

広島大学学位請求論文

**Interaction mechanism between
proteins and lipid membranes
characterized by vacuum-ultraviolet
circular dichroism spectroscopy**

(真空紫外円二色性によるタンパク質と
生体膜の相互作用機構の解析)

2022年

広島大学大学院理学研究科

物理学専攻

熊代 宗弘

目 次

1. 主論文

Interaction mechanism between proteins and lipid membranes characterized by vacuum-ultraviolet circular dichroism spectroscopy
(真空紫外円二色性によるタンパク質と生体膜の相互作用機構の解析)

2. 公表論文

- (1) Conformation of myelin basic protein bound to phosphatidylinositol membrane characterized by vacuum-ultraviolet circular-dichroism spectroscopy and molecular-dynamics simulations.

Munehiro Kumashiro, Yudai Izumi, Koichi Matsuo

Proteins: Structure, Function, and Bioinformatics, 89(10) (2021) 1251-1261.

- (2) Formation of β -strand oligomers of antimicrobial peptide magainin 2 contributes to disruption of phospholipid membrane. Munehiro Kumashiro, Ryoga Tsuji, Shoma Suenaga, Koichi Matsuo

Membranes, 12(3) (2022) 131.

3. 参考論文

- (1) Characterization of the mechanism of interaction between α_1 -acid glycoprotein and lipid membranes by vacuum-ultraviolet circular-dichroism spectroscopy.

Koichi Matsuo, Munehiro Kumashiro, Kunihiro Gekko

Chirality, 32(5) (2020) 594-604.

主論文

Contents

Summary.....	1
Chapter 1: General Introduction.....	5
Chapter 2: Methods	9
2.1 Liposome preparation.....	9
2.2 Ultraviolet spectroscopy.....	10
2.3 Circular dichroism spectroscopy.....	12
2.3.1 Principle of circular dichroism.....	12
2.3.2 Synchrotron radiation and HiSOR	15
2.3.3 Bending magnet beamline BL-12 at HiSOR.....	16
2.3.4 VUVCD spectrophotometer at HiSOR BL-12	17
2.3.5 Optical cell for VUVCD spectrophotometer.....	18
2.4 Linear dichroism spectroscopy.....	19
2.4.1 Principle of linear dichroism	19
2.4.2 Flow cell for linear dichroism measurement.....	21
2.5 Fluorescence anisotropy	21
2.5.1 Principle of fluorescence anisotropy	22
2.5.2 Fluorescence anisotropy of DPH in liposomes	23
2.6 Calcein dye leakage assay	24
2.7 VUVCD-NN prediction.....	25
Chapter 3: Circular dichroism study of the interaction between α 1-acid glycoprotein and lipid membranes	27
3.1 Introduction	27
3.2 Experimental.....	29
3.3 Results	31
3.3.1 Vacuum-ultraviolet circular dichroism spectra of membrane-bound states	31
3.3.2 Secondary structures of membrane-bound states	35
3.3.3 Positions of secondary structures in membrane-bound states.....	37
3.3 Discussion.....	38
Chapter 4: Circular dichroism and molecular dynamics studies of the interaction between myelin basic protein and phosphatidylinositol membrane.....	45

4.1 Introduction	45
4.2 Experiment and Theory	47
4.3 Results and Discussion	49
4.3.1 Vacuum-ultraviolet circular dichroism spectra of MBP in the presence of PI liposomes	50
4.3.2 Secondary structures of the membrane-bound conformation of MBP	52
4.3.3 Characterization of membrane-interaction helices of MBP using MD simulations	56
4.3.4 Membrane-bound conformation of MBP	61
Chapter 5: Circular dichroism, linear dichroism, and fluorescence studies of the interaction between antimicrobial peptide magainin 2 and lipid membrane	65
5.1 Introduction	65
5.2 Experimental.....	67
5.3 Results	72
5.3.1. Vacuum-ultraviolet circular dichroism	72
5.3.2. Linear dichroism.....	81
5.3.3. Fluorescence anisotropy	84
5.4 Discussion.....	87
Chapter 6: Conclusions.....	91
Acknowledgements	93
Reference	94

List of acronyms

A	acidic
AGP	α_1 -acid glycoprotein
AMP	antimicrobial peptide
AMR	antimicrobial resistance
A β	amyloid β
cryo-EM	cryogenic electron microscopy
DMPC	dimyristoyl phosphatidylcholine
DMPE	dimyristoyl phosphatidylethanolamine
DMPS	dimyristoyl phosphatidylserine
DOPC	dioleoyl phosphatidylcholine
DOPE	dioleoyl phosphatidylethanolamine
DPH	1,6-diphenyl-1,3,5-hexatriene
DPPC	dipalmitoyl phosphatidylcholine
DPPE	dipalmitoyl phosphatidylethanolamine
DPPG	dipalmitoyl phosphatidylglycerol
FTIR	Fourier-transform infrared
GROMACS	Groningen Machine for Chemical Simulations
L/P(P/L)	lipid-to-peptide (peptide-to-lipid)
LD	linear dichroism
M2	magainin 2
MB	membrane-bound
MBP	myelin basic protein
MD	molecular dynamics
N	native
NMR	nuclear magnetic resonance
NN	neural network
OCD	oriented circular dichroism
PG	phosphatidylglycerol
PI	phosphatidylinositol
PIP	phosphatidylinositol-4-phosphate

PIP2	phosphatidylinositol-4,5-bisphosphate
POPC	1-palmitoyl-2-oleoylphosphatidylcholine
POPG	1-palmitoyl-2-oleoylphosphatidylglycerol
PS	phosphatidylserine
SM	sphingomyelin
VUVCD	vacuum-ultraviolet circular dichroism
VUVCD-NN	combination method of vacuum-ultraviolet circular dichroism and neural network

Summary

Interaction of proteins with lipid membranes plays a key role in the manifestations of various biological phenomena such as myelin formation around neuron cell, antimicrobial activity in immune system, and amyloid fibril formation in amyloidosis. For elucidating the molecular mechanisms underlying the phenomena, it is necessary to characterize the membrane-bound conformation of proteins in the presence of bilayer liposomes, which have the properties of real cell membranes. However, the membrane-bound proteins including peripheral membrane proteins are difficult target for the advanced techniques such as X-ray crystallography and nuclear magnetic resonance spectroscopy. In this study, we have applied a vacuum-ultraviolet circular dichroism (VUVCD) spectroscopy to characterize the conformations of three types of membrane-bound proteins in aqueous solution and discussed their structure and function relationships at molecular level.

First, we investigated the mechanism of interaction between α_1 -acid glycoprotein (AGP) and lipid membranes by using VUVCD spectroscopy. AGP interacts with lipid membranes as a peripheral membrane protein to decrease the drug-binding capacity accompanying the $\beta \rightarrow \alpha$ conformational change that is considered a protein-mediated uptake mechanism for releasing drugs into membranes or cells. Here, we measured the VUVCD spectra of AGP in the presence of five types of liposomes whose constituent phospholipid molecules have different molecular characteristics in the head groups (e.g., different net charges). The VUVCD analysis showed that the α -helix and β -strand contents and the numbers of segments of AGP varied with the constituent phospholipid molecules of liposomes, while combining VUVCD data with a neural-network method predicted that these membrane-bound conformations comprised several common long helix and small strand segments. The amino-acid composition of each helical segment of the conformations indicated that amphiphilic and positively charged helices formed at the N- and C-terminal regions of AGP, respectively, were candidate sites for the membrane interaction. The addition of 1 M sodium chloride shortened the C-terminal helix while having no effect on the length of the N-terminal one. These results suggest that the N- and C-terminal

helices can interact with the membrane via hydrophobic and electrostatic interactions, respectively, and the formation of N-terminal helix would be crucial for releasing neutral drugs because this region contains the most-important site for binding with drugs such as progesterone.

Second, we investigated the conformation of full-length myelin basic protein (MBP) in membrane by using VUVCD spectroscopy and molecular dynamics (MD) simulation. The 18.5-kDa isoform of MBP interacts with the membrane surface of the myelin sheath to construct its compact multilamellar structure. Here, we measured the VUVCD spectra of MBP in the bilayer liposome comprising the following essential lipid constituents of the myelin sheath: phosphatidylinositol (PI), phosphatidylinositol-4-phosphate (PIP), and phosphatidylinositol-4,5-bisphosphate (PIP2). The spectra of MBP exhibited the characteristic peaks of the helix structure in the presence of PI liposome, and the intensity increased markedly in the presence of PIP and PIP2 liposomes to show an iso-dichroic point. This suggests that the amount of the membrane-bound conformation of MBP enhanced due to the increased number of negative net charges on the liposome surfaces. Secondary-structure analysis revealed that MBP in the membrane comprised approximately 40% helix contents and eight helix segments. MD simulations of the eight segments were conducted for 250 ns in the presence of PI membrane, which predicted two amphiphilic and three nonamphiphilic helices as the membrane-interaction sites. Further analysis of the distances of the amino-acid residues in each segment from the phosphate group showed that the nonamphiphilic helices interact with the membrane surface electrostatically, while the amphiphilic ones invade the inside of the membrane to produce electrostatic and hydrophobic interactions. These results suggest that MBP can interact with the PI membrane via amphiphilic and nonamphiphilic helices under the control of a delicate balance between electrostatic and hydrophobic interactions. The mechanism of MBP-membrane interaction would provide an important basis for understanding the formation and stabilization processes of myelin sheath.

Finally, we investigated the molecular mechanism of antimicrobial activity of magainin 2 (M2) by using VUVCD, linear dichroism (LD), and fluorescence spectroscopies. The antimicrobial peptides M2 interact with and oligomerize on the membrane, inducing structural damage in bacterial cell membranes. Although extensive biophysical studies have revealed the interaction mechanism between M2 and membranes, the mechanism of membrane-mediated oligomerization of

M2 is controversial. Here, we measured the VUVCD and LD spectra of M2 in dipalmitoyl-phosphatidylglycerol lipid membranes in lipid-to-peptide (L/P) molar ratios from 0–26 to characterize the conformation and orientation of M2 on the membrane. The results showed that M2 changed from random coil to α -helix structures via an intermediate state with increasing L/P ratio. Singular value decomposition analysis supported the presence of the intermediate state, and global fitting analysis revealed that M2 monomers with an α -helix structure assembled and transformed into M2 oligomers with a β -strand-rich structure in the intermediate state. In addition, LD spectra showed the presence of β -strand structures in the intermediate state, disclosing their orientations on the membrane surface. Furthermore, fluorescence spectroscopy showed that the formation of β -strand oligomers destabilized the membrane structure and induced the leakage of calcein molecules entrapped in the membrane. These results suggest that the formation of β -strand oligomers of M2 plays a crucial role in the disruption of the cell membrane.

All the findings in this study demonstrate that VUVCD spectroscopy and its combination of experimental (e.g., LD and fluorescence) and theoretical (e.g., NN and MD) methods provide useful information on the interaction mechanism between proteins and lipid membranes.

Chapter 1: General Introduction

Interaction between peripheral membrane protein and lipid membrane plays a crucial role in the biological functions such as drug delivery into the membrane (or cell), formation of myelin membrane around neuron cell, and membrane disruption related to immune system¹⁻³. The interaction also induces the formation of toxic oligomers of amyloidogenic proteins, leading to serious neurological diseases such as Alzheimer's disease and Parkinson's disease⁴. It is known that the water-soluble protein approaches to and interacts with the surface of membrane to induce large structural changes accompanying the expression of its functions or diseases¹⁻⁴. To gain detailed insight into the molecular mechanisms underlying the life phenomena, it is therefore of great importance to understand the complex nature of the interactions between proteins and lipid membranes, including the structural change of the proteins.

X-ray crystallography, nuclear magnetic resonance (NMR) spectroscopy, and cryogenic electron microscopy (cryo-EM) are most important methods for characterizing the secondary and tertiary structures of proteins. Although X-ray crystallography requires the crystallization of proteins, with the developments for membrane protein crystallization techniques⁵, this method has become possible for many integral membrane proteins. As for NMR spectroscopy, the targets are restricted to the proteins with low molecular weight (upper limit: 30 kDa), but the development of new types of membrane mimetic model (e.g., nanodisc) has made it possible to analyze the structure of several membrane-bound peptides under membrane mimetic condition⁶. Cryo-EM is a recent emerging technique that can be used to analyze the structure of isolated biomolecular complexes with molecular weight ranging from tens of kilo-Daltons (e.g., hemoglobin) to several mega-Daltons (e.g., virus particles)⁷. With recent advances in detector and image processing technologies⁷, cryo-EM has been applied to structural analysis of various membrane proteins, including those even in the presence of liposomes⁸ that have the characteristics of real cell membrane. Despite the considerable progress achieved in the structural analysis of proteins in membrane mimetic environment, the proteins bound to the periphery of liposomes are not amenable

to these techniques of modern molecular biology⁹ because of the difficulty of crystallization and the limitation to complex with large molecular weight^{10,11}.

Circular dichroism (CD) spectroscopy is one of the most widely used techniques for monitoring the conformation of protein in solution. Although CD does not reveal protein structure at the atomic resolution that is possible in X-ray crystallography and NMR spectroscopy, it can be applied to the conformational analysis of both integral and nonintegral (or peripheral) membrane proteins in the presence of liposome¹²⁻¹⁴. Further, vacuum-ultraviolet CD (VUVCD) spectroscopy using synchrotron radiation as a light source has extended the protein CD spectrum into the vacuum-ultraviolet region (down to 160 nm)^{15,16}, which allowed us to improve the accuracy of estimating the contents and numbers of α -helix and β -strand segments of proteins compared to conventional CD spectroscopy¹⁷ and also to determine the positions of these segments on the amino-acid sequence in combination with a neural network (NN) algorithm (VUVCD-NN method)¹⁷. Furthermore, by combining VUVCD with linear dichroism (LD), the information on the orientations of secondary structures of membrane-bound proteins can be provided¹⁴. Recently, the contents, segments, positions, and orientations of secondary structures of various membrane-bound proteins (e.g., α -acid glycoprotein, β -amyloid protein, and β -lactoglobulin) have been successfully estimated^{14,18,19}, indicating that this technique could be a powerful tool for characterizing the conformation of peripheral membrane proteins in liposomes.

It has been reported that the lipid composition of membranes changes in several diseases such as Parkinson's disease and multiple sclerosis²⁰⁻²². In Parkinson's disease and in allergic encephalomyelitis or multiple sclerosis, the ratio of charged to uncharged lipids has been found to be different from that in normal brains²⁰⁻²². It has been suggested that the α -helical conformation of amyloid- β -(1-40), which is a causative peptide in Alzheimer's disease, on charged liposome is significantly different from that on uncharged liposome²³. In addition, the structural rearrangement in the peptide has been found to occur depending on the lipid-to-peptide (L/P) molar ratio when interacting with the charged lipid membrane²³. Further, the fibrillation speed and toxicity of α -synuclein, which is thought to be the cause of Parkinson's disease, has also been shown to depend on the L/P molar ratio (at low L/P: promotion of amyloidogenesis, at high L/P: inhibition of amyloidogenesis)²⁴. Based on the results of these studies, we could hypothesize that the lipid composition and the L/P molar ratio affect the membrane-bound

conformation of proteins, resulting in the diseases. It is difficult to investigate the conformational dependence on the lipid composition and the L/P molar ratio by X-ray crystallography and NMR spectroscopy, but VUVCD spectroscopy can be used to study it easily.

In this study, we have characterized the unique and complicated membrane-induced conformational change of α_1 -acid glycoprotein (AGP) (Chapter 3), myelin basic protein (MBP) (Chapter 4), and antimicrobial peptide (AMP) magainin 2 (M2) (Chapter 5) and discussed the contributions to their biological functions. AGP interacts with lipid membranes as a peripheral membrane protein to decrease the drug-binding capacity accompanying the conformational change (Figure 1.1 (a))^{25,26}. This conformational change is closely related to a protein-mediated uptake mechanism for releasing drugs into membranes or cell, but the interaction mechanism between AGP and lipid membranes is poorly understood. MBP is the second most abundant protein in the myelin sheath of central nervous system and interacts with the membrane surfaces of the myelin sheath to form its compact multilayered structure (Figure 1.1 (b))^{27,28}. The conformation of membrane-bound MBP remains to be further explored because of the difficulty of crystallization¹¹ and the complicated dependence on lipid composition^{2,29,30}. M2, one of the most widely studied AMPs, interacts with bacterial cell membranes and induces the structural damage in the membranes (Figure 1.1 (c))^{3,31}. Although extensive research has revealed the interaction mechanism between M2 and liposome membranes, the mechanism of L/P-dependent and membrane-mediated oligomerization of M2 is controversial. To reveal the interaction mechanism between the membrane-bound proteins (or peptides) and lipid membranes at the molecular level, we used VUVCD spectroscopy and its combinations of NN, LD, fluorescence spectroscopy, and molecular dynamics (MD) simulation. Our findings demonstrate that VUVCD spectroscopy is a powerful tool for characterizing the interaction mechanism between peripheral membrane protein and lipid membrane.

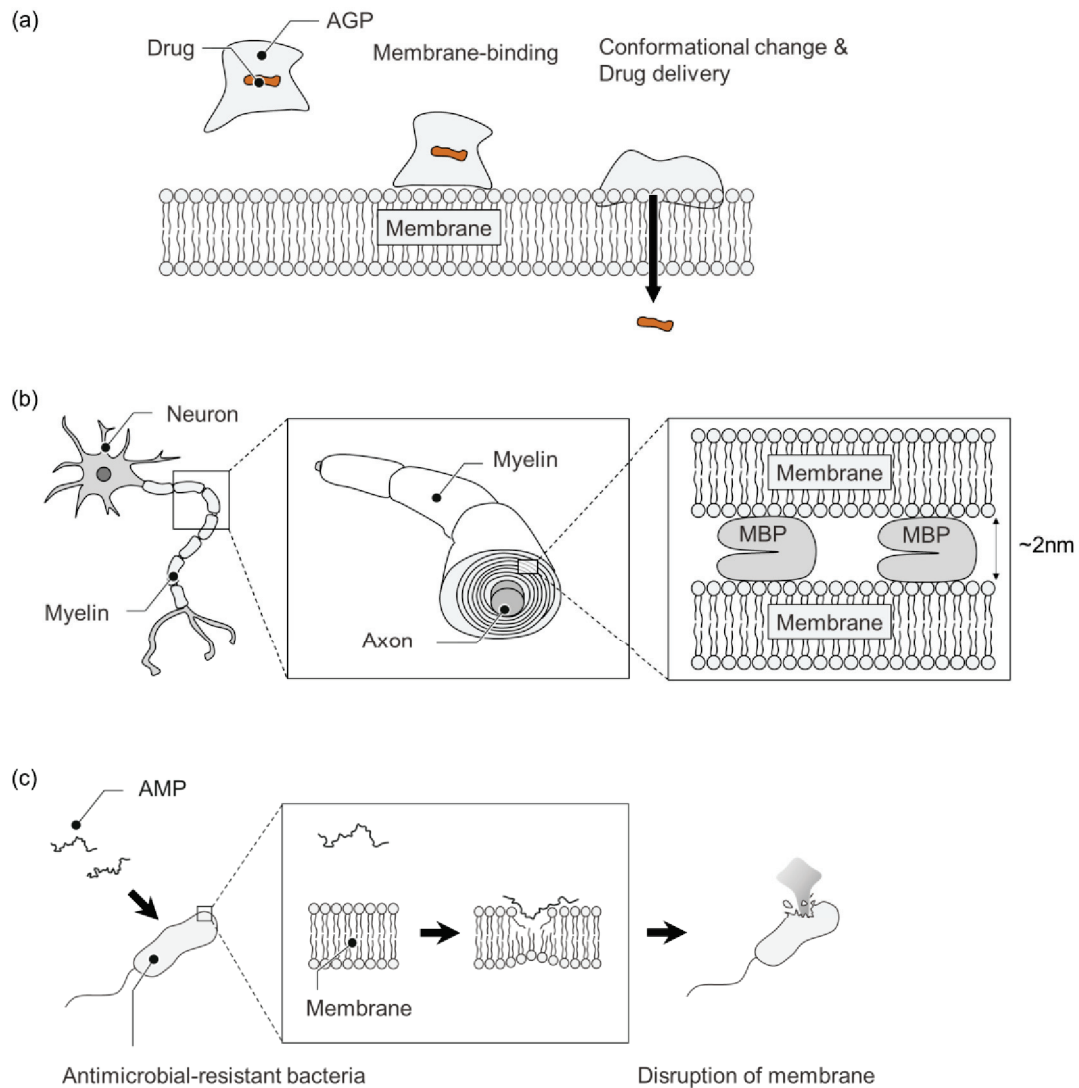


Figure 1.1. (a) Schematic diagram of interaction between AGP and lipid membrane. The membrane-induced conformational change of AGP is related with the drug delivery function of AGP. (b) Diagram of the relationship between neuron cell, myelin sheath, axon, lipid membrane, and MBP. MBP functions as a “molecular glue” in the stacking structure of myelin sheath. (c) Diagram of membrane disruption by AMP. AMP interacts with cell membrane of bacteria and induces structural damage in the membranes.

Chapter 2: Methods

2.1 Liposome preparation

Liposomes are spherical artificial lipid vesicles that mimic the cell membranes of a living organism. Large unilamellar vesicle, the most widely used liposome model in biochemical experiments, can be prepared by using an extrusion technique (Mini-Extruder, Avanti)³², whose experimental set-up is shown in Figure 2.1. The phospholipid powder is dissolved in a buffer to obtain a multilamellar liposome. The liposome solution is then placed alternately in liquid nitrogen and a heated block (five freeze-thaw cycles) as the liposomes exhibit low lamellarity. Large unilamellar vesicles are prepared using an extrusion technique, in which the liposome solution is passed 25 times through a polycarbonate membrane (Whatman, Clifton, NJ) with a pore diameter of 100 nm.

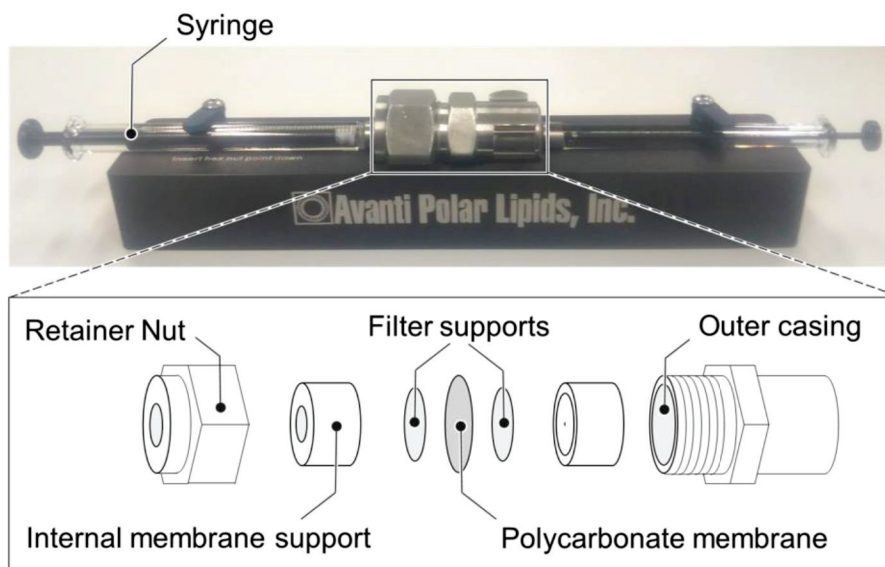


Figure 2.1. Experimental set-up of extrusion method for liposome preparation.

2.2 Ultraviolet spectroscopy

Ultraviolet spectroscopy is an absorption spectroscopy method in the ultraviolet region commonly used in analytical chemistry. This section describes the basic principles of ultraviolet absorption of molecules, which are also the fundamentals of the sections 2.3 and 2.4 (CD and LD spectroscopies).

A molecule in solution can absorb the ultraviolet light and transit from a ground state $|0\rangle$ to an excited state $|n\rangle$. Based on Fermi's Golden Rule, the transition probability $\Gamma_{on}(\omega)$ is described as^{33,34},

$$\Gamma_{on}(\omega) = \frac{2\pi e^2}{\hbar m_e^2 c^2} \sum_i |\langle 0 | \mathbf{A} \cdot \hat{\mathbf{p}}_i | n \rangle|^2 \delta(\hbar\omega - \hbar\omega_{0n}), \quad (2.1)$$

where e is the elementary charge, m_e is the electron mass, \mathbf{A} is the vector potential of incident light, $\hat{\mathbf{p}}_i (= i\hbar\nabla)$ is the momentum operator of i th electron, δ is the Dirac delta function, $\hbar\omega$ is the photon energy, and $\hbar\omega_{0n}$ is the energy difference between ground and excited states. The $\Gamma_{on}(\omega)$ can be transformed into the dimensionless oscillator strength f written as,

$$f = \frac{2}{m_e \hbar \omega_{0n}} \sum_i |\langle 0 | \exp(i\mathbf{k} \cdot \mathbf{r}_i) (\boldsymbol{\mathcal{E}} \cdot \hat{\mathbf{p}}_i) | n \rangle|^2, \quad (2.2)$$

where \mathbf{k} is the wavenumber vector of incident light, \mathbf{r}_i is the coordinate of i th electron, and $\boldsymbol{\mathcal{E}}$ is the polarization vector of incident light. In case of linearly polarized light, a Taylor series expansion of Equation (2.2) ($\exp(i\mathbf{k} \cdot \mathbf{r}_i) = 1 + i(\mathbf{k} \cdot \mathbf{r}_i) - \dots$) leads to the following equation:

$$f = \frac{2m_e \omega_{0n}}{e^2 \hbar} |\boldsymbol{\mathcal{E}} \cdot \langle 0 | \hat{\boldsymbol{\mu}} | n \rangle|^2 + \frac{2m_e c^2}{e^2 \hbar \omega_{0n}} |(\mathbf{k} \times \boldsymbol{\mathcal{E}}) \cdot \langle 0 | \hat{\boldsymbol{m}} | n \rangle|^2 + \dots, \quad (2.3)$$

where $\hat{\boldsymbol{\mu}}$ and $\hat{\boldsymbol{m}}$ are the electric-dipole and magnetic-dipole operators. The first term of Equation (2.3), the so-called electric dipole allowed transition, does not vanish in electronic transitions such as $\pi \rightarrow \pi^*$ transition³⁵⁻³⁷, in which the parity of $|0\rangle$ is different with that of $|n\rangle$. The second term of Equation (2.3), the so-called magnetic dipole allowed transition, does not disappear in electronic transitions such as $n \rightarrow \pi^*$ transition³⁵⁻³⁷, in which the parity of $|0\rangle$ is the same as that of $|n\rangle$. These terms determine the curve shape of ultraviolet spectrum of a molecule in solution.

Figure 2.2 shows the ultraviolet spectra of protein, myoglobin, in the wavelength region from 320 nm and 190 nm. Myoglobin shows a peak absorption at 280 nm, which is mainly attributed to the electric dipole allowed transitions of aromatic residues such as L_b and L_a transitions of tryptophan residue in Platt notation³⁵. Myoglobin also exhibits a large absorption band around 190 nm with a shoulder around 220 nm. The absorptions at 190 nm and 220 nm are due to the electric dipole allowed $\pi \rightarrow \pi^*$ transition and the magnetic dipole allowed $n \rightarrow \pi^*$ transition, respectively, of peptide bond³⁵⁻³⁷.

Based on Lambert-Beer's law, the absorbance A is proportional to the concentration c of a solute and an optical path length l as follows:

$$A = -\log \frac{I}{I_0} = \varepsilon cl, \quad (2.4)$$

where I and I_0 are the intensities of the incident and transmitted light, respectively, and ε is the molar extinction coefficient³⁵. Thus, ultraviolet spectroscopy can be used to determine the concentration of the solute in the sample if the optical path length and the molar extinction coefficient are known. We measured the ultraviolet spectrum of protein or peptide using a UV-vis spectrophotometer (V-560, Jasco, Japan) to determine the concentration of protein or peptide in the sample.

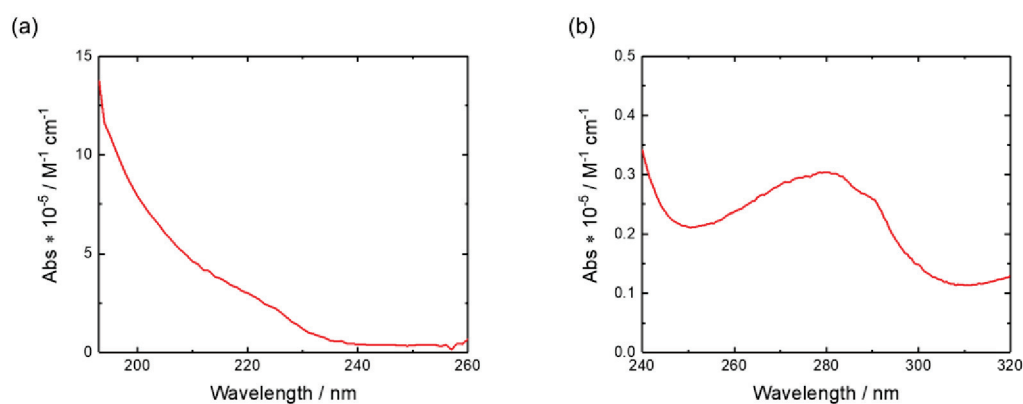


Figure 2.2. Absorption spectra of myoglobin in wavelength region from 190 nm to 260 nm (a) and from 240 nm to 320 nm (b).

2.3 Circular dichroism spectroscopy

CD spectroscopy is a powerful tool for analyzing the conformation of chiral molecules such as proteins in solution. This section describes the principle of CD and the measurement system of VUVCD spectrophotometer installed at Hiroshima Synchrotron Radiation Center (HiSOR) BL-12.

2.3.1 Principle of circular dichroism

CD is the difference in absorption between left- and right-handed circularly polarized light and is defined as³⁵⁻³⁷,

$$\Delta\varepsilon = \varepsilon_L - \varepsilon_R, \quad (2.5)$$

where ε_L and ε_R are the molar extinction coefficients for the left- and right-handed circularly polarized light, respectively. The CD intensity of chiral molecules in solution is proportional to the scalar product between the electric dipole and magnetic dipole transition moments, which is described as³⁴⁻³⁸,

$$\Delta\varepsilon \propto \text{Im}\langle n|\hat{\boldsymbol{\mu}}|0\rangle \cdot \langle 0|\hat{\boldsymbol{m}}|n\rangle. \quad (2.6)$$

This formula can be derived from the difference in the oscillator strengths, Equation (2.2), corresponding to the left- and right-handed circularly polarized light. The low-dimensional term of coupling between the electric dipole and electric dipole transition moments, as well as the term of coupling between electric dipole and electric quadrupole transition moments, cancels out due to the un-oriented solution condition and the conservation laws of electromagnetism in parity and reversality³⁴.

From the viewpoint of Equation (2.6), chiral molecules such as helical hexahelicene have non-zero electric dipole and magnetic dipole transition moments in one electronic transition, leading to non-zero CD intensity. On the other hand, in an achiral chromophore such as peptide bond, either the electric dipole (e.g., $n \rightarrow \pi^*$ transition) or the magnetic dipole (e.g., $\pi \rightarrow \pi^*$ transition) transition moment is equal to zero, or the two kinds of transition moments are perpendicular to each other (e.g., $n \rightarrow \sigma^*$ transition), resulting in zero CD intensity.

However, when identical chromophores are adjacent to each other in a chiral environment (e.g., asymmetric carbon atom), the chiral interactions between the electronic transitions perturb the global transition, resulting in non-zero CD intensity³⁹. Since the perturbation Hamiltonian depends on the distance and relative angle between the chromophores, the shape of CD spectra also depends on the distance and relative angle, leading to the fact that the CD spectrum of a protein reflects the conformation of the protein. Based on the mechanism of CD generation, Woody et al. have developed the semi-empirical “matrix method”³⁹, which allows us to calculate the CD spectrum of a protein from the three dimensional coordinates of the protein structure.

Figure 2.3 (a) shows the CD spectra of 31 proteins in the wavelength region from 260 nm to 160 nm^{15,16}. Since proteins have electronic transitions of peptide bond such as $\pi \rightarrow \pi^*$ and $n \rightarrow \pi^*$ transitions in the wavelength region³⁹, the CD spectra contain the information about the conformation of protein backbone, including α -helix, β -strand, and random coil. As shown in Figure 2.4, the dihedral angles of protein backbone (ϕ and ψ), which describes the conformation of protein backbone, have restricted values due to the steric hindrance among the peptide bond atoms, the hydrogen atoms on the α carbon, and the side chain atoms. In the plots of ϕ against ψ (Ramachandran plots)^{40,41}, the major allowed regions are corresponding to the secondary structures such as α -helix and β -strand. Thus, CD spectrum $d(\lambda)$ of a protein can be approximated as the sum of fraction c_i of the component CD spectrum $s_i(\lambda)$ of the i th secondary structure of the protein, as written in the following equation:

$$d(\lambda) = \sum_{i=1}^l c_i s_i(\lambda), \quad (2.7)$$

where l is the number of types of secondary structures³⁶.

Figure 2.3 (b) shows the component spectra of secondary structures of proteins. These spectra can be calculated by using the CD spectra of proteins of known structures in Figure 2.3 (a) and the classical least squares method⁴²,

$$S = (C^T C)^{-1} C D, \quad (2.8)$$

where S , C , and D are the matrices of component spectra, secondary-structure fractions of reference proteins, and CD spectra of reference proteins, respectively. The CD spectrum of α -helix shows two negative peaks at 222 nm ($n \rightarrow \pi^*$

transition) and 208 nm, and a positive peak at 190 nm (exciton splitting $\pi \rightarrow \pi^*$ transition) with a small shoulder around 175 nm (charge-transfer transition)⁴³. The spectrum of β -strand shows a negative peak at 220 nm ($n \rightarrow \pi^*$ transition) and around 175 nm, and a positive peak at 200 nm (exciton splitting $\pi \rightarrow \pi^*$ transition)⁴³. The spectrum of random coil shows a positive peak at 225 nm and a negative peak at 200 nm. Woody et al. suggested that the dominant conformation of random coil is polyproline II helix⁴⁴, whose CD spectral peaks around 225 nm and 195 nm are attributed to charge-transfer transitions⁴⁵. Due to the distinctive shapes of the CD spectra of secondary structures, the content of secondary structures of an unknown protein can therefore be estimated by measuring CD spectrum of the protein and analyzing the spectrum based on the Equation (2.7).

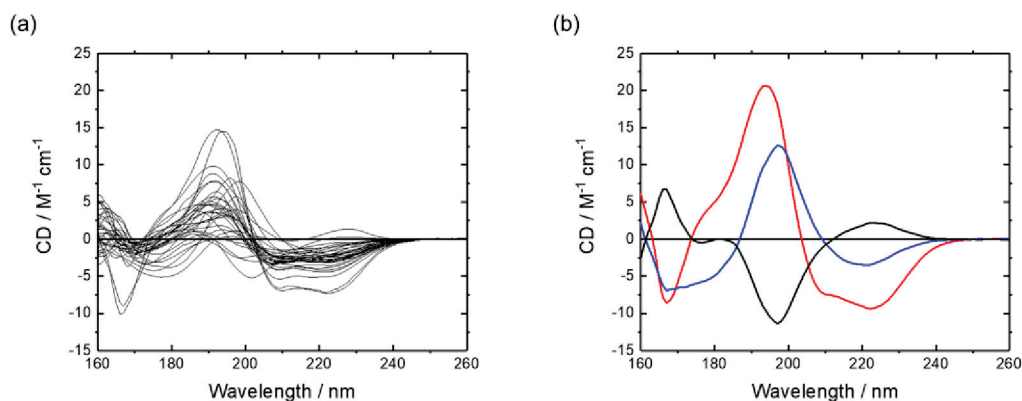


Figure 2.3. (a) CD spectra of 31 proteins and (b) component spectra of proteins (red: α -helix; blue: β -strand; black: random coil (others)).

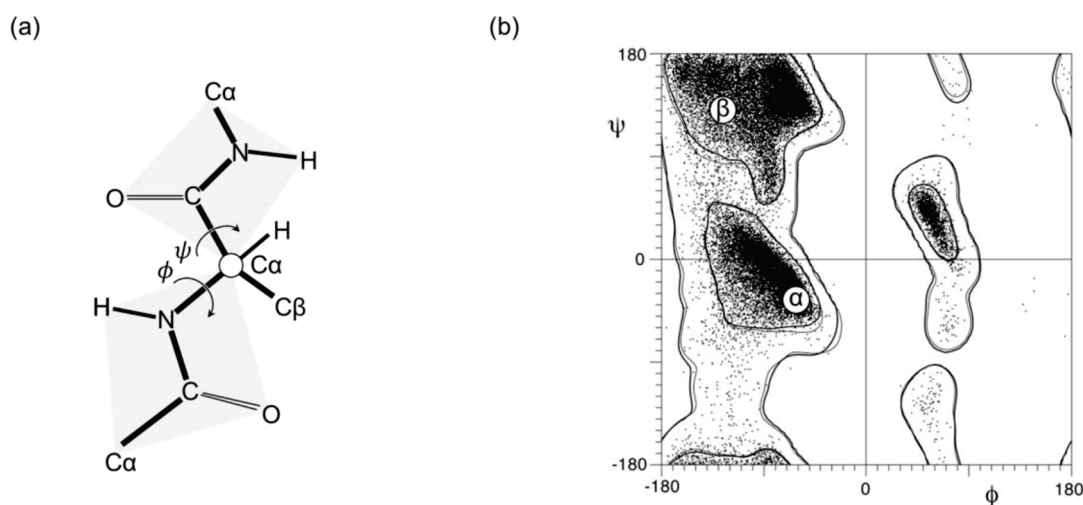


Figure 2.4. (a) Diagram of dihedral angle of protein and (b) Ramachandran plots⁴¹. The regions corresponding to α -helix and β -strand are also shown.

2.3.2 Synchrotron radiation and HiSOR

Synchrotron radiation is an electromagnetic radiation emitted when the motion of charged particles, including electron, are accelerated by electrostatic potential, or are changed by magnetic field. Compared with commercially available light sources such as Xe lamp, synchrotron radiation has several advantages as follows:

1. Wide spectral range from microwave to hard X-ray,
2. Linearly or circularly polarized light,
3. High flux,
4. High brilliance,
5. Pulsed time structure.

The above features of synchrotron radiation allow us to investigate many aspects of the structure of matter at the atomic and molecular levels. Thus, synchrotron radiation has been used as a powerful probe in various fields such as life science, material science, chemistry, earth science, environmental science, medical science, and industry.

HiSOR is a compact 700 MeV synchrotron radiation facility established at Hiroshima University. Figure 2.5 shows the layout of experimental hall in HiSOR. The electron-storage ring of HiSOR is composed of two 180-degree normal-conducting bending magnets and two insertion devices, a linear undulator and an APPLE-II undulator. The compact racetrack-type ring produces high-intensity synchrotron radiation in wide spectral range from ultraviolet to soft X-rays. Using the synchrotron radiation as a probe, users can perform polarization-dependent high-resolution angle-resolved photoemission spectroscopy (BL-1), surface X-ray absorption fine structure (BL-3), angle-resolved photoemission spectroscopy (BL-7), high-resolution spin-resolved angle-resolved photoemission spectroscopy (BL-9B), VUVCD (BL-12), and soft X-ray magnetic CD (BL-14) in each beamline⁴⁶.

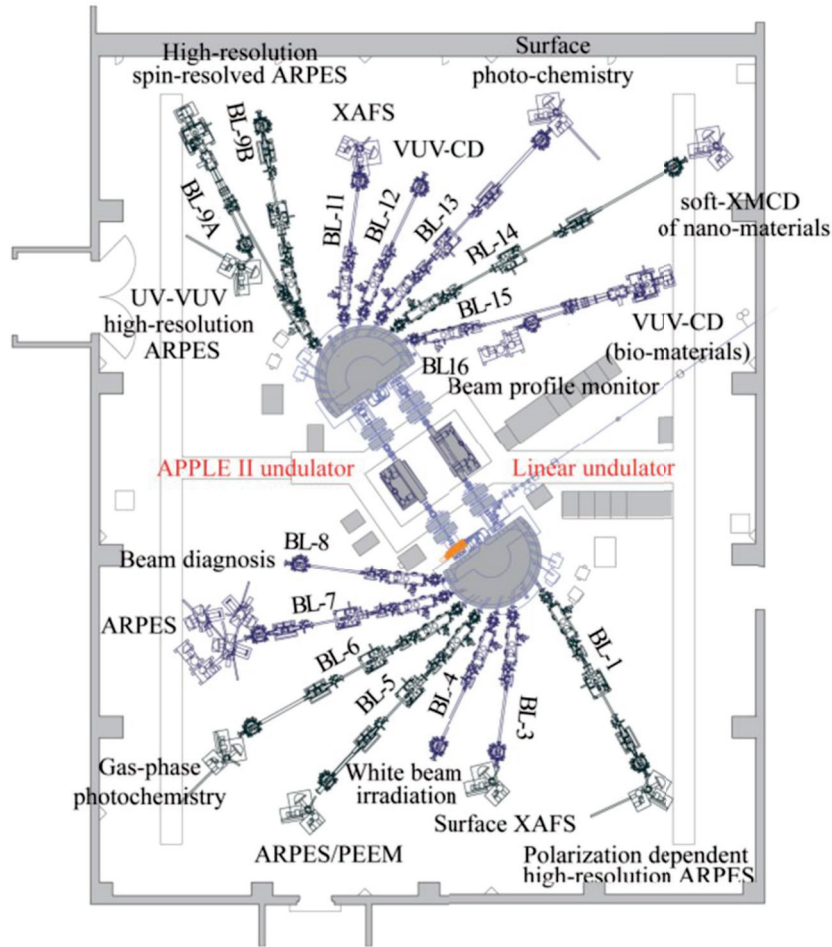


Figure 2.5. Layout of experimental hall in HiSOR⁴⁶.

2.3.3 Bending magnet beamline BL-12 at HiSOR

We used the VUVCD spectrophotometer at HiSOR BL-12. Figure 2.6 shows the schematic layout of the optical system of HiSOR BL-12. The synchrotron radiation beamline is composed of only three reflective elements, two of which are focusing mirrors (M0 and MF), and another of which is the Wadsworth-type monochromator with a normal incidence grating (GR). The minimization of numbers of mirrors and wide acceptance angles of the optical elements contribute to high flux of monochromatic light (3×10^{11} photons/sec/100 mA at 200 nm). The optical design covers the light energy range between 2 eV (620 nm) and 10 eV (124 nm)⁴⁷.

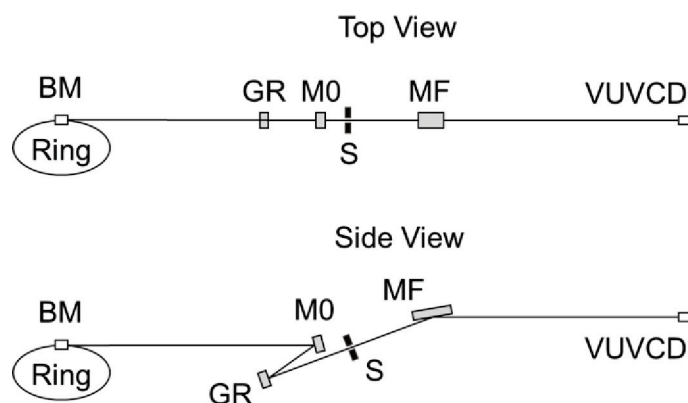


Figure 2.6. Schematic layout of the optical system at BL-12 (BM: bending magnet; GR: grating; M0: focusing mirror 0; S: slit; MF: focusing mirror).

2.3.4 VUVCD spectrophotometer at HiSOR BL-12

Figure 2.7 shows the block diagram of VUVCD spectrophotometer installed at the end-station of HiSOR BL-12. The system is composed of a polarization modulation chamber and a sample chamber. During measurement, the chambers are evacuated ($\sim 10^{-4}$ Pa) or purged with nitrogen gas to avoid light absorption in the vacuum-ultraviolet region by air and water vapor. The monochromatic light from the beamline is separated into two orthogonal linearly polarized beams (main light and reference light) by a polarizer (POL) with a separation angle of $5.1^\circ \sim 5.4^\circ$. Both beams are modulated into circularly polarized light at 50 kHz by a photoelastic modulator (PEM). The main light passes through a sample cell and is detected by a photomultiplier tube (Main-PM). The reference light is modulated into linearly polarized light at 100 kHz by an analyzer (ANA) and is detected by another photomultiplier tube (Ref-PM). The signals from Main-PM and Ref-PM are rectified and amplified by lock-in-amplifier (LIA), and the CD signal of the sample is monitored on a computer. This double-beam system, the so-called servo-control system, contributes to the compensation of the thermal drift of the PEM in the vacuum-ultraviolet region and the stabilization of the LIA. Thus, the servo-control system using synchrotron radiation as a light source allows us to perform

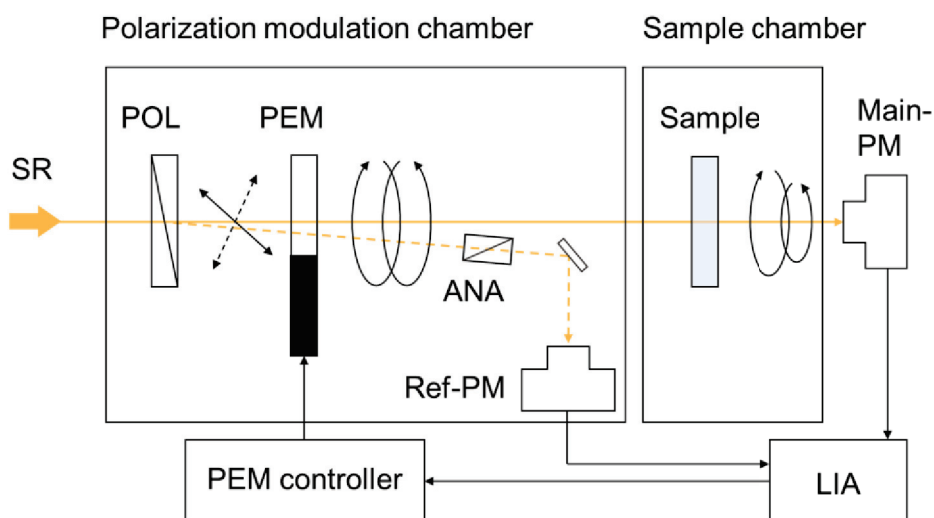


Figure 2.7. Block diagram of vacuum-ultraviolet circular dichroism spectrophotometer installed at HiSOR BL-12 (SR: synchrotron radiation; POL: polarizer; PEM: photo-elastic modulator; ANA: analyzer; LIA: lock-in-amplifier; PM: photomultiplier).

accurate VUVCD measurements of biomolecules with a high signal-to-noise ratio⁴⁸.

2.3.5 Optical cell for VUVCD spectrophotometer

Figure 2.8 shows a schematic of the assembled-type optical cell for VUVCD spectrophotometer. The optical cell is composed of a container with a cylindrical screw, two CaF₂ (or MgF₂) crystal windows, and three O-rings. CaF₂ is used as the window crystal, because CaF₂ crystal has high transmittance in the vacuum-ultraviolet region. The optical path length can be adjusted to be ultra-thin between 1.3 μm and 100 μm using a Teflon spacer, to avoid light absorption by the solvent. The screw and O-rings are used to set the sample solution in the optical cell holder⁴⁸.

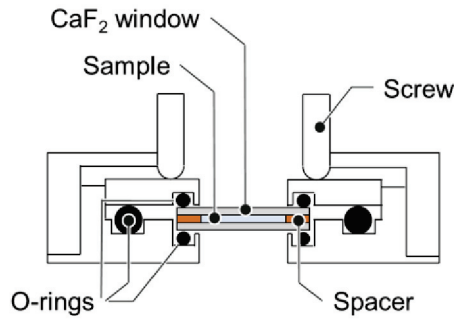


Figure 2.8. Schematic of assembled-type optical cell for VUVCD measurements.

2.4 Linear dichroism spectroscopy

Linear dichroism (LD) spectroscopy is a useful method for estimating the orientation of molecules in flow environment. This section describes the principle of LD and flow LD measurement system installed at the VUVCD spectrophotometer.

2.4.1 Principle of linear dichroism

LD is the difference in absorption between light linearly polarized parallel (A_{\parallel}) and perpendicular (A_{\perp}) to an orientation axis and is defined as³⁵,

$$LD = A_{\parallel} - A_{\perp}. \quad (2.9)$$

From a quantum mechanical point of view, the LD intensity of oriented molecules in flow environment is proportional to the difference in transition moments polarized parallel (μ_{\parallel}) and perpendicular (μ_{\perp}) to the orientation axis or flow direction, which is described as,

$$LD \propto |\langle 0 | \mu_{\parallel} | n \rangle|^2 - |\langle 0 | \mu_{\perp} | n \rangle|^2. \quad (2.10)$$

In the mathematical framework of LD, LD is a function of an angle α between the transition moment and the orientation axis, and is written as,

$$LD = \frac{3}{2} A_{\text{iso}} S (3 \cos^2 \alpha - 1), \quad (2.11)$$

where A_{iso} is the absorbance of an un-oriented sample and S is the orientation factor ($S = 1$ for perfect orientation; $S = 0$ for random orientation). If the polarization of the transition moment is perfectly parallel to the orientation axis ($\alpha = 0^\circ$), the oriented molecules show a positive LD³⁵. On the other hand, the molecules exhibit a negative LD if the polarization of the transition moment is perfectly perpendicular to the orientation axis ($\alpha = 90^\circ$)³⁵. Thus, LD gives the information on the orientation of the chromophores of the oriented sample.

Figure 2.9 shows the transition moments in α -helix and β -strand and the schematic of LD signals for α -helix and β -strand polarized parallel or perpendicular to the orientation direction. The directions of $n \rightarrow \pi^*$ and $\pi \rightarrow \pi^*$ transition moments relative to the α -helix and β -strand axes are characteristic as shown in Figure 2.9. Thus, the LD signals of α -helix and β -strand at 220, 208, and 195 nm depend on these orientations. For example, α -helix polarized parallel to the orientation direction shows two negative peaks at 195 and 220 nm and a positive peak at 208 nm, while α -helix polarized perpendicular to the orientation direction shows the sign-inverse LD spectrum (Figure 2.9 (a))^{35,49}. LD spectroscopy can therefore be used to estimate the orientation of secondary structure with respect to the orientation (flow) direction.

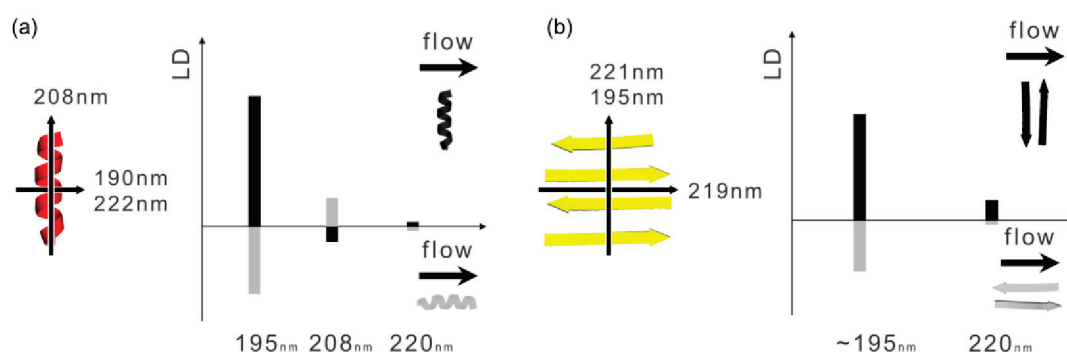


Figure 2.9. Transition moments in α -helix (a) and β -strand (b), and the schematic diagram of expected LD signals for α -helix (a) and β -strand (b) polarized parallel or perpendicular to the orientation (flow) direction.

2.4.2 Flow cell for linear dichroism measurement

For the flow LD measurements of peptides bound to liposomes, we used the liquid-circulation system attached to the VUVCD spectrophotometer at HiSOR BL-12¹⁴. Figure 2.10 shows the diagram of the flow LD measurement system. The system consists of a dual-plunger parallel-flow pump (LC-20AD, Shimadzu, Japan) and an LD flow cell (Translume, MI; light path length: 75 μm), which circulates liposome solution from the sample container to the LD flow cell. Shear flow deforms the liposomes from spherical to elliptical shapes, and the axes of the elliptical liposomes are oriented along the flow direction on average. The peptides on the elliptical liposomes show a slight bias in the directions of their axes and show the LD signals according to the orientation of the secondary structure relative to the membrane surface.

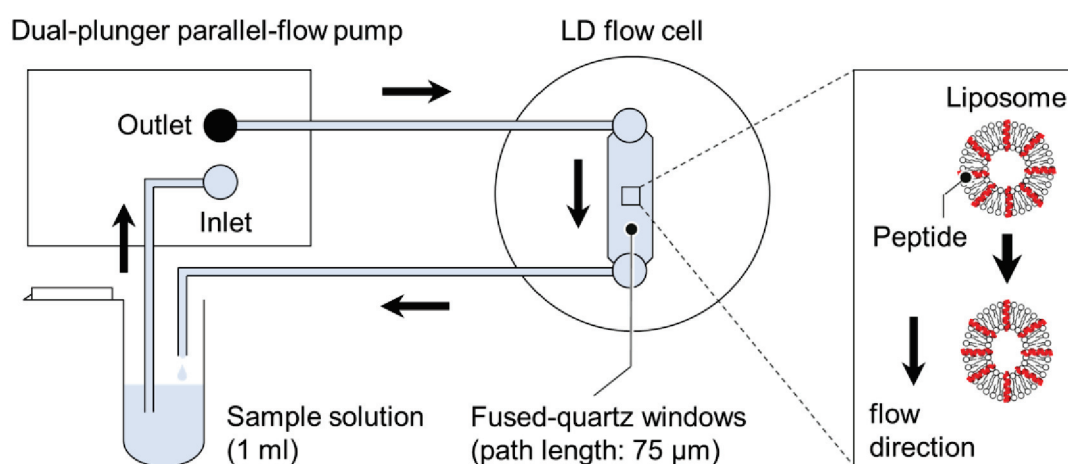


Figure 2.10. Block diagram of the liquid-circulation system with a dual-plunger parallel-flow pump and LD flow cell. The schematic diagram of liposome deformation due to shear flow is also shown.

2.5 Fluorescence anisotropy

Fluorescence anisotropy can be used to investigate membrane fluidity, and measurement of the temperature dependence of the fluorescence anisotropy of 1,6-

diphenyl-1,3,5-hexatriene (DPH) in membranes provides the information on the stability of the membranes. This section describes the principle of fluorescence anisotropy of DPH in liposomes.

2.5.1 Principle of fluorescence anisotropy

Figure 2.11 (a) illustrates the measurement of fluorescence anisotropy, which is defined as⁵⁰,

$$r = \frac{I_{vv} - GI_{vh}}{I_{vv} + 2GI_{vh}}, \quad (2.12)$$

where I_{vv} is the intensity of detected light when both excitation and emission polarizers are mounted vertically, I_{vh} is the intensity of detected light when the excitation and emission polarizers are installed vertically and horizontally, respectively. The factor G in Equation (2.12) is determined from I_{hv}/I_{hh} (I_{hv} : intensity of detected light when the emission and the excitation polarizers are installed horizontally and vertically, respectively, and I_{hh} : intensity of detected light when the emission and the excitation polarizers are mounted horizontally). The absolute value of fluorescence anisotropy is based on the relationship between the fluorescence lifetime and the rotational diffusion time of the fluorescent molecule. As shown in the Figure 2.11 (b), the linearly polarized excitation light induces fluorescence emission from a fluorophore, which is also polarized parallel to a

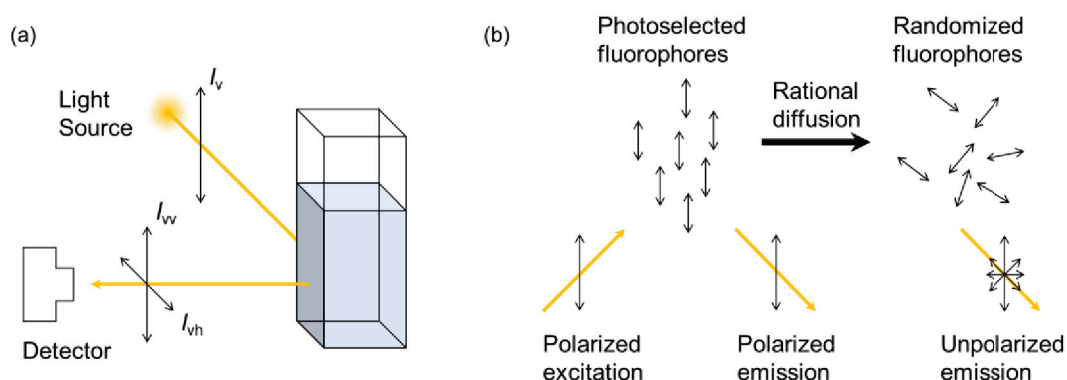


Figure 2.11. (a) Schematic diagram of fluorescence anisotropy and (b) diagram of the relationship between fluorescence anisotropy and rotational diffusion⁵⁰.

specific direction within fluorophore structure. Since the fluorophore molecules diffuse randomly in an isotropic solution, the polarized fluorescence light depolarizes during the fluorescence lifetime, resulting in the phenomenon of fluorescence anisotropy. The faster the rotational diffusion, the smaller the fluorescence anisotropy; conversely, the slower the rotational diffusion, the larger the fluorescence anisotropy. The degree of rotational diffusion of the fluorophore molecule depends on the following factors: (1) size and shape of the rotating molecule and (2) viscosity of the molecular environment. Thus, fluorescence anisotropy measurements can be used to investigate the micro-viscosity of lipid membranes or membrane fluidity⁵⁰.

2.5.2 Fluorescence anisotropy of DPH in liposomes

Figure 2.12 (a) shows the chemical structure of DPH. In the experiments of fluorescence anisotropy of DPH in liposomes, the DPH molecules are embedded into the hydrophobic core of the membranes as shown in the inset of Figure 2.11 (b). The DPH molecules in dipalmitoylphosphatidylcholine liposomes show a dramatic change of fluorescence anisotropy at 41 °C (Figure 2.11 (b)). This indicates that the fluctuation of DPH molecules largely increases due to the gel to liquid-crystalline phase transition of the membrane at 41 °C, leading to the

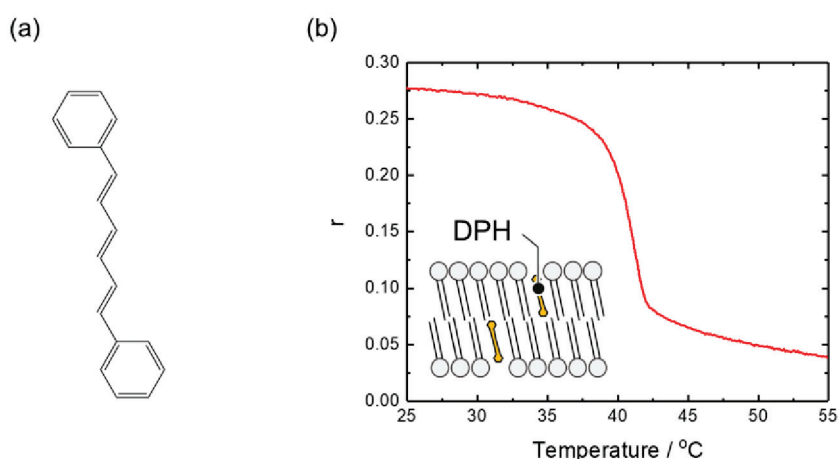


Figure 2.12. (a) Chemical structure of DPH and (b) temperature dependence of fluorescence anisotropy of DPH in dipalmitoylphosphatidylcholine liposome (phase transition temperature: 41 °C).

decrease in fluorescence anisotropy⁵⁰. The fluorescence anisotropy measurements are performed using fluorescence spectrophotometer (FP-8300, Jasco, Japan).

2.6 Calcein dye leakage assay

Calcein-loaded liposomes are widely used to investigate pore formation in liposomes^{51,52}. Figure 2.13 (a) shows the chemical structure of calcein. Calcein molecules exhibit a peak absorption at 490 nm and a peak fluorescence at 520 nm (Figure 2.13 (b)). The intensity of calcein fluorescence depends on the concentration of calcein (Figure 2.13 (c)). At high concentration, the intensity is low because of self-quenching, but at lower concentration, the intensity becomes

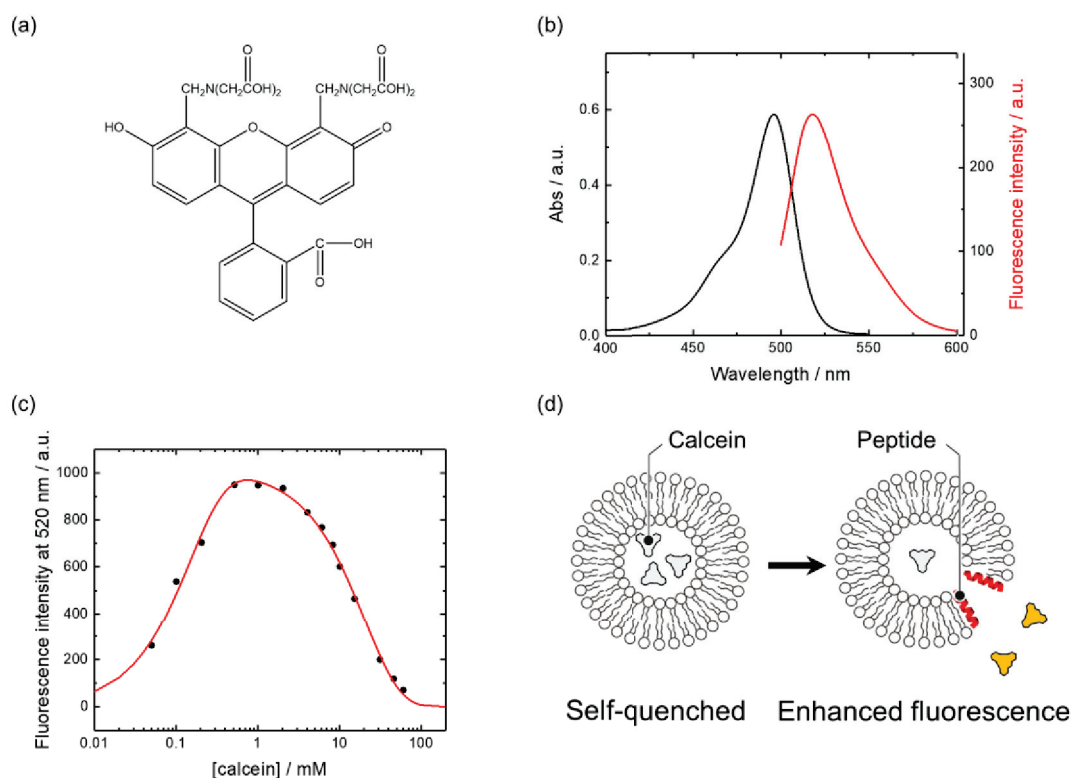


Figure 2.13. (a) Chemical structure of calcein, (b) absorption and fluorescence spectra of calcein, (c) dependence of fluorescence intensity at 520 nm on calcein concentration, and (d) schematic diagram of calcein dye leakage assay. The fluorescence intensity of calcein is enhanced by leakage from liposome through pores induced by membrane-bound peptide.

higher because the quenching is suppressed. The fluorescence of the self-quenched calcein entrapped in liposomes increases when calcein molecules leak out of the liposomes through pores (Figure 2.13 (d)). These properties allow us to investigate pore formation in liposomes^{51,52}. The measurements of calcein fluorescence are conducted using fluorescence spectrophotometer (FP-8300, Jasco, Japan).

2.7 VUVCD-NN prediction

The NN algorithm, which learns the correlation between the amino-acid sequences and the secondary structures of proteins, can be used to predict the positions of secondary structures (α -helix and β -strand) only from the amino-acid sequence of unknown protein. Since VUVCD spectroscopy can provide the information on the secondary-structure content and number of segments with high accuracy, compared with those only from the NN method, the combination of NN and VUVCD methods (VUVCD-NN method) can improve the predictive accuracy of the positions of secondary structures¹⁷. The brief computational protocol is described as following. We utilized an NN algorithm⁵³ that predicts the position of secondary structures using the evolutionary sequence information based on the position-specific scoring matrices generated using the PSI-BLAST tool. A training data set of 607 proteins used in the NN algorithm was obtained from the X-ray structures in the PDB, and the weights and biases of 20 amino acids for α -helices and β -strands were calculated from the secondary structures and amino-acid sequences of these 607 proteins¹⁷. The positions of α -helices and β -strands on the amino-acid sequences were assigned in descending order of the α -helix and β -strand weights of the 20 amino acids until the determined numbers of α -helix and β -strand residues converged to those estimated in the VUVCD analysis. Next, the numbers of α -helix and β -strand segments estimated in the VUVCD analysis were introduced into the NN calculation until the predicted numbers of segments converged to those estimated from VUVCD. In cases where the predicted numbers of residues and segments for α -helices and β -strands did not converge to the VUVCD estimates, the sequence alignment that minimized the difference between the two estimates was taken as the final solution. The predictive accuracy of this method for the positions of α -helix and β -strand segments was 74.9% for 30 reference soluble proteins¹⁷ and 73% for 15 integral membrane proteins,

suggesting that this combination technique will be valuable for predicting the sequences of secondary structures of soluble proteins in the presence of liposomes¹⁷.

Chapter 3: Circular dichroism study of the interaction between α 1-acid glycoprotein and lipid membranes

3.1 Introduction

AGP is a peripheral membrane protein that exhibits characteristic abilities to bind to numerous basic, acidic, and neutral drugs as well as to steroid hormones in the native (N) state^{25,26}, but this binding capacity decreases due to interactions with the membrane that induce the $\beta \rightarrow \alpha$ conformational change. This feature of AGP is believed to relate with the molecular mechanism of drug delivery by AGP. X-ray crystallography has revealed that unglycosylated human recombinant AGP has a β -barrel conformation⁵⁴ (Figure 3.1). However, the tertiary structure of AGP in the membrane and the interaction mechanism of AGP and membrane have not been characterized well.

The secondary structure of AGP in the native (N) state has been investigated using CD, Raman, and Fourier-transform infrared (FTIR) spectroscopy to reveal the binding sites of drugs and the structure-function relationships of AGP^{1,55-60}. CD spectroscopy has been used to analyze the structure of AGP in lipid membranes because it is very sensitive to local peptide structures and applicable to any size of protein at a low concentration under various experimental conditions, such as in the presence of a membrane³⁶. Nishi et al measured the CD spectrum of AGP from 250 to 200 nm in reverse micelles and phosphatidylglycerol (PG) liposome in a mildly acidic condition (pH 4.5) and confirmed that the β -barrel structure of AGP transformed to the α -helix-rich conformation^{1,55}. In experiments using Trp and His mutants, those authors also found that W25, W160, and H172 were key sites for interacting with the liposome (Figure 3.1)^{55,61}. VUVCD spectroscopy using synchrotron radiation as a light source extended the wavelength range of the CD

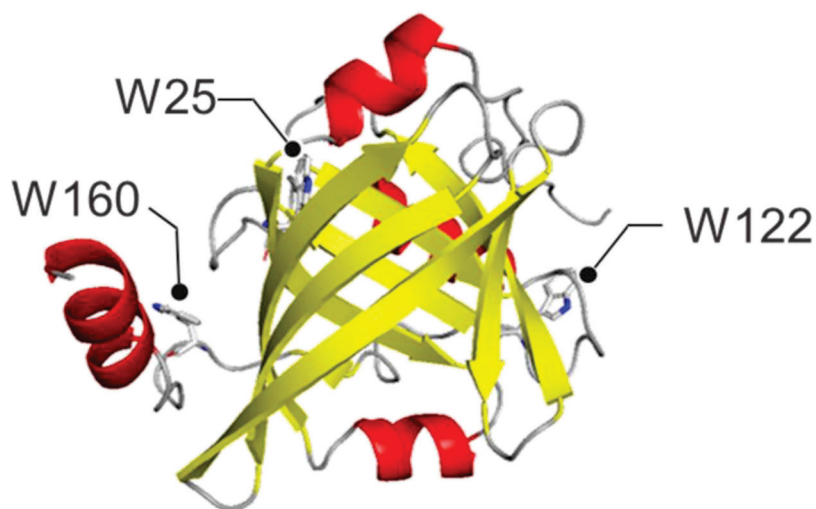


Figure 3.1. Crystal structure of unglycosylated human recombinant AGP (PDB code: 3kq0), which comprises four α -helix and β -strand segments. The types of secondary structures were determined using the DSSP method in which the 3_{10} -helices are assigned as unordered structures. The positions of W25, W122, and W160 are also shown.

measurements of AGP down to the vacuum ultraviolet region (~ 160 nm) and allowed us to accurately estimate the secondary-structure contents and numbers of segments in the PG liposome^{15,16,18}. These secondary-structure parameters were combined with an NN (VUVCD-NN) method to characterize the positions of secondary structures of the membrane-bound conformation of AGP. The findings suggested that the N-terminal helix including W25 and the C-terminal helix including W160 and H172 can interact with the surface of PG liposome¹⁸. However, the mechanism of interaction between AGP and lipid membranes remains controversial because the membrane-bound conformation of AGP has been analyzed only in the presence of PG liposome, whereas the conformation depends on the constituent phospholipid molecules of liposomes^{62,63}, while the roles of the two helical regions predicted as the membrane interaction sites have not been fully considered.

This study characterized the membrane interaction sites and the mechanism of interaction between AGP and lipid membranes by applying VUVCD spectroscopy

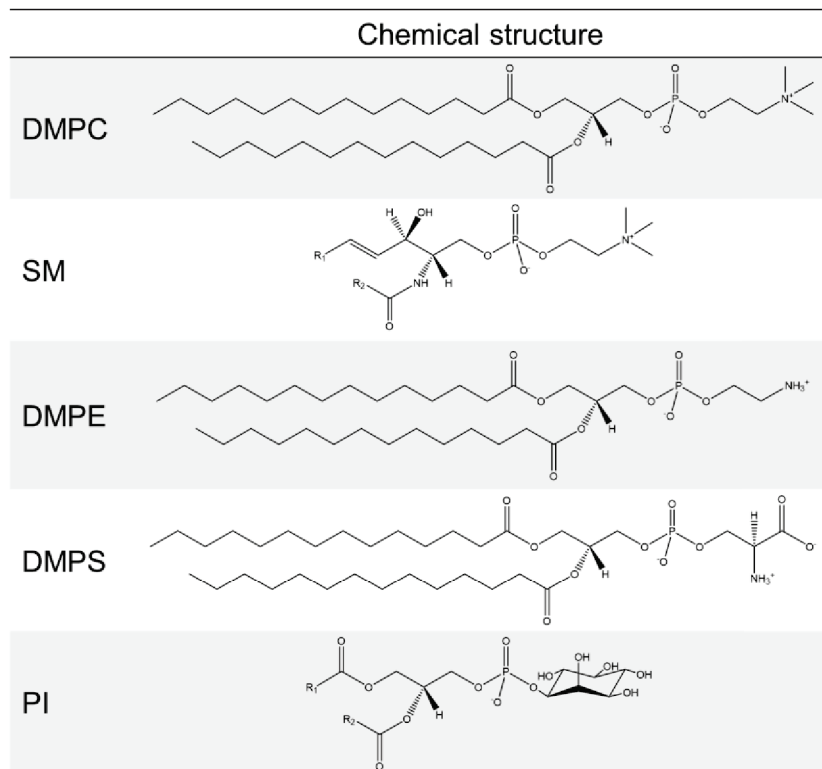
to the conformation analysis of AGP in the presence of five types of liposomes. The constituent phospholipid molecules of the liposomes are major components of human cells⁶⁴ and have different molecular characteristics in the head groups (e.g., different net charges), giving unique properties to the liposome surface. The secondary structures of different membrane-bound conformations of AGP according to the types of liposomes were characterized at the amino-acid sequence level, and the interaction mechanism was investigated in terms of hydrophobic and electrostatic interactions.

3.2 Experimental

Materials

AGP from human plasma (Cohn fraction VI) was purchased from Sigma (St. Louis, MO). Dimyristoyl phosphatidylcholine (DMPC), sphingomyelin (SM), dimyristoyl phosphatidylethanolamine (DMPE), dimyristoyl phosphatidylserine (DMPS), and phosphatidylinositol (PI), which are major membrane components of human cells⁶⁴, were obtained from Avanti (Alabaster, AL). Their chemical structures are shown in Table 3.1. These phospholipid molecules had purities of >98%. AGP was dissolved in 20 mM sodium phosphate buffer (pH 7.4) or in 20-mM sodium acetate buffer (pH 4.5), and the solutions were exhaustively dialyzed against the same buffer at 4°C. The dialyzed protein solutions were centrifuged at 14 000 rpm for 15 minutes and filtered by a membrane with a pore size of 20 µm (DISMIC 25AS020AS, ADVANTEC, Tokyo) to remove aggregates. The AGP concentration was determined by measuring the absorption (V-560, Jasco, Tokyo) using the molar extinction coefficient of 33,074 M⁻¹ cm⁻¹, which was estimated from extinction coefficient of 8.93 dL (g cm)⁻¹ at 278 nm⁵⁵ and total mass of AGP. This molar extinction coefficient was close to that calculated from the amino-acid sequence of AGP (33,140 M⁻¹ cm⁻¹ at 280 nm)⁶⁵. The DMPC, SM, DMPE, DMPS, and PI liposomes were prepared by the extrusion technique. The liposome vesicles were mixed with protein solution at final concentrations of 50 µM protein and 3 mM phospholipid (i.e., molar ratio of protein to phospholipid of 1:60)^{1,18}. The protein-liposome mixtures were incubated at room temperature overnight before performing the VUVCD measurements.

Table 3.1. Chemical structure of phospholipids used in this study. R₁ and R₂ mean fatty acyl chains.



VUVCD measurements

The VUVCD spectra of AGP in the presence or absence of liposomes were measured from 260 to 170 nm using the VUVCD spectrophotometer in the HiSOR and an assembled-type optical cell at 25°C. The path length of the optical cell was adjusted with a Teflon spacer to 10.6 μm. All of the VUVCD spectra were recorded with a 1.0-mm slit, a 4-s time constant, a 20-nm min⁻¹ scan speed, and using four to nine accumulations. The optical cell was located within 10 mm of the photomultiplier so as to minimize the effects of light scattering from the liposome particles^{14,66}. The secondary structures of proteins in the presence or absence of liposomes were analyzed using the SELCON3 program^{67,68} and the database of VUVCD spectra of 31 reference proteins with known X-ray structures^{15,16}. These reference proteins are water-soluble, but they would be suitable for liposome-

bound systems because there was no evidence of wavelength shifts between the CD spectra of soluble and membrane proteins¹². However, the $n\text{-}\pi^*$ and $\pi\text{-}\pi^*$ transitions originating from the peptide group might be affected by membrane environments in which the dielectric constant is much lower than that for water⁶⁹. The numbers of α -helix and β -strand segments were calculated from the distorted α -helix and distorted β -strand contents, respectively⁶⁸. The positions of α -helices and β -strands on the amino-acid sequence were predicted using the VUVCD-NN combination method.

3.3 Results

The VUVCD spectra of AGP were measured from 260 to 170 nm using a VUVCD spectrophotometer in the N state at pH 7.4 and in the presence of DMPC, SM, DMPE, DMPS, and PI liposomes—corresponding to DMPC, SM, DMPE, DMPS, and PI states, respectively—at pH 4.5. The conformational differences of AGP between pH 7.4 and 4.5 would be minor since its secondary structures were found to be only slightly modified over the pH range from 10 to 4.5^{18,57}. The VUVCD spectra for each liposome solution were also measured as the baseline, which was subtracted as the background from the spectra of mixtures of AGP and liposome. All of the VUVCD spectra including the baselines of liposome solutions were constant within an experimental error of 5% during data acquisition, which took about 1 hour. Thus, the obtained spectra are available for analyzing the liposome-induced conformational changes in AGP.

3.3.1 Vacuum-ultraviolet circular dichroism spectra of membrane-bound states

Figure 3.2 shows the VUVCD spectra of AGP in the N state and the DMPC, SM, DMPE, DMPS, and PI states, which were obtained by subtracting the spectra of the glycan chain from the observed spectra of AGP, based on the weight proportion of protein and glycan in AGP as described previously¹⁸ and in Figure 3.3.

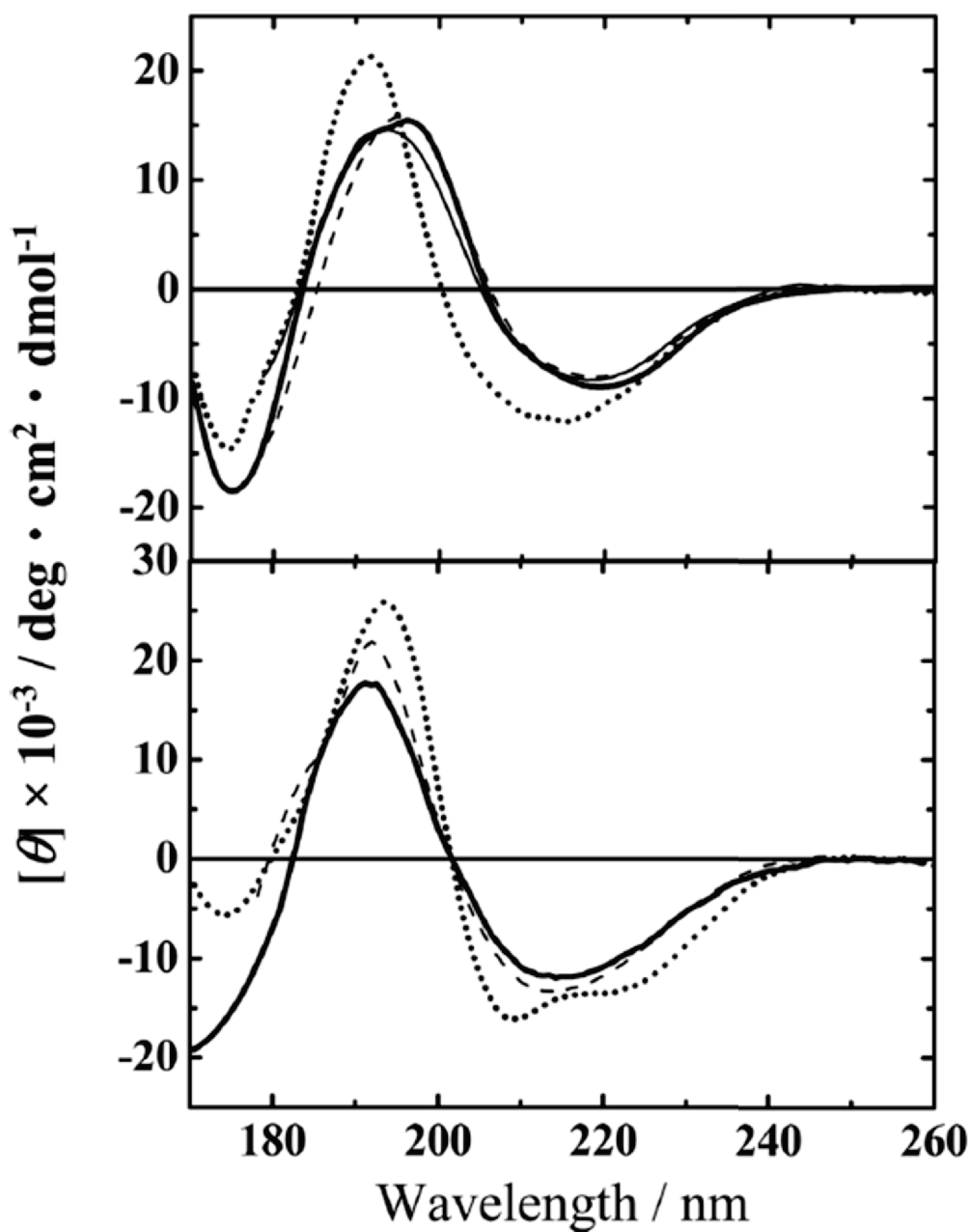


Figure 3.2. VUVCD spectra of AGP in the N state and the MB states at 25°C: (a) N state (thick line), DMPC state (thin line), SM state (dashed line), and DMPE state (dotted line), and (b) DMPS state (solid line), PI state (dotted line), and PI state for 1 M NaCl (dashed line). The solvents were 20-mM sodium phosphate buffer (pH 7.4) for the N state and 20-mM sodium acetate buffer (pH 4.5) for the MB states.

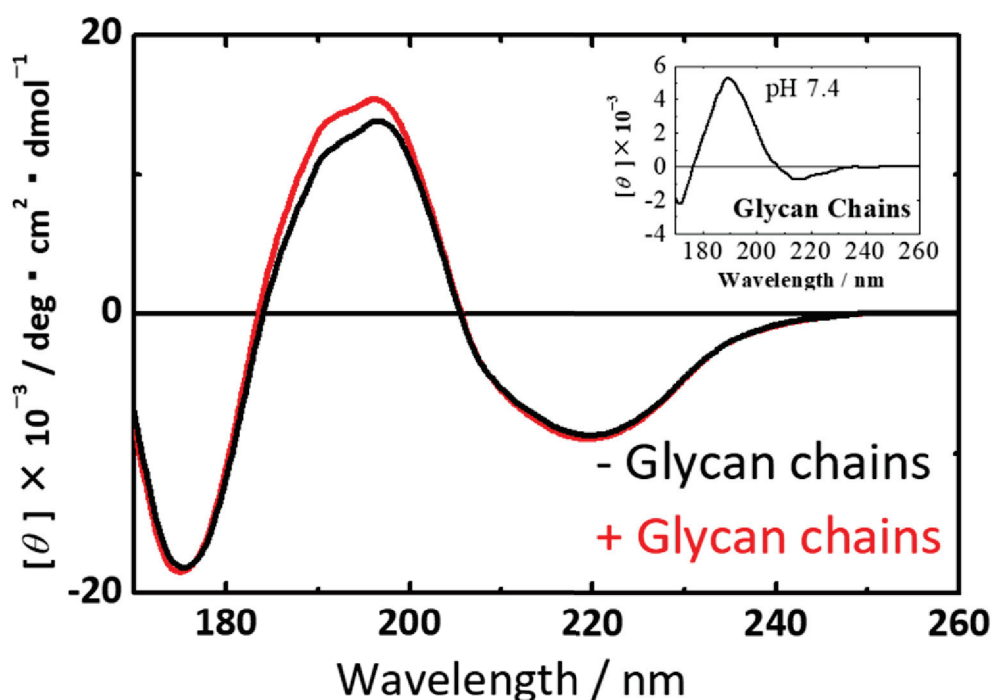


Figure 3.3. VUVCD spectra of AGP with and without glycan chains at pH 7.4. The VUVCD spectrum of the glycan moiety of AGP shown in the inset was calculated by a linear summation of the CD spectra of all the constituent sugars using their weight proportions in the glycan chains: 0.6% fucose, 8.5% galactose, 7.4% mannose, 16.27% GlcNAc, and 10.03% NeuNAc⁷⁰. First, the obtained AGP spectrum was converted to the ellipticity unit per total molecular weight of the protein and glycan moieties. Second, the CD spectrum of the glycan chain was converted to the ellipticity unit per total molecular weight of the glycan chain, and the obtained ellipticities were subtracted from the ellipticities of AGP spectrum. In this way, the obtained spectra of the protein moiety of AGP were divided by the number of amino-acid residues (183) to convert the spectra to the molar ellipticity unit¹⁸.

The five phospholipid molecules used in this study (DMPC, SM, DMPE, DMPS, and PI) have characteristic head groups (Table 3.1) located on the surface of the liposome because they have affinity to the hydrophilic region or aqueous solution, meaning that the molecular characteristics of head groups such as differences in

the net charge could affect the properties of the liposome surface⁷¹. The net charge of a liposome surface would be neutral in DMPC, SM, and DMPE because the negative charge in the phosphate group would be canceled by the positive charges of the choline of DMPC and SM and of the ethanolamine of DMPE. The DMPS and PI liposomes have negatively charged surfaces because the negative charge of the phosphate group could be retained due to the serine with zwitterions for DMPS and inositol without any charge for PI.

The VUVCD spectra of AGP in the N state and in the DMPC, SM, and DMPE states are shown in Figure 3.2A. The native AGP exhibited one positive peak around 195 nm and two negative peaks around 220 and 175 nm, which are characteristic peaks of β -strand-rich proteins^{15,16}. These characteristic peaks were mostly retained in the DMPC and SM states. However, the positions of peaks in the spectrum in the DMPE state were blue-shifted compared with those in the N, DMPC, and SM states, exhibiting two negative peaks around 215 and 175 nm and one positive peak near 190 nm as the CD intensity increased.

The VUVCD spectra of AGP in the DMPS and PI states are shown in Figure 2B. The DMPS state exhibited a spectrum similar to that observed in the DMPE state, although the two spectra differed markedly below 180 nm. The PI state resulted in a large spectral change, showing three negative peaks at 222, 208, and 175 nm and a positive peak at 195 nm, which are characteristic of α -helix-rich proteins^{15,16}. These spectral characteristics were similar to those found previously in the PG state¹⁸. To confirm the effect of oriented CD (OCD)⁷², the CD spectrum of AGP in the PI state was measured from 260 to 198 nm with 200- μ m path length and compared that measured with 10.6- μ m path length as shown in Figure 3.4. Evidently, the both spectra were consistent in the overlap region, suggesting that the effect of OCD would be small or even negligible in the PI state. Thus, the spectra of AGP were highly dependent on the molecular characteristics of head groups of the constituent phospholipid molecules in the liposomes, which affected the conformations of AGP.

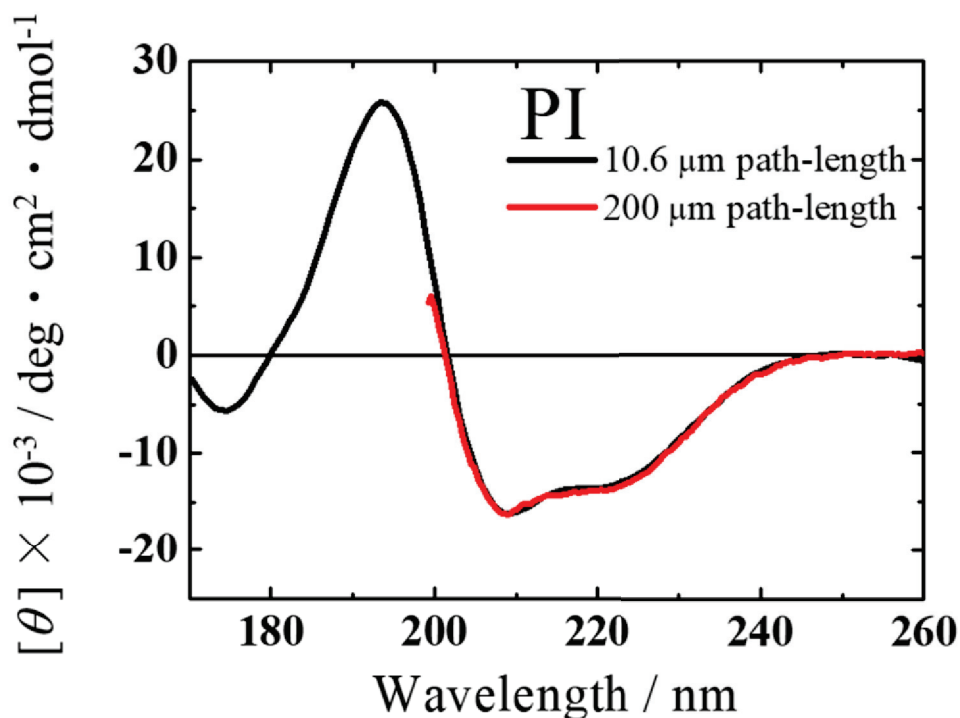


Figure 3.4. The CD spectra of AGP in the PI state measured with 10.6 μm and 200 μm path-length cell at 25°C. The both spectra are mostly identified, meaning that the effect of oriented CD was small or even negligible in this study.

3.3.2 Secondary structures of membrane-bound states

The secondary-structure contents and numbers of segments of AGP in the N state and in the DMPC, SM, DMPE, DMPS, and PI states estimated from VUVCD spectra from 260 to 170 nm (Figure 3.2) are listed in Table 3.2. The results for the crystal structure are also listed in this table for comparison⁵⁴. The missing residues 176 to 183 in the crystal structure were considered as the unordered structures. The types of secondary structures in this study were determined using the DSSP method⁷³, in which the 3_{10} -helices were assigned as unordered structures (see Section 2).

Table 3.2. Secondary-structure contents and numbers of segments of AGP in the N state and in the DMPC, SM, DMPE, DMPS, and PI states.

	Percentage Content				Numbers of Segments	
	α -helix	β -strand	Turn	Unordered	α -helix	β -strand
N state						
X-ray	18.0	39.3	15.9	26.8	4	9
VUVCD	17.2	37.8	22.7	23.1	4	11
Membrane-bound state						
DMPC	19.0	37.5	21.5	21.9	5	11
SM	18.1	40.4	21.0	21.4	4	11
DMPE	37.7	16.9	18.1	28.9	5	7
DMPS	28.9	18.6	21.4	30.9	6	6
PI	45.8	6.8	17.9	31.2	7	3
PI + NaCl	40.0	14.7	20.1	27.2	7	4

As listed in Table 1, the contents of α -helices, β -strands, turns, and unordered structures of native AGP were 17.2%, 37.8%, 22.7%, and 23.1%, respectively, which were very similar to those estimated previously¹⁸ and the crystal structure of unglycosylated recombinant AGP (18.0%, 39.3%, 15.9%, and 26.8%, respectively)⁵⁴. This suggests that the effect of glycan chains on the secondary structures of AGP are small or even negligible. Further, 4 and 11 helix and strand segments, respectively, were found using VUVCD, with 4 and 9 found using X-ray crystallography, showing that combining the VUVCD method with the SELCON3 program⁶⁷ can successfully estimate the secondary-structure contents and numbers of segments of AGP in the N state.

The secondary-structure contents and numbers of segments in the DMPC and SM states are mostly consistent with those in the N state, as expected from the similarity of their VUVCD spectra. In the DMPE, DMPS, and PI states, it is evident that the contents of α -helices and β -strands uniquely increased and decreased, respectively, inducing the $\beta \rightarrow \alpha$ conformational change although the components of secondary structures differed among them (37.7% and 16.9%, respectively, in the DMPE state, 28.9% and 18.6% in the DMPS state, and 45.8%

and 6.8% in the PI state). This suggests that the conformation of AGP is very sensitive to differences in the molecular characteristics of liposome surfaces.

3.3.3 Positions of secondary structures in membrane-bound states

Figure 3.5 shows the positions of α -helices, β -strands, and other structures of AGP in the N state and in the DMPE, DMPS, and PI states predicted by the VUVCD-NN method, together with the N state as determined from X-ray data. The secondary-structure sequences in the DMPC and SM states are not shown in this figure because they were similar to those in the N state. We first compared the sequence data between the VUVCD and X-ray estimates. Four helical segments in the N state estimated by the VUVCD-NN method were assigned as residues 16 to 21, 36 to 44, 135 to 145, and 167 to 175; these helical segments corresponded to

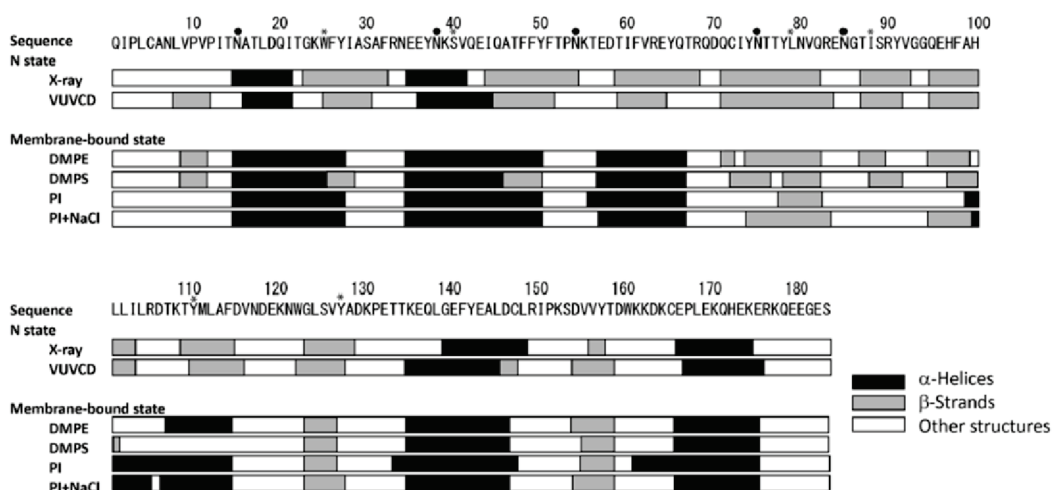


Figure 3.5. Sequence-based secondary structures of α_1 -acid glycoprotein (AGP) in the N, DMPE, DMPS, and PI states predicted using the VUVCD-NN method. The sequence of native AGP was also estimated from X-ray data for comparison. The residues marked with filled circles (●) and asterisks (*) correspond to the glycan and predicted ligand-binding sites, respectively

residues 15 to 21, 35 to 41, 139 to 148, and 166 to 174, respectively, identified in the X-ray data. Further, the positions of β -strands other than the N-terminal strand (residues 8-10) were also consistent with the results from the X-ray data, resulting in a total prediction accuracy of the sequences between the X-ray and VUVCD-NN estimates in the N state of 80% in terms of the success rate (quantified as the Q3 value)⁷⁴. These results suggest that the VUVCD-NN method used in this study would be a useful tool for monitoring the conformational changes in AGP induced by the addition of liposomes.

The DMPE, DMPS, and PI states had characteristic conformations consisting of some long α -helices and small β -strands (Figure 3.5). The positions of six α -helix segments in the DMPE state were assigned as residues 15 to 27, 35 to 50, 57 to 66, 107 to 114, 135 to 146, and 166 to 175, which are denoted as A-, B-, C-, D-, E-, and F-helices, respectively. The positions of five α -helices in the DMPS state were assigned as residues 15 to 25, 35 to 46, 57 to 66, 135 to 146, and 166 to 175, which are denoted as A-, B-, C-, E-, and F-helices, respectively. Further, the regions of six α -helices in the PI state were assigned as residues 15 to 27, 35 to 50, 56 to 66, 99 to 114, 133 to 147, and 161 to 175, which are denoted as A-, B-, C-, D-, E-, and F-helices, respectively. These results suggest that the AGP formed characteristic conformations depending on the liposomes, although the A-, B-, C-, and E-helix segments were in similar positions among the three states. It is unclear whether these helical formations were affected by five glycan chains linked to Asn-15, -38, -54, -75, and -85, but the types of secondary structures at these linkage sites were mostly conserved in the conformational changes in AGP (Figure 3.5). The numbers of segments predicted at the sequence level did not necessarily agree with those predicted from VUVCD data because sequence-alignment minimization was performed in the VUVCD-NN method¹⁷.

3.3 Discussion

This study found that the VUVCD spectra of AGP in the N state and in the DMPE, DMPS, and PI states (Figure 3.2) provided detailed information about the secondary structures, in terms of not only the contents and numbers of segments (Table 3.2) but also their positions on the amino-acid sequence (Figure 3.5). Although this secondary-structure information could not be used to determine the

tertiary structure of the membrane-bound conformation of AGP and the liposomes used in this study were model membranes constructed from simple phospholipid molecules, the structural data of membrane-bound AGP including the positions of secondary structures can be used in discussions of the membrane interaction sites and the mechanism of interaction between AGP and lipid membranes at the sequence level.

Knowledge of the membrane interaction sites of AGP is important for understanding the mechanism of interaction between AGP and lipid membranes. Previous studies^{1,18} found that the N- and C-terminal helices in the PG state, which are residues 15 to 27 and 161 to 175, respectively, are candidate sites for the interactions. In the present study, the two helices at the N- and C-terminals were designated as A- and F-helices, respectively. The A-helix in the N state was markedly extended in the three states (residues 15-25 or 26), but the F-helix was only extended in the PI state (residues 161-175). We examined the characteristics of A- and F-helices in the DMPE, DMPS, and PI states to confirm the possibility of them acting as interaction sites. The net charges of the A- and F-helices were calculated to be 0 and -1, respectively, for DMPE, 0 and -1 for DMPS, and 0 and +1 for PI, based on the numbers of acidic (Asp and Glu) and basic (Lys, Arg, and His) residues in each helix segment. These net charges would increase slightly because the carboxyl groups of Asp and Glu residues ($pK_a \approx 4$) are not completely ionized at pH 4.5. Further, according to the HELIQUEST program⁷⁵, the A-helix segments in the three states comprised the localized polar and nonpolar surfaces as seen in the amphiphilic helix, indicating that the localized nonpolar surface could interact with the hydrophobic moiety of the membrane. Further, the F-helix had a positively charged region in the PI state, suggesting that the negatively charged liposome surface would interact with the positively charged F-helix in that state. These results indicate that the candidate membrane interaction sites would be the amphiphilic A-helix in the DMPE, DMPS, and PI states and the positively charged F-helix in the PI state. Another candidate would be the D-helix (residues 99-114) in the PI state because this region had a positive net charge, which could induce an interaction with the negatively charged liposome, and moreover, half of all of the residues of this helix are hydrophobic amino acids. However, this region comprises a core with a β -barrel conformation in native AGP, which might make it difficult to interact directly with the liposome. It is likely that the region of the D-helix in the PI state would form a helical structure after the A- and F-helices interacted with the liposome.

As mentioned above, AGP includes three Trp residues (W25, W122, and W160) (Figure 3.1), and W25 and W160 are known to be crucial residues for membrane interactions in the PG state¹. W25 is the constituent residue of A-helices in the DMPE, DMPS, and PI states, while only W160 is involved with the F-helix in the PI state. To characterize the two membrane interaction sites (A- and F-helix

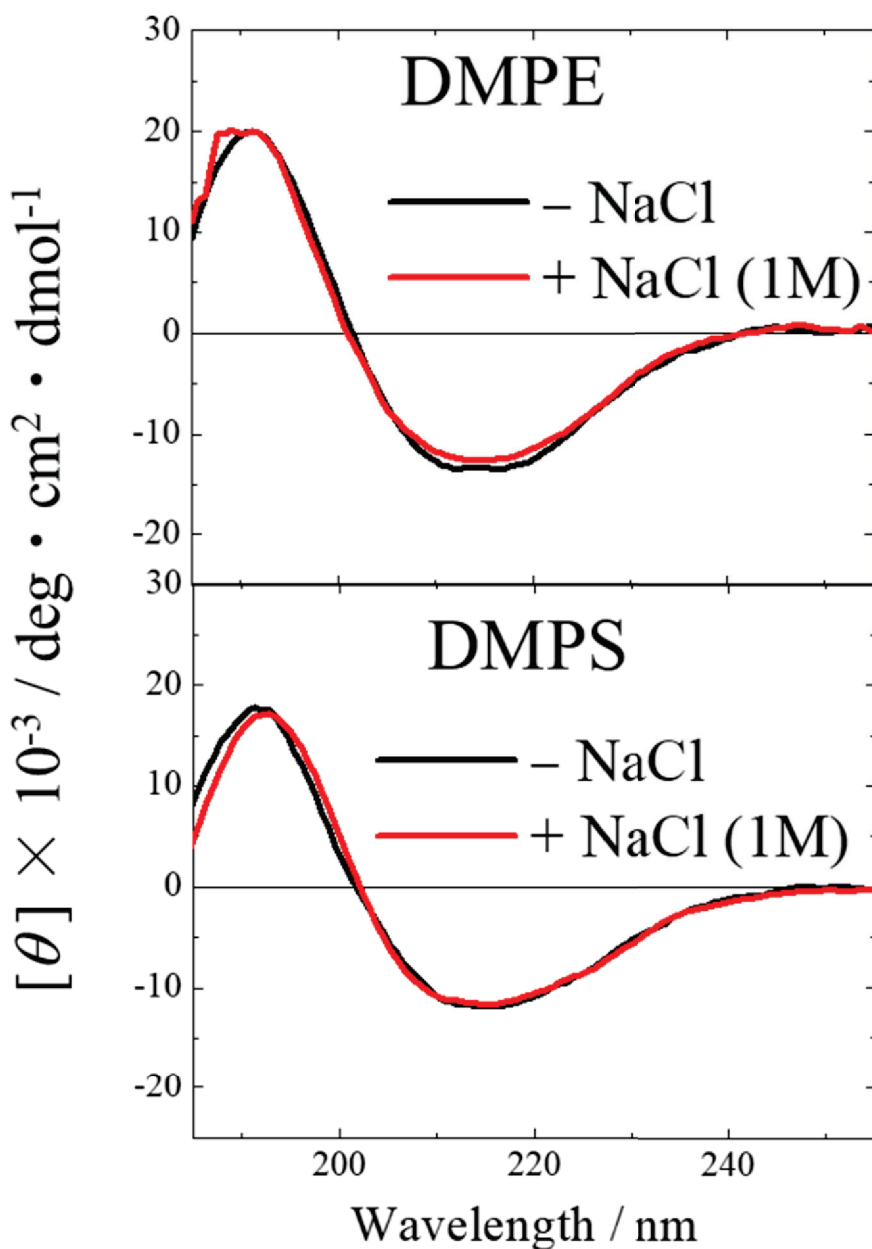


Figure 3.6. VUVCD spectra of AGP in the DMPE and DMPS states in the presence or absence of 1M NaCl at 25°C.

regions), we investigated the effect of salt on the conformation of AGP in the DMPE, DMPS, and PI states. The VUVCD spectra of AGP in the DMPE, DMPS, and PI states in the presence of 1 M sodium chloride (NaCl) are presented in Figure 3.6 (DMPE and DMPS states) and Figure 3.2B (PI state). Spectral changes were not observed in the DMPS and DMPE states, but they were observed in the PI state. It was particularly interesting that the spectrum in the PI state for the NaCl solution was similar to those in the DMPE and DMPS states. Salt is known to reduce the electrostatic interactions between proteins and membranes⁷⁶⁻⁷⁸, implying that the electrostatic interaction exists in the PI state.

The positions of conformational changes in the PI state due to the addition of NaCl were addressed by predicting the secondary-structure sequence, as shown in Figure 3.5. It is evident that the F-helix shortened in the PI state to have the same length as in the DMPE and DMPS states. This result is reasonable given that the F-helix involved in W160 would be expected to interact with the liposome surface

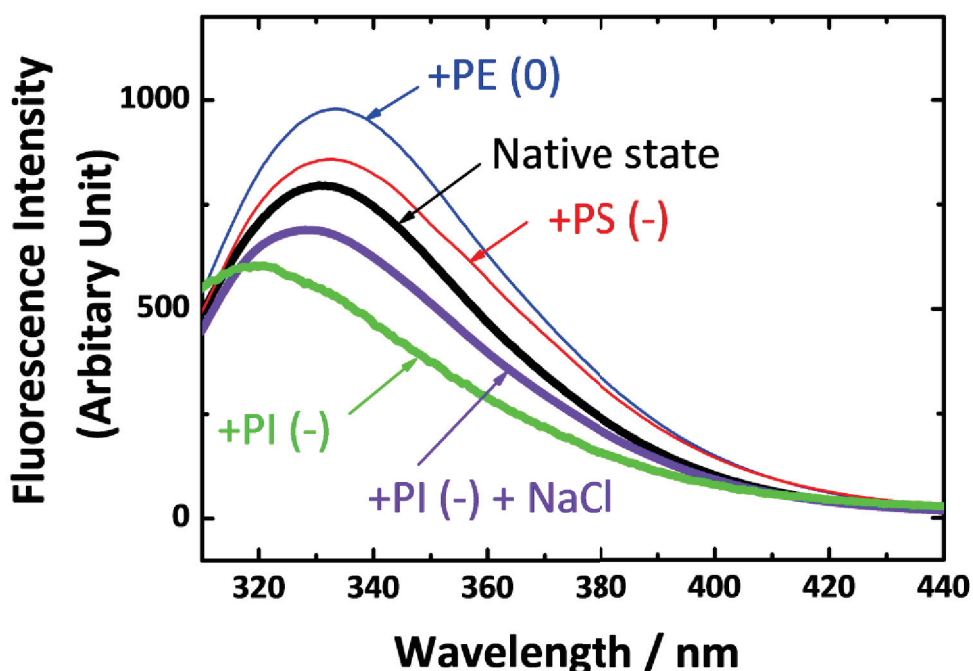


Figure 3.7. The fluorescence spectra of AGP in the N state and in the DMPE, DMPS, and PI states from 440 to 310 nm, which were recorded using a fluorescence spectrophotometer (FP-8000, Jasco, Japan) with excitation at 280 nm, a 1-nm resolution, a 10-nm slit width, a 1-s time constant, and a 100-nm min⁻¹ scan speed

via electrostatic interactions and that the addition of salt would reduce this interaction. Similar results were obtained in the fluorescence spectra, in which the position of the peak in the PI state was blue-shifted compared with that in the DMPE state, but the peak returned to the positions in the DMPE state when NaCl was added to the PI state (Figure 3.7), directly reflecting the change in the environment around W160⁷⁹. Further, the length of A-helix including W25 was maintained in the PI states with 1 M NaCl, which is probably due to the amphiphilic A-helix strongly interacting with the liposome surface via hydrophobic interactions.

Based on these characteristics of the membrane interaction sites of AGP, this protein has at least two interaction sites with membrane: the amphiphilic A-helix and the positively charged F-helix. It is known that the protein-membrane interactions mainly comprise electrostatic interactions between the anionic head groups of lipids and the positively charged protein or regions of protein and the subsequent penetration of some hydrophobic regions of the protein into the membrane⁸⁰. However, as mentioned above, although the DMPC, SM, and DMPE liposomes have a neutral net charge on their surface, the membrane interaction of AGP was induced only in the DMPE state.

Phosphatidylethanolamine (PE) contains an ethanolamine head group rather than the choline one present in phosphatidylcholine and SM. It is reported that this substitution changes many properties of the phospholipid. Litzinger and Huanget showed that one of the main differences between dioleoyl phosphatidylethanolamine (DOPE) and dioleoyl phosphatidylcholine (DOPC) is that DOPE tends to forming nonbilayer structures, such as in the hexagonal H_{II} phase, whereas this activity is absent in DOPC⁸¹. This effect of not forming a bilayer in DOPE can decrease the head-group pressure and allow a peripheral membrane protein to access the inside of the liposome, which contains a negatively charged phosphate group⁸². Although the effect of not having a bilayer might be small at 25°C because the hexagonal H_{II} phase in the mixture of dielaidoyl PE and DOPE constituted 100% of the population at 50°C but this decreased to about 10% at 25°C⁸³, AGP might weakly interact with the nonrigid surface of the PE liposome via interactions between the positively charged AGP and the negatively charged internal phosphate group.

PI includes myoinositol in its head group, which has six hydroxyl groups (Table 3.1) with a strong affinity to aqueous solutions. Nishi et al investigated the

conformation of AGP at pH 4.0 in various alcohol solutions as a membrane-mimicking environment and found that the hydroxyl group of the alcohol only plays a role in the dissolution in water and that the formation of α -helix is induced by the hydrocarbon moiety⁸⁴. Although alcohol and inositol molecules have markedly different structures, it seems that the hydroxyl group itself does not contribute to the helical conformation, meaning that the negative charged liposome surface contributed strongly to the conformational changes in AGP in the PI state. On the other hand, the DMPS and PI liposomes should have negatively charged surfaces, but they induced different conformations. Moncelli et al suggested that the charge density of the phosphatidylserine (PS) lipid film changed from slight negative to slight positive values over the pH range from 7.5 to 3 due to the anomalous behavior of the phosphate group⁸⁵. Therefore, the effect of the negative net charge of the PS liposome is reduced in a mildly acidic condition (pH 4.5) compared with that of the PI liposome. These slight differences in the net charge might induce differences in the conformations between the DMPS and PI states.

Thus, the physical properties of each of the DMPE, DMPS, and PI liposomes are very complicated and depend on the experimental conditions, but their individual uniqueness would induce characteristic membrane-bound conformations in the three states. However, it is conceivable that the interaction mechanism would be similar among the DMPE, DMPS, and PI states because all three states formed A-helix segments, but there would be an additional step in the PI state. In the DMPE and DMPS states, the positively charged AGP molecule (pI=2.8-3.8) approaches the anionic regions in the membrane surface via an electrostatic interaction and the A-helix region including W25 is formed on the membrane surface via the hydrophobic interaction, followed by the formation of other helices. In the PI state, in addition to the interaction processes and the formation of A-helix observed in the DMPE and DMPS states, the F-helix region near W160 was formed weakly in contact with the membrane surface via the electrostatic interaction, followed by the formation of other helices. From the viewpoint of the protein-mediated uptake mechanism of drugs, the formation and extension of A-helix would be crucial for releasing neutral drugs because W25 is known to be the most-important site for binding with drugs such as progesterone via the molecular docking and the induced CD spectra of drug-AGP complex (Figure 3.5)^{54,86}.

These unique interaction mechanisms are still speculative, and it might be difficult to confirm further experimentally. However, additional techniques for investigating membrane interactions such as fluorescence quenching⁷⁹, mass spectroscopy⁸⁷, and site-directed spin labeling and electron paramagnetic resonance spectroscopy⁸⁸ could also be useful for elucidating more details about the mechanism of interaction between AGP and cell membranes.

In summary, we have used VUVCD spectroscopy to characterize the conformation of AGP in the presence of liposomes and revealed that N- and C-terminal helices could interact with the membrane via hydrophobic and electrostatic interaction, respectively.

Chapter 4: Circular dichroism and molecular dynamics studies of the interaction between myelin basic protein and phosphatidylinositol membrane

4.1 Introduction

The myelin sheath is a unique multilayered membrane surrounding the axon of neurons in which the cytoplasmic and extracellular regions alternately and compactly accumulate⁸⁹. This unique structure of myelin provides several neurological functions, including saltatory conduction, nervous metabolism, and regulation of ion and water homeostasis^{90,91}. Damage to the myelin sheath or demyelination leads to serious neurological diseases such as multiple sclerosis^{92,93}. Elucidating the formation and stabilization processes of the myelin sheath are crucial for understanding the mechanisms underlying the manifestations of these neurological diseases.

The 18.5-kDa isoform of MBP is the second-most-abundant protein in the myelin sheath^{27,28}. MBP is an intrinsically disordered protein in solution and in the N state⁹⁴, but it can form an ordered structure when interacting with the membranes in the cytoplasmic side in the myelin sheath to contribute to the stabilization and formation of the myelin sheath^{2,29}. The conformations of MBP in the membrane-bound state (MB-state) have previously been investigated using NMR, fluorescence resonance energy transfer, CD spectroscopy, and small-angle X-ray scattering in various membrane environments, including liposomes (bilayer membrane), micelles, and alcohol solutions⁹⁵⁻⁹⁹. Further, the contributions of the membrane net charge to the MBP-membrane interactions have been examined using various types of liposomes with different head groups of phospholipid

molecules such as choline, ethanolamine, serine, and glycerol groups at pH values from 4 to 10^{22,100-102}. The conclusions from these studies include that at least three segments of MBP located in the N-terminal, central, and C-terminal regions of MBP could form amphiphilic helices on the membrane, and that the membrane and MBP mainly interact electrostatically via positively charged residues of MBP and negatively charged head groups of acidic phospholipids in the membrane, followed by hydrophobic interactions^{2,29,30}. However, the conformations of MBP in the MB-states strongly depend on the lipid compositions of liposomes and the types of mimic membrane^{2,29,30}, which makes it difficult to comprehensively understand the membrane-bound conformation and the membrane-interaction sites of MBP.

PI lipid molecules with negatively charged head groups, which are components of myelin membrane, are crucial elements for the MBP-membrane interactions¹⁰³. The molar ratio of PI on the cytoplasmic side of the myelin membrane is only about 2% in all lipids¹⁰⁴, but it is involved in various functions crucial to sustaining life such as signal transduction, stabilization of myelin, and glial metabolism^{100,103,105}. In addition, phosphatidylinositol-4,5-bisphosphate (PIP2), which is a phosphorylated form of PI, is recognized as a membrane target of MBP that is tightly colocalized with MBP^{103,105}. It is already known that the PI membranes including phosphatidylinositol-4-phosphate (PIP) and PIP2 exhibit strong interactions with MBP, inducing the structural alteration from coils to helices^{106,107}. Hence, knowledge of the lipid constituents of PI, PIP, and PIP2 would be useful for characterizing the membrane-bound conformation of MBP.

This study measured the VUVCD spectra of MBP down to 178 nm in the presence of liposomes comprising PI, PIP, or PIP2 lipid molecules to characterize the positions of helix segments in the membrane-bound conformation of MBP at the level of amino-acid sequences. The peptide segments related to these characterized helix regions were also analyzed in MD simulations of the bilayer membrane to confirm whether these regions are where membrane interactions occur. This study also combined the VUVCD and MD methods to investigate how each helix region interacts with the membrane (via electrostatic and/or hydrophobic interactions) in terms of the distances of amino-acid residues from the membrane surface.

4.2 Experiment and Theory

Materials

MBP from bovine brain was purchased from Sigma (St. Louis, MO). L- α -PI from soy, L- α -PIP from porcine brain, and L- α -PIP2 from porcine brain, DMPC, and DMPS were purchased from Avanti (Alabaster, AL). The chemical structures and net charge of head groups of these phospholipids are listed in Table 4.1. All other chemicals were of analytical grade and obtained from Sigma. MBP was dissolved in 10 mM phosphate buffer (pH 6.8) or 20 mM sodium acetate buffer (pH 4.5), and the protein solution was centrifuged at 15,000 rpm for 10 minutes to remove the protein aggregates. The supernatant solution was used for the VUVCD measurements. The MBP concentration was carefully determined by analyzing amino acids and measuring absorptions (V-560, Jasco, JPN) (the molar extinction coefficient at 276 nm was $1.73 \times 10^5 \text{ M}^{-1} \text{ cm}^{-1}$). A mildly acidic state (A-state, pH 4.5) was used as the environment for the membrane interactions of MBP in this

Table 4.1. Chemical structures of phospholipids used in this study. R₁ and R₂ mean fatty acyl chains.

	Net Charge	Chemical structure
DMPC	± 0	
DMPS	-1	
PI	-1	
PIP	-2	
PIP2	-3	

study, because protein-membrane interactions are increased at mildly acidic pH without the presence of aggregation or turbidity^{18,101,108}. Liposomes were prepared using an extrusion technique. The filtered vesicles were mixed with protein solution at final concentrations of 30 μM protein and 9 mM lipid (the molar ratio of lipid to protein [L/P] was 300).

VUVCD measurements

The VUVCD spectra of MBP in the N-state (pH 6.8), A-state (pH 4.5), and in the presence of liposomes were measured from 260 to 178 nm with a path length of 50 μm using a VUVCD spectrophotometer⁴⁸. The sample solution was encapsulated in a calcium fluoride optical cell and positioned 10 mm below the photomultiplier window to minimize the effects of light scattering from the liposome particles¹³. The VUVCD spectra of the liposome solutions were also measured as a baseline that was subtracted from the spectra of the mixing solution of MBP and liposome. All of the VUVCD spectra were recorded at 25°C with a 4-seconds time constant, 20-nm min^{-1} scan speed, and 4 to 16 accumulations. The contents of α -helices, β -strands, turns, and unordered structures of MBP in the N-state, A-state, and in the presence of liposomes were estimated from the corresponding VUVCD spectra using the SELCON3 program and a database of VUVCD spectra for 31 reference proteins^{12,15,16,67}. The numbers of α -helix and β -strand segments were calculated from distorted α -helix and distorted β -strand contents, respectively⁶⁷. The positions of α -helix and β -strand segments on the amino-acid sequence were predicted using the VUVCD-NN method¹⁷.

MD simulations of peptide fragments of MBP

The simulation system for the peptide fragments of MBP in the presence of a PI bilayer membrane was generated using the CHARMM-GUI interface¹⁰⁹. We used a highly mobile membrane-mimetic model utilizing a 1.3 scaling factor and an acyl tail comprising six carbon atoms to enhance conformational sampling¹¹⁰⁻¹¹². The initial helix structures were constructed using the Visual Molecular Dynamics package¹¹³. The initial orientation of the helices for the membrane surface were calculated using PPM server¹¹⁴. The N- and C-terminals of the peptides were acylated and amidated, respectively, using the appropriate options in the CHARMM-GUI interface to reduce the kinetic barrier associated with inserting peptides in membranes. The peptide fragment was set to be at least 11 Å above the membrane surface to prevent forced interactions with the membrane¹¹¹. The side

chains of His (pKa 6.0) residues were protonated because the pH value was 4.5 for the membrane-bound condition in this study.

The system including peptide, lipids, and solvents was minimized using a steepest-descent algorithm, followed by six “suggested” equilibration steps¹¹⁰. The production steps were carried out for 250 ns with a 2-fs time step using the GROMACS (Groningen Machine for Chemical Simulations) package and the CHARMM36m force field^{115,116}. The simulations were performed using the NPAT ensemble, in which temperature (25°C) and pressure (1 bar) were maintained using a Nose-Hoover thermostat and Langevin barostat, respectively^{117,118}. A periodic boundary condition was employed, and van der Waals and electrostatic interactions were treated using the particle-mesh Ewald method¹¹⁹. All covalent bonds involving hydrogen atoms were constrained using the LINCS algorithm¹²⁰.

All of the MD simulations reported on here were performed at least twice with different initial seeds. Since the second and any subsequent results were all in close agreement with the first ones, for simplicity only the representative results are provided here.

4.3 Results and Discussion

We measured the VUVCD spectra of MBP from 260 to 178 nm using a VUVCD spectrophotometer in the N-state, A-state, and in the presence of PI, PIP, and PIP2 liposomes (hereinafter called PI-, PIP-, and PIP2-states, respectively). The obtained VUVCD spectra are shown in Figure 4.1. All of the VUVCD spectra were constant during the data-acquisition period (about 2 hours), indicating that the synchrotron radiation had not damaged the samples. Thus, the obtained VUVCD spectra were suitable for investigating the liposome-induced conformation of MBP.

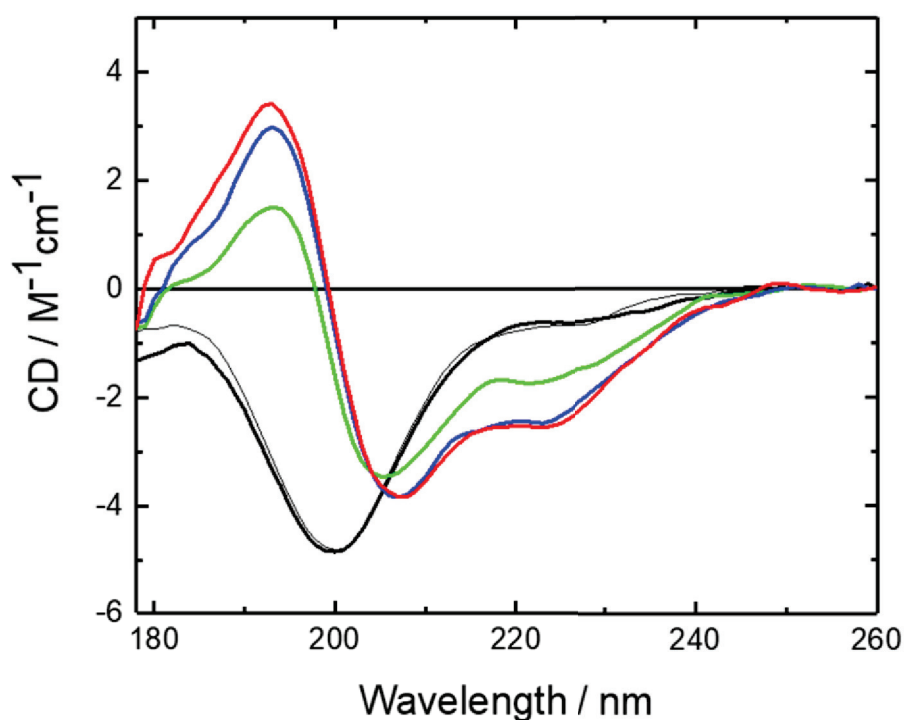


Figure 4.1. VUVCD spectra of MBP in the N- (black), A- (thin black), PI- (green), PIP- (blue), and PIP2-states (red) at 25°C.

4.3.1 Vacuum-ultraviolet circular dichroism spectra of MBP in the presence of PI liposomes

The VUVCD spectrum of MBP in the N-state exhibited a negative shoulder around 230 nm and a large negative CD peak around 200 nm (Figure 4.1), which are characteristic spectral features of unordered structures or intrinsically disordered proteins^{121,122}. The spectrum in the N-state is highly consistent with that of recombinant bovine MBP measured by Stadler et al.⁹⁵, showing that the MBP used in the present study could be compared with the results obtained in previous studies^{107,123,124}. Further, a similar spectrum was observed in the A-state, suggesting that the unordered structure in the N-state was maintained in the A-state (pH 4.5).

The spectrum of MBP in the PI-state contained two negative peaks around 208 and 222 nm and a positive peak around 193 nm, which are characteristic spectral features of α -helix-rich proteins¹²¹. The spectral change from the N- or A-state to the PI-state observed here indicates that adding the PI liposome resulted in the structure of MBP changing from a coil to a helix. The spectra of MBP in the PI-state were measured previously from 250 to 190 nm at low L/P values of 3 and 10 at pH 7.4¹⁰⁷. However, the amount of the structural alteration from coil to helix was much smaller than the result obtained in the present study, probably because of the low L/P. As shown in Figure 4.2, the spectra of MBP in the presence of DMPC and DMPS liposomes at pH 4.5 exhibited the characteristic peaks of an unordered structure and a helix structure, respectively, meaning that the net negative charge of the DMPS or PI liposome surface (the net charges of the head

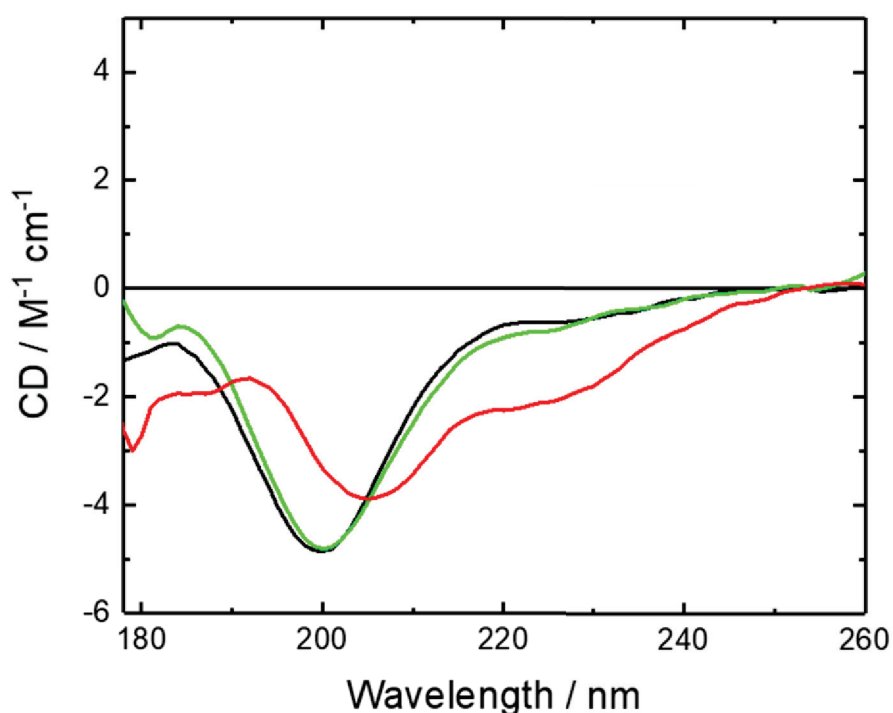


Figure 4.2. VUVCD spectra of MBP in the N- (black), DMPC- (green), and DMPS- (red) states. MBP in the N- and DMPC-states showed the same VUVCD spectra, suggesting that MBP could not interact with DMPC liposome. MBP in the DMPS-state exhibited the spectrum with small amount of helical conformation, indicating that MBP could bind to DMPS liposomes.

groups of DMPS, PI, and DMPC lipid molecules are -1 , -1 , and 0 , respectively) could induce the helix structure in MBP (Table 4.1), as mentioned in previous papers^{99,125}. In the VUVCD spectrum of MBP in the PIP-state, the CD intensities at the three characteristic peaks were greatly increased, indicating increments of the helical structure compared with that in the PI-state. This was probably due to the increase in the numbers of net negative charges on the liposome surface (-1 for PI and -2 for PIP) (Table 4.1). The spectra of bovine MBP and murine MBP in the PIP-state were measured previously at L/P values of 10 and 50 at pH 7.4, respectively^{107,126}, and showed similar spectral shapes but different intensity compared with those obtained in the present study (L/P = 300). The spectrum of MBP in the PIP2-state remained that same as that in the PIP-state despite the negative net charge increasing from -2 to -3 (Table S1). The similarity between the spectra might be related to their morphology, because Ishiyama et al.¹⁰⁷ found no significant differences in the morphology of murine MBP between the PIP- and PIP2-states in transmission electron microscopy.

As confirmed in Figure 4.1, there was an isodichroic point around 205 nm in the N-, A-, PI-, PIP-, and PIP2-states, suggesting that only two states (the N- and MB-states) were present. Further, in spite of the differences in the net charges, the spectrum in the PIP-state was consistent with that in the PIP2-state, suggesting that the conformational change in MBP induced by membrane interactions was mostly saturated in the PIP- and PIP2-states, and that the spectra of both states would be considered to reflect the membrane-bound conformation of MBP.

4.3.2 Secondary structures of the membrane-bound conformation of MBP

Table 4.2 lists the secondary-structure contents and the numbers of segments of MBP in the N-, PIP-, and PIP2-states as analyzed using the SELCON3 program. Table 4.2 indicates that MBP in the N-state comprised 5% α -helices, 26% β -strands, 22% turns, and 46% unordered structures, indicating that MBP is an intrinsically disordered protein (as mentioned above). The contents of β -strands are mostly consistent with that estimated using FTIR spectroscopy (25%)¹²⁷, although the β -strands estimated here might not exist as β -sheets, but rather as an ensemble of

Table 4.2. Secondary-structure contents and numbers of segments of MBP in the N-, PIP-, and PIP2-states determined by VUVCD spectra and the SELCON3 program. The standard errors calculated by error propagation method from experimental errors are also shown.

	α -helix		β -strand		Turn (%)	Unordered (%)
	Content (%)	Number	Content (%)	Number		
N state	5 \pm 2	3 \pm 1	26 \pm 4	11 \pm 1	22 \pm 4	46 \pm 4
PIP state	38 \pm 4	8 \pm 1	9 \pm 6	4 \pm 2	26 \pm 5	29 \pm 6
PIP2 state	39 \pm 4	8 \pm 1	8 \pm 8	4 \pm 2	25 \pm 6	30 \pm 6

numerous short peptide segments with the dihedral angles of β -strands, as are often observed in denatured proteins¹²⁸. The PIP2-state showed an increased content of α -helices (5% \rightarrow 39%) but decreased contents of β -strands (26% \rightarrow 8%) and unordered structures (46% \rightarrow 30%) (Table 4.2). Similar increases in the helix contents and decreases in the strand contents were observed in the murine MBP bound to dimyristoyl phosphatidylglycerol/DMPC (1:1) vesicles at an L/P of 300 (α -helix: 3% \rightarrow 20% and β -strands 26% \rightarrow 22%)¹²⁹. However, the helix content in our study was twice that in the previous one, probably due to the stable interaction between MBP and PIP or PIP2 membrane and the increase in the negative net charge of the membrane surface. As mentioned above, it would be expected that the spectra observed in the PIP- and PIP2-states would reflect the conformation of MBP in the MB-state. Hence, the sequences of secondary structures in the membrane-bound conformation of MBP were estimated using the VUVCD spectrum in the PIP2-state and the VUVCD-NN method.

Figure 4.3 shows the secondary-structure sequences of MBP in the PIP2-state. The positions of α -helix segments of MBP were assigned as residues 6-16, 17-24, 36-39, 85-90, 100-110, 129-140, 143-155, and 165-169, which are denoted as A-, B-, C-, D-, E-, F-, G-, and H-helices, respectively. In this method, the contents and numbers of segments of helices were 40% and 8, respectively, which are mostly consistent with the values estimated in the SELCON3 analysis (Table 4.2). The positions of secondary structures were also predicted based on the MBP sequence using the PSIPRED¹³⁰, JPred4¹³¹, and SOPMA¹³² methods (Figure 4.3). Since these three methods are only applicable to the protein structure in the N state, the

contents and numbers of segments of helices differed markedly from those obtained experimentally (e.g., the contents and numbers were 17% and 5, respectively, for PSIPRED), thereby demonstrating the advantage of the present combination method for predicting the sequence of the secondary structure of a membrane-bound protein. The membrane-bound conformation of full-length MBP at an atomic-level resolution has not been determined experimentally, but several studies have used the HELIQUEST program to tentatively assign the three amphiphilic helices of MBP (33-47, 85-94, and 144-155) as the candidate sites of membrane interactions². These three regions are depicted in Figure 4.3, in which it is evident that the C-, D-, and G-helices (i.e., residues 36-39, 85-90, and 143-155, respectively) of MBP corresponded to these three amphiphilic helices. This correspondence suggests that the VUVCD-NN method is a suitable technique for characterizing the positions of helix regions of the membrane-bound conformation of MBP. In addition to the previously reported amphiphilic helices (C-, D-, and G-helices), we have newly identified five nonamphiphilic helices (A-, B-, E-, F-, and H-helices). Hence, to confirm the capability of the eight helix segments as membrane-interaction sites, MD simulations were performed for these segments in the presence of a PI bilayer membrane.

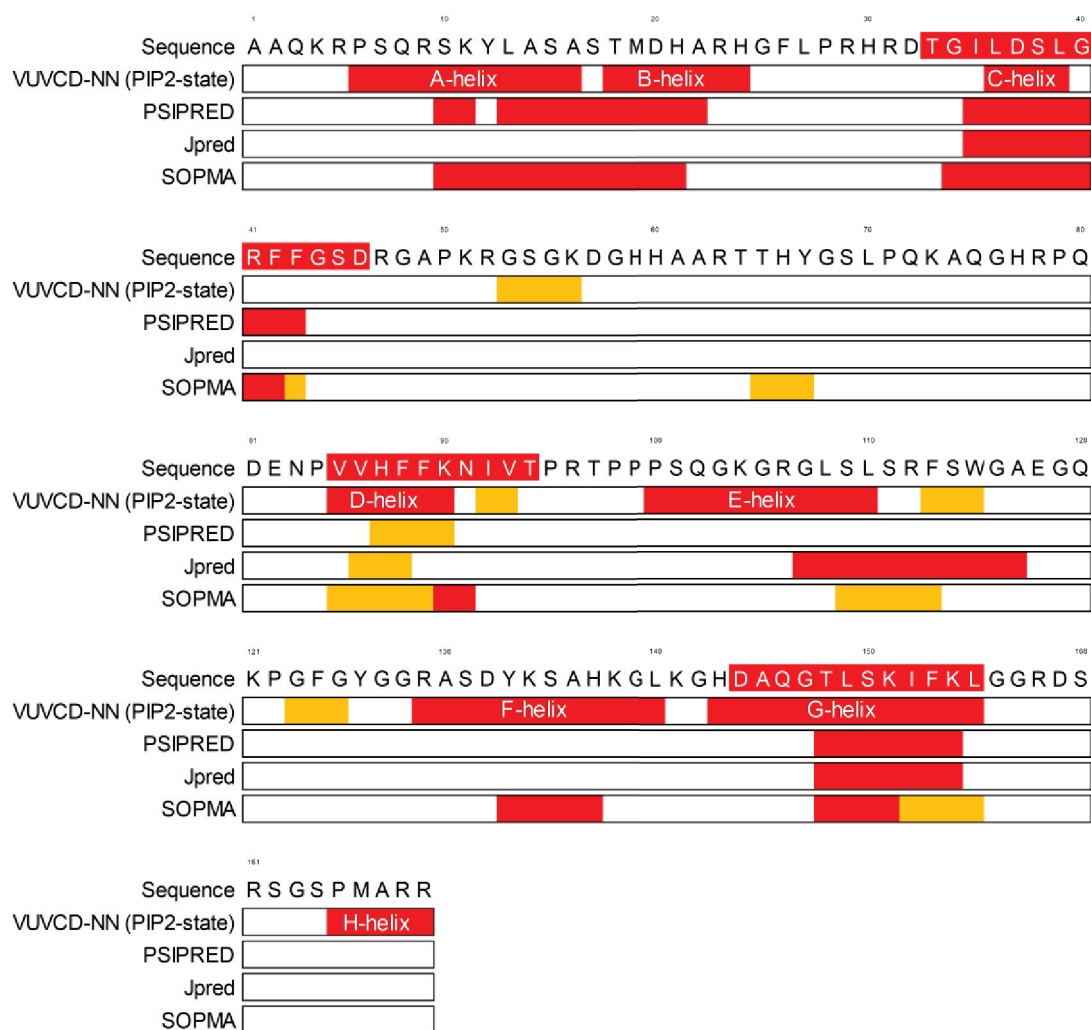


Figure 4.3. Sequence of secondary structures of MBP in the PIP2-state predicted using the VUVCD-NN method. The helix segments are denoted by upper-case letters (A- to H-helices). Sequence-based secondary structures of MBP predicted by PSIPRED, Jpred, and SOPMA are also shown. The three red regions in the sequence (residues 33-46, 85-94, and 144-155) correspond to the three membrane-interaction sites of amphiphilic helices (murine MBP) proposed by Harauz et al.²⁹ The α -helices, β -strands, and coil structures are indicated in red, yellow, and white rectangles, respectively.

4.3.3 Characterization of membrane-interaction helices of MBP using MD simulations

MD simulations are a useful technique for characterizing the conformation of membrane-bound proteins or membrane proteins, and simulations including membranes and peptide fragments assigned as membrane-interaction sites are often used to estimate the interaction mechanisms between membranes and proteins^{112,133–135}. In this study, the MD simulations in the presence of a PI bilayer membrane with a thickness of 4 nm were conducted for 250 ns for the eight peptide fragments corresponding to the A-, B-, C-, D-, E-, F-, G-, and H-helices (Figure 4.3). The PI bilayer membrane, which component lipid molecules have negatively charged head group, was stable during the 250 ns simulations, as for the case of phosphatidylglycerol lipid molecules that also have a negatively charged head group¹³⁶. The length of the peptide fragments was extended by two residues at each end, and the N- and C-terminals were acetylated and N-methylated, respectively, to enhance sampling of the insertion and conformation of peptide fragments. A helix conformation was adopted as the initial structure in the simulations^{137,138}. The peptide fragment was set to be at least 11 Å above the membrane surface (see Methods and Figure 4.4). In the simulations it was assumed that all of the eight peptide fragments could be exposed to solvent and membrane, which would be possible because MBP formed a disordered structure before interacting with the membrane.

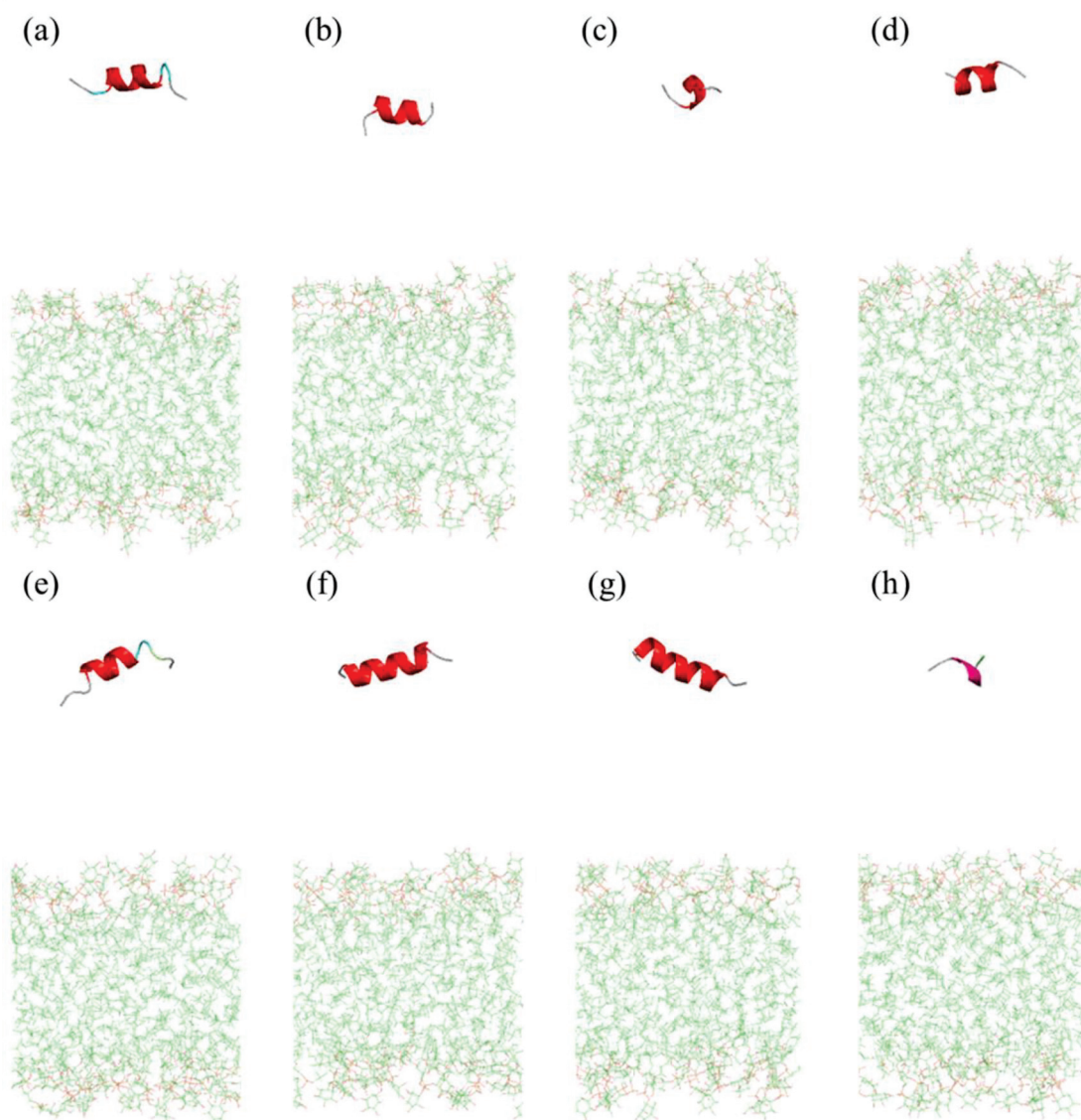


Figure 4.4. Initial structures of MD simulations after the minimization and equilibration. Panels a, b, c, d, e, f, g, and h indicate the systems of the peptide fragments corresponding to the A-, B-, C-, D-, E-, F-, G-, and H-helices in the presence of PI bilayer membrane, respectively.

Figure 4.5 plots the position-changes along the z-coordinate of the center of mass of each peptide fragment (including the side chains of amino acids) over the

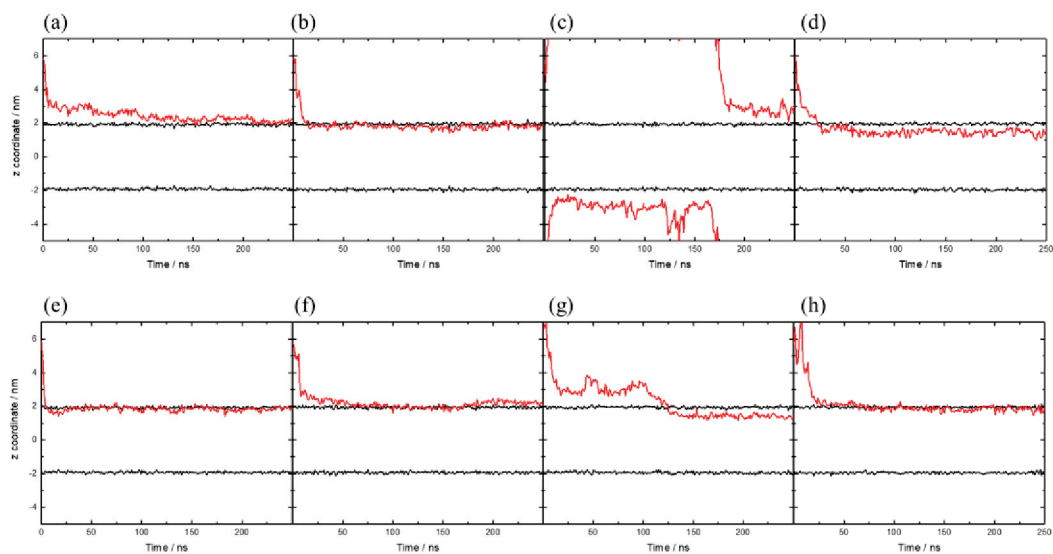


Figure 4.5. Relative position (z -coordinate) of the center of mass of eight peptide fragments against the average positions of phosphorus atoms in the lipid molecules ($z = 2$ and -2) over the 250-ns simulation period. Panels A, B, C, D, E, F, G, and H indicate the time positions of the peptide fragments (red line) corresponding to the A-, B-, C-, D-, E-, F-, G-, and H-helices, respectively. The center of mass of inositol is located around $z = 2.15$ and -2.15 (black lines). The position of $2 > z < -2$ is inside the membrane or tail region of the lipid molecules

250-ns simulation period against the average positions (around 2 and -2) of phosphorus atoms in the lipid molecules. The center of mass of inositol was located around 2.15 and -2.15 . The figure also shows that the peptide fragments corresponding to the B-, D-, E-, F-, G-, and H-helices approached the membrane surface or inositol molecule and reached the phosphate group in the membrane, whereas those corresponding to the A- and C-helices approached the membrane surface and remained there. The peptide fragments corresponding to the D- and G-helices clearly showed values of $z < 2$ at 250 ns, meaning that some of the residues of these segments deeply invaded the inside of the membrane below the position of the phosphate group. The trajectory of the peptide fragment corresponding to the C-helix differed markedly from those of the other fragments (indicated in the figure by a large jump between neighboring panels), indicating that the affinity to the membrane surface might not be particularly strong, which would be due to the shortness of the C-helix (estimated at only four residues) (Figure 4.3).

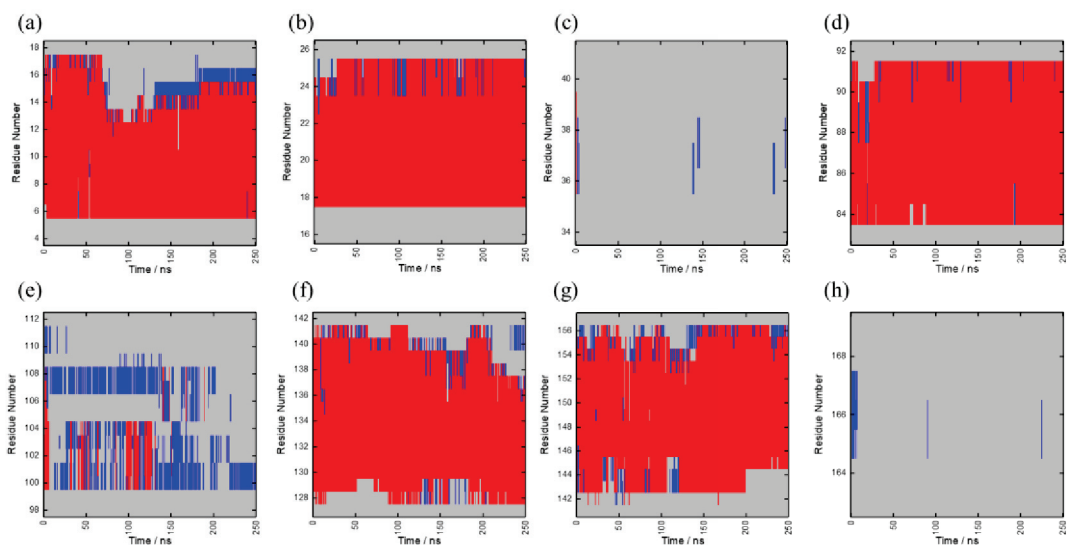


Figure 4.6. Secondary structures of each amino-acid residue in eight peptide fragments as a function of the simulation time (total of 250 ns). Panels A, B, C, D, E, F, G, and H indicate the secondary structures of the peptide fragments corresponding to the A-, B-, C-, D-, E-, F-, G-, and H-helices, respectively. Colors: gray, coil; blue, turn; red, α -helix.

The time-dependent secondary structures of each peptide fragment during each simulation are also depicted in Figure 4.6. It is evident that the peptide fragments corresponding to the A-, B-, D-, F-, and G-helices formed a helix structure on the membrane surface while the others were distorted, although the E-helix region with a proline-rich region changed into a turn structure during the simulations (Figure 4.6). These simulations suggest that all of the peptide segments can approach and interact with the membrane surface within 250 ns, but only the peptide fragments of the A-, B-, D-, F-, and G-helices remain as helix structures on the surface. Control simulations of the eight peptide fragments were conducted without the membrane, which revealed that all of the peptide fragments transformed into unordered structures within 300 ns (Figure 4.7). This means that the A-, B-, D-, F-, and G-helical structures can be stabilized in the presence of a PI bilayer.

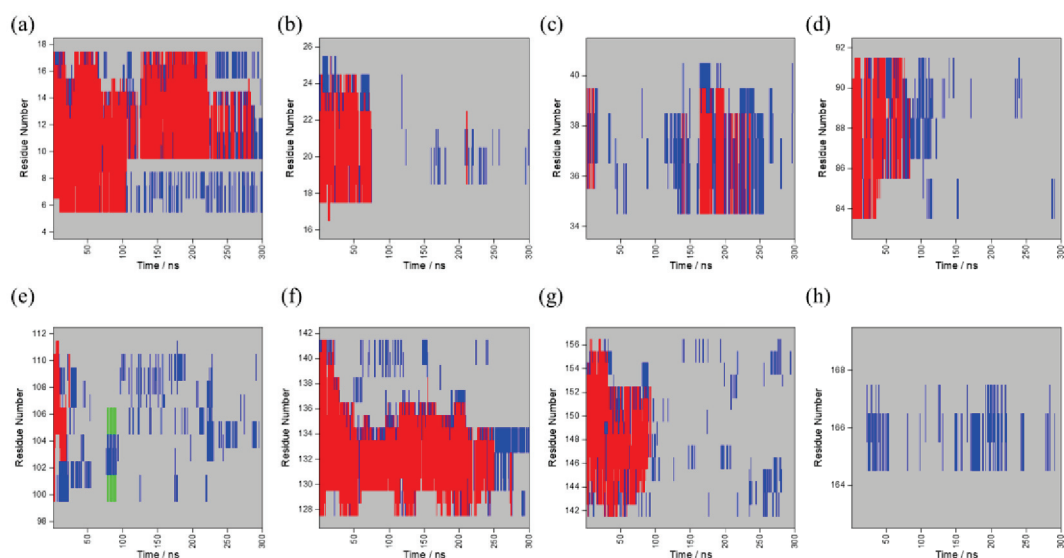


Figure 4.7. Secondary structures of each amino-acid residue in eight peptide fragments as a function of the simulation time (total of 300 ns) in the absence of a PI bilayer membrane. Panels a, b, c, d, e, f, g, and h indicate the secondary structures of the peptide fragments corresponding to the A-, B-, C-, D-, E-, F-, G-, and H-helices, respectively. The simulation system for the peptide fragments of MBP in the absence of a PI bilayer membrane was generated using the CHARMM-GUI interface. The system including peptide and solvents was minimized using a steepest-descent algorithm, followed by a “suggested” equilibration steps. The production steps were carried out for 300 ns with a 2-fs time step using the GROMACS package and the CHARMM36m force field. The simulations were performed using the NPT ensemble, in which temperature (25 °C) and pressure (1 bar) were maintained using a Nose-Hoover thermostat and Langevin barostat, respectively. A periodic boundary condition was employed, and van der Waals and electrostatic interactions were treated using the particle–mesh Ewald method. All covalent bonds involving hydrogen atoms were constrained using the LINCS algorithm. Colors: gray, coil; blue, turn; red, α -helix; green, β -strand.

4.3.4 Membrane-bound conformation of MBP

While the membrane-bound conformation of full length MBP remains unclear, the basic conformation could be represented schematically as three membrane-bound amphiphilic helix segments and the proline-rich turn segment, showing that the sequence of secondary-structure segments is two successive helices, a turn, and a helix^{137,138}. The combined analysis method of VUVCD and MD utilized in the present study suggested that the A-, B-, D-, F-, and G-helix regions are the membrane-interaction sites, with the D- and G-helix regions corresponding to two of the three membrane-bound amphiphilic helices. The C-helix region probably formed a distorted structure during the simulation due to its shortness, but the region and its surroundings were strongly expected to form a helix structure, as reported previously². Therefore, the sequence of the secondary-structure segments of the membrane-bound conformation of MBP obtained in the present study would be four successive helices (A-, B-, C-, and D-helices), a turn, and two successive helices (F- and G-helices); the order of these secondary-structure segments is essentially consistent with the previous representation of two successive helices, a turn, and a helix^{137,138}.

As shown in Figure 4.5, the D- and G-helix regions deeply invaded the inside of the membrane, whereas the A-, B-, and F-helix regions (or nonamphiphilic helices) remained around the membrane surface or the lipid phosphate group at 250 ns. To evaluate the degree of insertion of each helix segment into the membrane, the average positions of the amino-acid residues in the peptide fragments corresponding to the A-, B-, D-, F-, and G-helices from 200 to 250 ns are plotted in Figure 4.8 against the phosphorus atoms in the lipid molecules (around zero). For the peptide fragment corresponding to the D-helix region (Figure 4.8C), it is evident that V85, F88, and F89 were located inside the membrane, where they can interact hydrophobically with the tail region of the lipid molecules, while K90 was near the membrane surface and can interact electrostatically with the phosphate group (Figure 4.9D). Further, in the G-helix region (Figure 4.8E), K151 and K154 were located around the phosphate group and can interact electrostatically, and L149 and F153 were inside the membrane, in which both residues can interact hydrophobically (Figure 4.9G). The patterns of interactions of these amino-acid residues are highly consistent with previous reported experimental and theoretical findings for murine MBP^{125,137,138}. On the

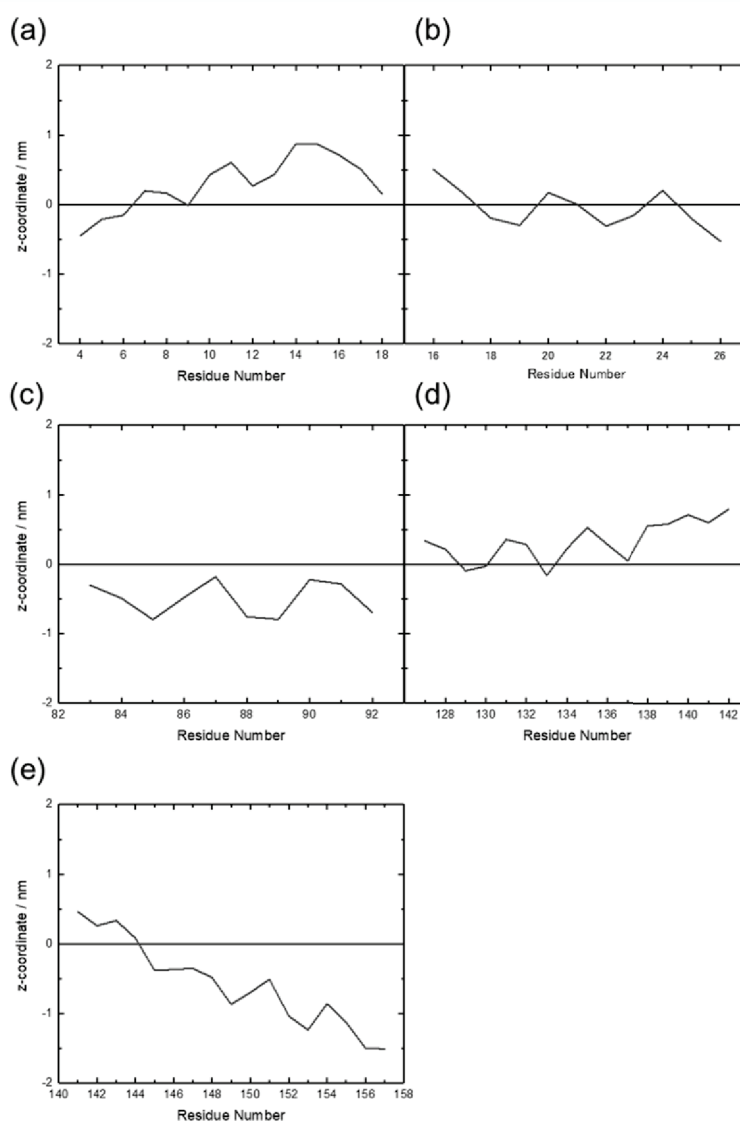


Figure 4.8. Average positions (z-coordinate) of each amino-acid residue of the A-, B-, D-, F-, and G-helix regions (panels A, B, C, D, and E, respectively) between 200 and 250 ns. The average position of the phosphorus atoms in the lipid molecules was recentered to $z = 0$, and the position of $z < 0$ is inside the membrane or tail region of the lipid molecules

other hand, the positively charged residues of R9 (A-helix), R23 (B-helix), and R129 and K134 (F-helix) are located around the negatively charged phosphate group in the membrane (Figure 4.8), implying that the A-, B-, and F-helix regions (or nonamphiphilic helices) would interact with the membrane via electrostatic interactions (Figure 4.9A, B, F).

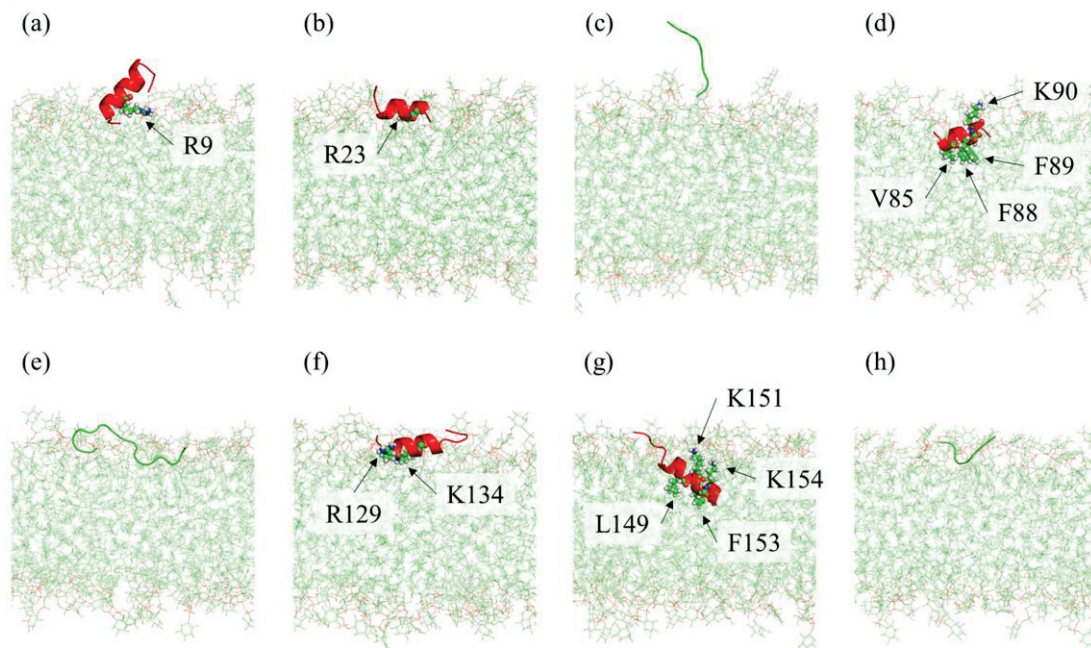


Figure 4.9. Snapshots of the MD simulations at 250 ns. Panels a, b, c, d, e, f, g, and h indicate the systems of the peptide fragments corresponding to the A-, B-, C-, D-, E-, F-, G-, and H-helices in the presence of PI bilayer membrane, respectively.

Considering these insights into the types of interactions between each amino-acid residue and the membrane, a plausible model structure for the membrane-bound conformation of MBP could be constructed based on a previous schematic representation^{137,138}. In this model, the A-, B-, C-, and D-helix regions and the F- and G-helix regions interact with the upper surface of one membrane and the lower surface of another membrane, respectively, and the E-helix region connects the two helix regions as a turn structure to make the membrane both compact and stable. However, the A-, B-, and F-helix regions would interact electrostatically with the membrane surface as nonamphiphilic helices, while the D- and G-helix regions (and probably also the C-helix region) would interact both hydrophobically and electrostatically with the membrane as the amphiphilic helices. Although further experimental and theoretical data are needed for refining the membrane-bound conformation and membrane-interaction sites of MBP, these results suggest that MBP can interact with the PI membrane via amphiphilic and nonamphiphilic

helices under the control of a delicate balance between electrostatic and hydrophobic interactions.

In summary, we have characterized the conformation of full-length MBP in PI membranes by using VUVCD spectroscopy and MD simulations and found that two amphiphilic and three nonamphiphilic helices interact with the membrane surface via hydrophobic and electrostatic interactions, suggesting that these helices contribute to the formation and stabilization of the stacking structure of myelin sheath.

Chapter 5: Circular dichroism, linear dichroism, and fluorescence studies of the interaction between antimicrobial peptide magainin 2 and lipid membrane

5.1 Introduction

Antimicrobial resistance (AMR) is one of the most serious global threats to healthcare and agriculture. The overuse and misuse of antimicrobial agents, such as antibiotics, can lead to the emergence of antimicrobial-resistant microorganisms, resulting in prolonged hospitalizations and increased medical costs¹³⁹. AMPs are a potential solution to this problem because they have broad-spectrum antibacterial, antifungal, and antiviral activities and it is difficult for microorganisms to acquire AMR against them^{3,140}. The antimicrobial mechanism of AMP is different from that of conventional antibiotics; antibiotics inhibit the synthesis of bacterial components, whereas AMPs interact with bacterial cell membranes and directly cause damage to the membrane structure^{3,31}. Extensive efforts have been devoted to utilizing AMP as a medicine; however, the clinical application of AMP is currently limited due to its short half-life and toxic side effects^{141–143}. Hence, further understanding of the interaction mechanism between AMP and membranes at the molecular level are necessary to gain new insights into the design strategy of effective AMP¹⁴⁴.

M2, a cationic and amphipathic peptide composed of 23 amino acids (GIGKFLHSAKKFGKAFVGEIMNS), is an AMP present in the immune system of African clawed frog *Xenopus laevis*¹⁴⁵. The interactions between M2 and the membrane have been investigated extensively through various biophysical techniques such as fluorescence spectroscopy, CD spectroscopy, NMR

spectroscopy, and isothermal titration calorimetry (ITC)^{51,146–148}. Regarding the molecular mechanism of the antimicrobial activity of M2, Matsuzaki et al. suggested that the M2 peptides assembled and transformed the oligomers in PG membranes, and their oligomerization induced pore formation in the membrane, leading to membrane disruption by M2^{149,150}. Schümann et al.¹⁵¹ and Gregory et al.¹⁵² found that no peptide oligomerization occurs when M2 interacts with 1-palmitoyl-2-oleoylphosphatidylglycerol phospholipids (POPG) membranes and with the mixed membranes of 1-palmitoyl-2-oleoylphosphatidylcholine (POPC) and POPG, suggesting that in a peptide state (no oligomerization), M2 works in a chaotic or stochastic manner on the pores on these membranes when obtaining the antimicrobial activity¹⁵³. These results indicate that the mechanisms of the membrane interaction or the antimicrobial activity of M2 might strongly depend on the constituents of the lipid membrane¹⁵⁴. Although these studies commonly support that M2 peptides tightly interact with negatively charged lipid membranes, such as PG, compared to neutral lipid membranes, these interactions remain to be further explored^{51,149}. As for the conformation of the M2 peptide on the membrane, most reports concluded that the membrane-bound conformation of M2 was an α -helix-rich structure, but some groups, including Hirsh et al. showed that there are two populations of M2 peptides in the membranes of dipalmitoylphosphatidylglycerol (DPPG) and in the mixed membranes of DPPG and dipalmitoylphosphatidylcholine (DPPC); with one population being completely α -helical and another being completely β -strand^{155–157}, as observed in other AMPs, such as bovine lactoferricin, protegrin 1, and human β -defensin-3¹⁵⁸. These results suggest that M2 could also form both α -helix and β -strand structures on the membrane, although the contribution of these M2 conformations to the antimicrobial activity is unclear and still controversial.

In this study, we characterized the unique and complicated conformations of M2 peptides on the negatively charged DPPG membrane and their contributions to the antimicrobial activity. We measured the VUVCD and LD spectra of M2 in the DPPG liposome in the L/P molar ratio from 0 to 26 and analyzed the types of secondary structures (α -helix and β -strand) of M2 and their orientation on the membrane. VUVCD has been applied to characterize the secondary structures of membrane-bound proteins in various liposomes^{14,108,159} and can measure the CD spectra down to the vacuum-ultraviolet region (~ 160 nm), whose wide range spectra could realize the component analyses of the unique and complicated conformations of M2 induced by the interaction with the DPPG membrane. LD

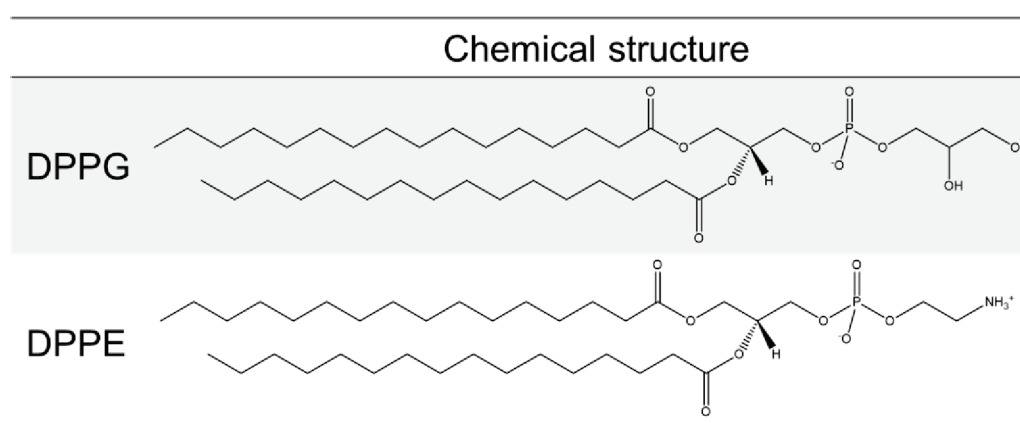
spectroscopy can provide important information on the secondary structure orientation, disclosing the direction of the helical and strand axes of M2 against the liposome surface¹⁴. Furthermore, the fluorescence anisotropy of DPPG liposomes in the presence of M2 was measured to elucidate the effect of M2-membrane binding on the structure and stability of lipid membranes. The combination of VUVCD, LD, and fluorescence spectroscopy could be useful for characterizing the relationships between the unique conformations and activities of M2 on the DPPG membrane.

5.2 Experimental

Materials

The M2 peptide was synthesized in GL Biochem (Shanghai, China), GenScript Biotech Corporation (Piscataway, NJ), and Bio-Synthesis (Lewisville, TX, USA). This peptide was purified by HPLC (>95%) and its molecular weight was analyzed by mass spectroscopy. DPPG (sodium salt) was purchased from Avanti (Alabaster, AL). 1, 2-dipalmitoyl-sn-glycero-3-phosphatidylethanolamine (DPPE) was obtained from Cayman Chemical (Ann Arbor, MI, USA). The chemical structures are shown in Table 5.1. All other chemicals were analytical grade products purchased from Sigma. DPPG lipid molecule was dissolved in 10 mM phosphate buffer (pH 7.0) and the DPPG liposomes with a diameter of 100 nm were prepared by an extrusion technique. The obtained liposome vesicles were mixed with the

Table 5.1. Chemical structures of phospholipids used in this study.



M2 solution at a final M2 concentration of 300 μM . The concentration of M2 was determined by measuring the absorption spectra of M2 in the absence of liposomes (molar extinction coefficient at 205 nm: 94,390 $\text{M}^{-1} \text{cm}^{-1}$). The concentration of DPPG phospholipid was changed from 0 to 8 mM (i.e., the L/P molar ratio of 0–26). The peptide-liposome mixtures were incubated overnight at 25 °C prior to the CD and LD measurements. For fluorescence anisotropy measurements, the following steps were performed before dissolving the lipids in the buffer: DPPG and DPH were dissolved in chloroform, and the stock solutions were then mixed at a DPPG/DPH molar ratio of 400/1. To remove the organic solvent, the solution was placed under a stream of nitrogen gas and then under vacuum for at least three hours¹⁴. The obtained DPPG film was dissolved in the buffer at final concentrations of 400 μM and 1 μM of DPPG and DPH, respectively.

VUVCD measurements

The SRCD spectra of M2 in the presence and absence of DPPG liposomes were recorded from 260 to 178 nm using a VUVCD spectrophotometer at HiSOR and an assembled optical cell with a 50 μm path length Teflon spacer. The distance between the optical cell and the window of the photomultiplier tube was set to less than 10 mm to minimize the effect of light scattering from the liposome particles¹⁴. The temperature of the cell was controlled using a Peltier device. The actual temperature of the sample solution was obtained by a calibration curve of the actual temperature (in the optical cell) against the set temperature, which was investigated in advance. The SRCD spectra of each sample were measured four times and averaged. The SRCD spectra of the liposome solutions were also measured as a background and subtracted from the spectra of the peptide-liposome suspensions. The secondary structures of M2 in the presence and absence of DPPG liposomes were analyzed using the SELCON3 program^{67,68} and the VUVCD dataset obtained by Matsuo et al.^{15,16}, as described previously^{14–16}.

LD measurements

The LD spectra of M2 in the presence of liposomes were measured from 300 to 185 nm using an LD spectrometer installed in the VUVCD spectrophotometer at HiSOR. An LD flow cell with a light path length of 75 μm (Translume, MI) was located within 10 mm of the photomultiplier tube. A shear flow with a flow velocity of 1.0 mL min^{-1} was applied using a dual-plunger parallel-flow pump (LC-20AD, Shimadzu, Japan), and the sample solution was circulated between the

sample container and the LD flow cell. All LD spectra were recorded at room temperature (25 °C) with four accumulations. The scattering contribution to the LD signal was subtracted using the method described by Nordh et al. ¹⁶⁰.

LD spectrum of M2 in DPPG liposomes at L/P = 25 was analyzed using the absorption spectrum. The absorption spectrum of M2 in DPPG liposomes at L/P = 25 was obtained by using the VUVCD spectrophotometer and the equation, $\log(HT_{pm}/HT_{pr}) - \log(HT_{lm}/HT_{lr})$, in which HT_{pm} and HT_{pr} are high tension voltages of the sample of M2 peptides in DPPG liposomes detected on main photomultiplier (main-PM) and reference photomultiplier (ref-PM), respectively, and HT_{lm} and HT_{lr} are high tension voltages of DPPG liposome sample detected on main-PM and ref-PM, respectively. The absorption spectrum was deconvoluted into three gaussian-type contributions with peaks at 190 nm, 208 nm, and 222 nm. Angle dependence of theoretical LD spectra were calculated by using the equation, $A_{LD} = 3/2 S \sum_{n=1}^3 A_{iso}(\lambda_n) (3\cos^2\gamma(\lambda_n)-1)$, where S is the orientation parameter, A_{iso} is the isotropic absorption spectrum obtained from the absorption spectrum, γ is the angle between the flow and the transition moment directions, and λ_n is the peak wavelength for n th contribution. For an ideal system, S is equal to 1, meaning that the molecules in the system are completely oriented. The dipoles at 190 nm, 208 nm, and 222 nm of helical peptides are vertical, parallel, and vertical to the helix axis, respectively. The limiting case for a biased alignment behavior is when the elliptical liposome is modeled as an infinite tube, the helical peptides are on the surface of the tube, and the peptides are aligned at an angle α between the helical axis and the normal of the tube surface. In this extreme condition, the γ for LD signals at 190 nm, 208 nm, and 222 nm are 90°, 0°, and 90°, respectively, when the helical peptides are lying parallel to the tube ($\alpha=90^\circ$). On the other hand, the γ for LD signals at 190 nm, 208 nm, and 222 nm are 0°, 90°, and 0°, respectively, when the helical peptides are inserted perpendicular to the tube ($\alpha=0^\circ$) [Transmembrane]: [On surface] ratio dependence of the theoretical LD spectra were calculated based on the assumption that M2 is in equilibrium between two helix states: transmembrane M2 and M2 on the membrane surface.

Fluorescence anisotropy measurements

The steady-state fluorescence anisotropy for DPH in DPPG liposome was measured using fluorescence spectrophotometer (FP-8300, Jasco, Japan). The excitation and emission wavelengths were 357 and 430 nm, respectively, with 5.0 nm band width. The measurements were conducted in the temperature range from

25 to 55 °C with 0.1 °C steps. The curves of temperature dependence of the anisotropy were fitted using the equation,

$$r(T) = r_l + m_l(T - T_l) + \frac{r_g - r_l + m_g(T - T_g) - m_l(T - T_l)}{1 + \exp\left(-\frac{\Delta H}{RT}\left(1 - \frac{T}{T_m}\right)\right)}, \quad (5.1)$$

where T is the absolute temperature, T_l and T_g are the reference temperatures for DPPG liposome in liquid-crystalline phase (= 55°C) and gel phase (= 25°C), respectively, r_l and r_g are the values of fluorescence anisotropy at 55°C (liquid-crystalline phase) and 25 °C (gel phase), respectively, T_m is the midpoint temperature of the phase transition of DPPG membrane, ΔH is the molar enthalpy change of the phase transition at T_m , and R is the gas constant. m_l and m_g in Equation (5.1) are temperature dependences of fluorescence anisotropy of lipid vesicles in liquid-crystalline phase and gel phase, respectively, which are empirical parameters. The adjustable parameters in Equation (5.1) are ΔH , T_m , m_l , and m_g .

Calcein leakage assay

M2-induced leakage of calcein entrapped in DPPG liposome was investigated at 25°C as described in section 2.6. The fluorescence intensity of calcein was monitored at 515 nm using a fluorescence spectrometer (FP-8300, Jasco, Japan) with an excitation wavelength of 490 nm. The extent F of calcein release was calculated according to $F = (I_f - I_0) / (I_{\max} - I_0)$, in which I_0 and I_f are the initial and final (about 40 min after the initial manipulation) intensities of fluorescence, respectively, and I_{\max} is the maximal fluorescence intensity obtained by adding Triton X-100 (all the entrapped calcein was released). Calcein-loaded DPPG liposomes were prepared by the extrusion method under the solution condition of containing 60 mM calcein and 10 mM HEPES (pH 7.0). Un-trapped calcein was separated from the liposomes by gel filtration using a bio-spin chromatography column (BIO-RAD, CA) with Sephadex G-75. This step was performed above the lipid phase transition temperature. Calcein was purchased from Tokyo Chemical Industry. The lipid concentration (= 400 μ M) was determined by a phosphorus assay¹⁶¹.

Adsorption model fitting procedure

The L/P dependence of the SRCD spectra of M2 in DPPG liposomes was analyzed using an adsorption model and a global fitting algorithm. The model of adsorption for a large self-associating ligand based on scaled particle theory was used as the model for fitting in this study¹⁶². The model can be written as¹⁶²:

$$Kc_f = \Phi_1\gamma_1(\Phi_1, \Phi_z), \quad (5.2)$$

$$\Phi_z = zK_{1z} \frac{(\gamma_1(\Phi_1, \Phi_z))^z}{\gamma_z(\Phi_1, \Phi_z)} \Phi_1^z, \quad (5.3)$$

$$\ln \gamma_1 = -\ln(1 - \Phi_1 - \Phi_z) + \frac{3\Phi_1 + \left(\frac{2}{f} + \frac{1}{f^2}\right)\Phi_z}{1 - \Phi_1 - \Phi_z} + \left(\frac{\Phi_1 + \frac{1}{f}\Phi_z}{1 - \Phi_1 - \Phi_z}\right)^2, \quad (5.4)$$

$$\ln \gamma_z = -\ln(1 - \Phi_1 - \Phi_z) + \frac{3\Phi_z + (2f + f^2)\Phi_1}{1 - \Phi_1 - \Phi_z} + \left(\frac{\Phi_z + f\Phi_1}{1 - \Phi_1 - \Phi_z}\right)^2, \quad (5.5)$$

where K is the association constant; c_f is the concentration of the peptide free in solution (or N state); $\Phi_1 (=nc_1/c_L)$ and $\Phi_z (=nc_z/c_L)$ are the fractions of the surface area occupied by the monomer and z-mer, respectively; c_1 and c_z are the concentrations of monomer and z-mer, respectively; c_L is the total lipid concentration; n is the number of lipid molecules covered by a single peptide; K_{1z} is the equilibrium constant for the formation of the z-mer; and f is the ratio of the radii of the circles representing the monomer and z-mer. When the area does not change due to self-association, f is equal to $z^{1/2}$.

To fit the adsorption model to the SRCD data, the thermodynamic parameters K , K_{1z} , z , and n were solved numerically using an iterative method. Their initial values were set, c_f , c_1 , and c_z at each L/P were calculated according to Equations (5.2)–(5.5), and then the concentration matrix C was output. The matrix of the pure component spectra S for M2 in native, monomeric, and oligomeric states was calculated using Equation (2.8) and the matrix D of measured SRCD data. The 2-norm of the error $E = |CS-D|_2$ was minimized by repeating the calculation with different initial values of K , K_{1z} , z , and n . The obtained solutions for the parameters were then used to calculate the fractions of M2 in the three states at each L/P using the least-squares method⁴²:

$$C = D(S^T(SS^T)^{-1}). \quad (5.6)$$

The populations of M2 in the three states at each L/P obtained using Eq. (5.6) were compared with the fitting curves calculated using the optimized thermodynamic parameters. The optimized component spectra of M2 in the three states were calculated using Equation (2.8) with the optimized parameters.

5.3 Results

5.3.1. Vacuum-ultraviolet circular dichroism

The VUVCD spectra of M2 in the presence of DPPG liposomes (pH 7.0 and 25 °C) were measured from 260 to 178 nm in the L/P ratios from 0 to 26, as shown in Figure 5.1. The spectrum at L/P = 0 exhibited a negative shoulder around 220

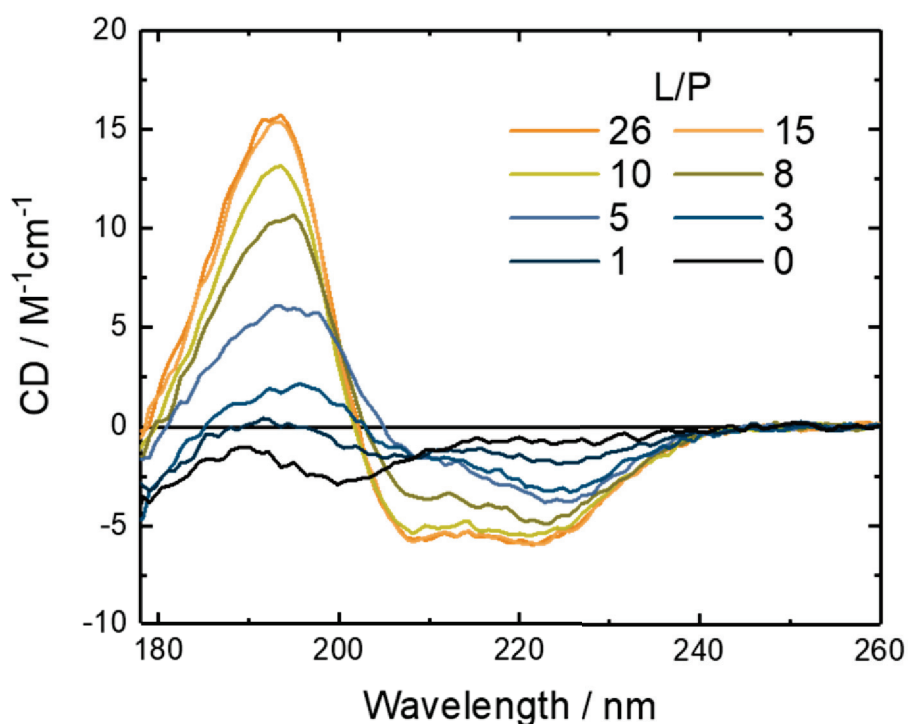


Figure 5.1. VUVCD spectra of M2 in the presence of DPPG liposome in the L/P ratio from 0 to 26. All spectra were recorded at 25 °C, pH 7.0, and the M2 concentration of 300 μ M.

nm, a negative peak around 200 nm, and a negative sign around 178 nm, indicating that M2 formed a random coil structure in the N state. As the L/P ratio increased, the spectral intensities of the shoulder and peak observed in the N state decreased and increased, respectively. The spectral change was completely saturated around L/P = 15, and the spectrum at L/P = 26 had two successive negative peaks around 222 and 208 nm and a positive peak around 190 nm, indicating that M2 formed a helical structure in the MB state. Furthermore, we found two iso-dichroic points around 200 and 210 nm during the spectral change, implying that M2 formed a helical conformation in the DPPG membranes through an intermediate state. M2 in the mixed liposomes with a DPPE/DPPG molar ratio of 3/1, which is believed to mimic the cell membranes of bacteria^{163,164}, also exhibited the same spectral change at 25 °C as those of M2 in DPPG liposomes (Figure 5.2), suggesting that M2 also has an intermediate state when interacting with the bacterial cell membrane.

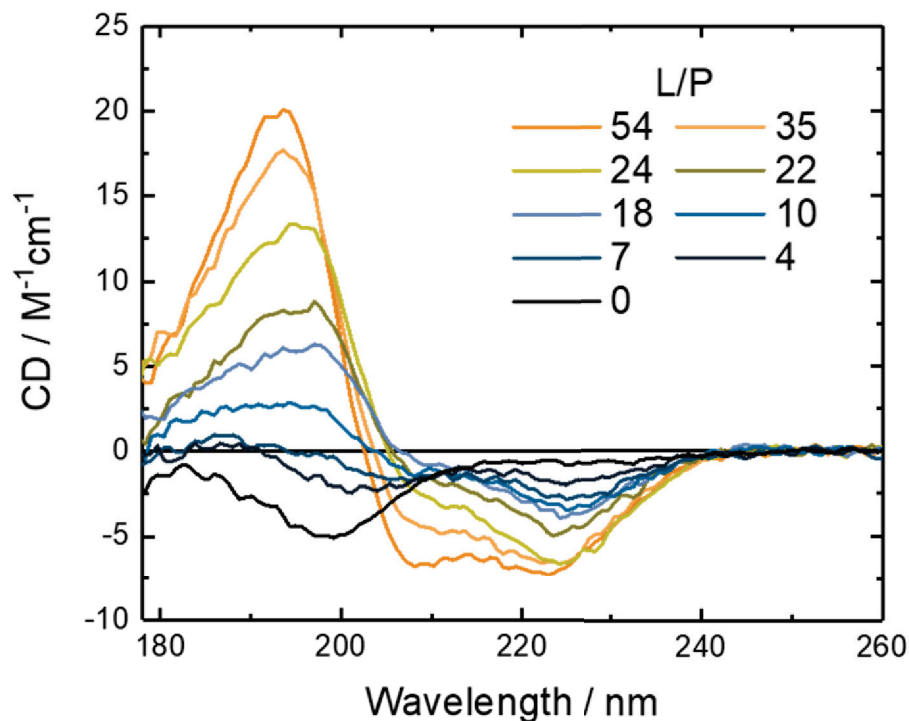


Figure 5.2. VUVCD spectra of M2 in the presence of DPPE/DPPG (molar ratio: 3/1) liposome at the L/P from 0 to 54 at 25 °C

We analyzed the spectral dataset in Figure 5.1 using the singular value decomposition (SVD) method. SVD, which is closely related to a principal component analysis, is a useful method for determining the dimension of a data matrix or the number of component spectra in the dataset^{165,166}. As a result, the SVD analysis provided three singular values that were significantly larger than zero and estimated three component spectra that can construct the VUVCD dataset within experimental error (Figure 5.3 and Figure 5.4). This indicates that the VUVCD spectra over the entire range of the L/P ratio can be explained by only three components, meaning that the spectral set in Figure 5.1 can be explained by

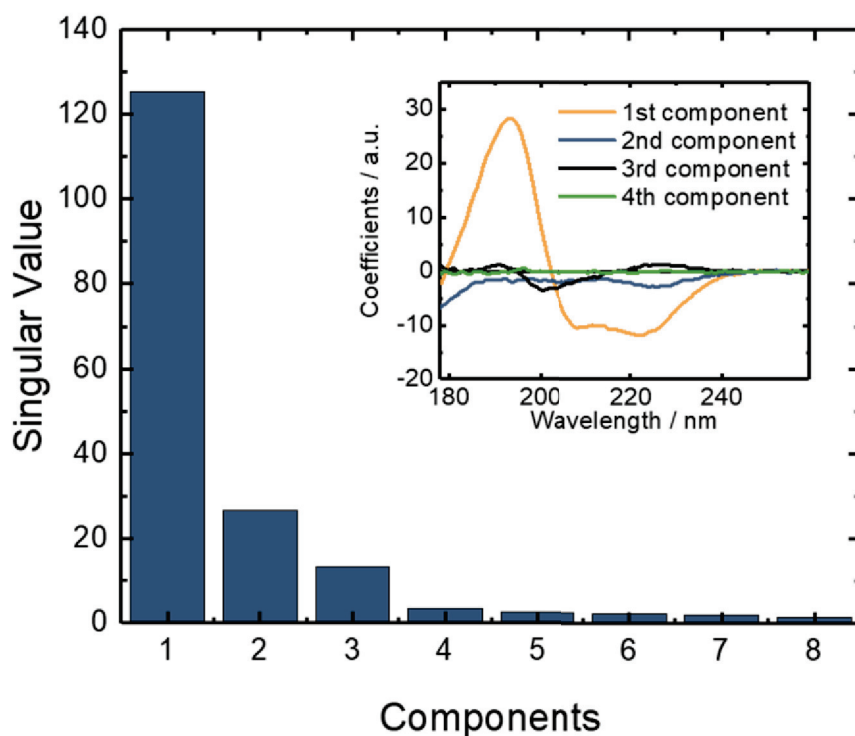


Figure 5.3. The singular values from the SVD analysis of the VUVCD spectra of M2 in DPPG liposomes at 25 °C. In SVD, the data matrix D is decomposed into three matrices as, $D = USV^T$, where U and V are the orthogonal matrices, and S is the diagonal matrix which contains the non-negative singular values on its diagonal. The inset shows the first four rows of US from the SVD analysis. The results showed that only three singular values were significantly larger than zero.

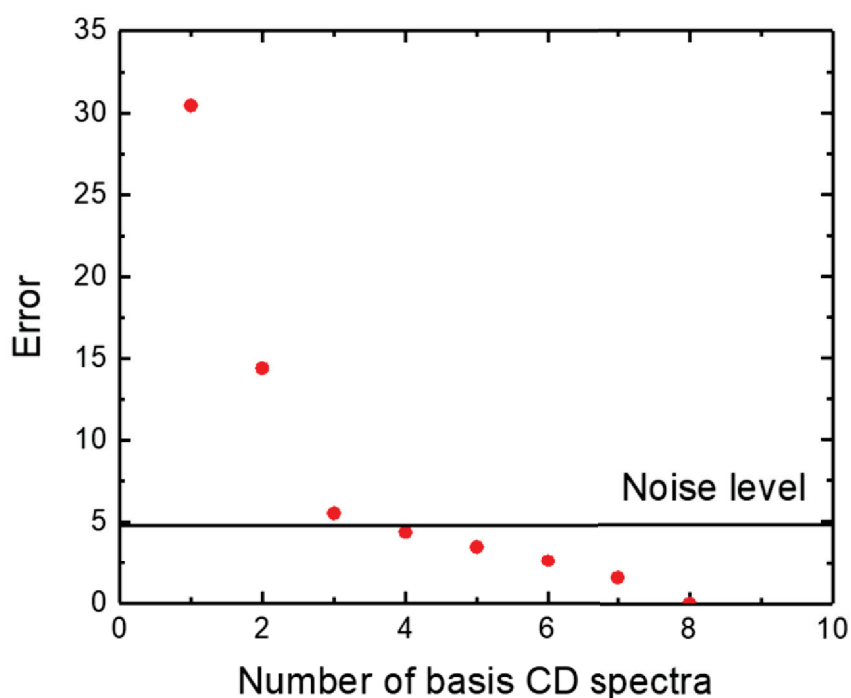


Figure 5.4. Error in reproducing VUVCD data set of M2 in DPPG liposomes using basis CD spectra from SVD analysis. The 2-norm of the error E was calculated by $E = \|D - U\tilde{S}V^T\|_2$, where \tilde{S} is the diagonal matrix which contains a part of the singular values obtained from the SVD analysis on its diagonal. Experimental noise level derived from data accumulation was also shown. The noise E_{exp} was calculated by $E_{\text{exp}} = \sqrt{\sum_{k=1}^l \sum_{j=1}^N \frac{1}{n-1} \sum_{i=1}^n (\Delta\varepsilon_{ijk} - \overline{\Delta\varepsilon}_{ijk})^2}$, where $\Delta\varepsilon$ is the CD value, $\overline{\Delta\varepsilon}$ is the average CD value, n is the number of data accumulation, N is the number of digitized wavelength points in each spectrum, and l is the number of L/P data points. The results showed that the error calculated using three basis CD spectra was almost equivalent to the experimental noise level.

the three-state model. However, the component spectra obtained from SVD might not correspond to that of M2 in each independent state (native, intermediate, and MB states) because the spectrum of M2, even in the N state, is composed of the

components of secondary structures¹⁶⁶. Hence, further analyses were conducted as follows:

Several physical models can explain the adsorption of peptides on membrane surfaces^{79,162,167}. Among them, the adsorption model with a large self-associating ligand based on scaled particle theory successfully explained the sigmoidal shape of the adsorption isotherm of lysozyme (or ligand) on negatively charged membrane surfaces, showing that the lysozyme gathered upon the membrane association⁷⁹. The sigmoidal shape of the adsorption isotherm is also a key behavior for interpreting the interaction between M2 and negatively charged PG because the same sigmoidal curve was observed in the tryptophan fluorescence experiments for M2 analogs and PG liposomes¹⁴⁹. Hence, to characterize the intermediate state of M2, we analyzed the VUVCD spectral data (Figure 5.1) using the adsorption model and the global fitting simulation (fitting procedures are provided in the Experimental section). This model assumes that peptides are in equilibrium between only three states: the N state in aqueous solution, the membrane-bound monomeric state, and the membrane-bound z-meric (oligomeric) state.

Figure 5.5 (a) shows the L/P dependence of the fractional populations of M2 in the native, membrane-bound monomeric, and oligomeric states. The inset of Figure 5.5 (a) shows the plots and fitting curve of CD at 193 nm against L/P. These experimental data were reproduced well from the adsorption model with a large self-associating ligand. We also found that the fitting error obtained using the adsorption model ($E = 9.5$) was much smaller than that obtained using the simplest monomodal adsorption model⁷⁹ ($E = 16.5$), which also supports the presence of the intermediate state. To understand the conformation of M2 in the intermediate state, we computed the spectra of M2 in the three states, as shown in Figure 5.5 (b). Native M2 exhibited a negative CD peak at 200 nm, which is a characteristic peak of the random coil structure¹²¹, whereas M2 in the membrane-bound monomeric state showed two negative peaks at 208 and 222 nm, and a positive peak around 193 nm, which are characteristic of the α -helix structure¹²¹. Moreover, M2 in the oligomeric state exhibited a negative peak around 225 nm, and a positive peak at 200 nm, which are characteristic peaks of the β -strand structure¹²¹, indicating that the α -helix monomers of M2 in DPPG membranes self-associate and transform to β -strand oligomers in the intermediate state.

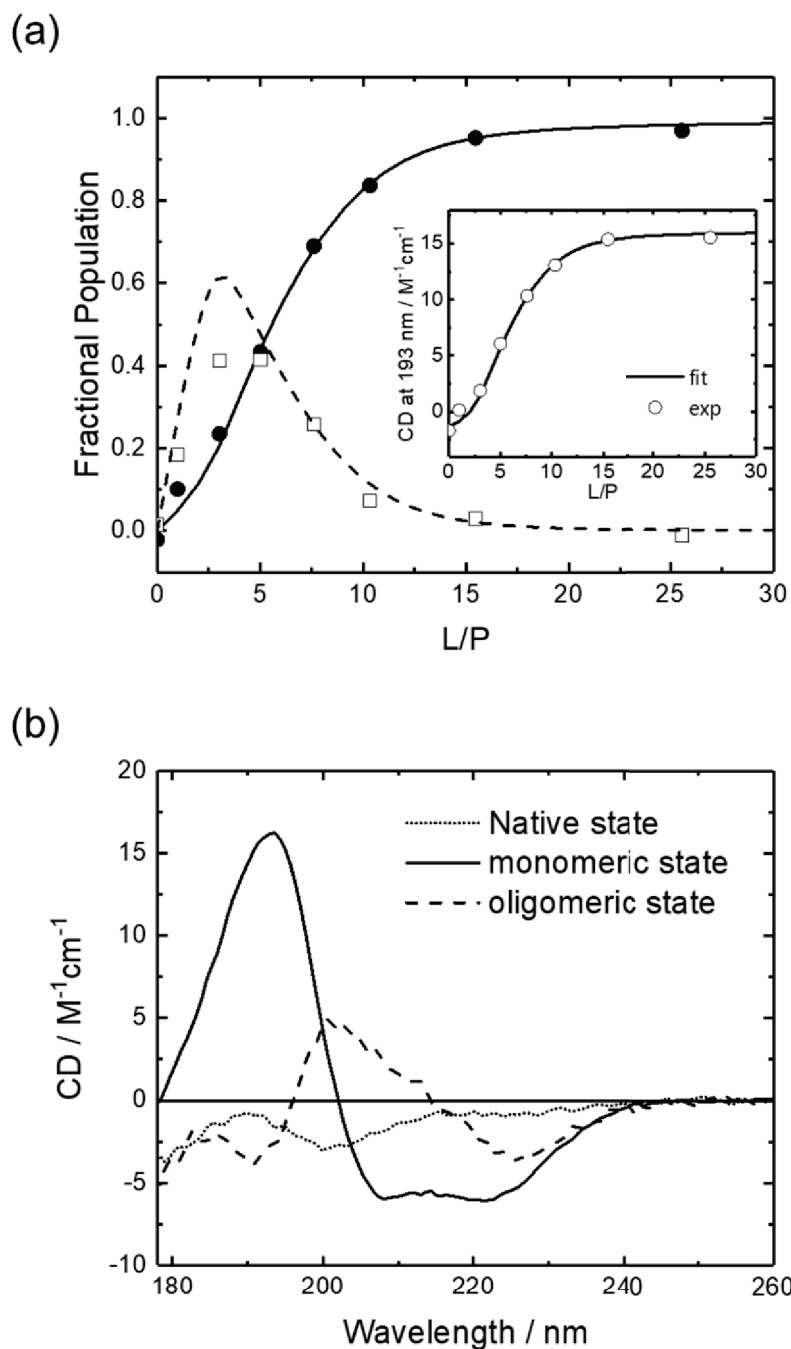


Figure 5.5. (a) L/P dependence of fractional populations of M2 in membrane-bound monomeric (closed circle: plots; solid line: fitting curve) and oligomeric states (open square: plots; dashed line: fitting curve). The fitting curves in (a) were calculated using the following optimized parameters: $K = 17500$, $K_{1z} = 3$, $z = 5$, and $n = 2.2$. The inset of (a) shows the L/P dependence of the CD at 193 nm; (b) spectra of M2 at native, membrane-bound monomeric, and oligomeric states.

In this model, the membrane-bound monomeric state of the peptide is modeled as a spherical form¹⁶². However, the helix structure of M2 might need to be treated in a cylindrical form when considering the NMR structure of M2 bound to dodecylphosphocholine micelles¹⁶⁸. In fact, when Zuckermann and Heimbürg¹⁶⁷ described the equilibrium between the peptides adsorbed on membranes and the peptide oligomers inserted into the membranes, they proposed an SPT-based model in which the membrane-bound peptide was modeled as a cylindrical form. This model might improve the fitting error in our study but it requires the detail structural parameters of cylindrical form such as the length and the radius. Since it was difficult to obtain these structural parameters of random coil, α -helix, and β -strand structures of M2, hence we used the spherical form. In fact, this form reproduced well the fractional population of the three states obtained from the global fitting simulation (Figure 5.5) and suggested the presence of oligomerization of membrane-bound peptides.

Previous research suggested that light scattering due to the self-association of peptides and liposomes induces the distortion of CD spectra¹⁶⁹ and the presence of an intermediate state in the research was attributed to the effect of light scattering distortion. We measured the optical density of the M2-DPPG liposome system at 450 nm using a commercial absorption spectrophotometer and a quartz cuvette with an optical path length of 1 cm, and observed slight light scattering in the system at an L/P ratio of 3 (Figure 5.6). Thus, we optimized the measurement system, such as the positioning of the sample holder and detector, because this optimized system realized the measurements of undistorted CD spectra of proteins even in the presence of large unilamellar vesicles^{13,14}. We observed that the raw CD spectra of M2 exhibited no baseline shift at 260 nm, which is believed to be an artifact of light scattering¹⁶⁹ (data not shown). These results indicate that the effect of light scattering on the VUVCD spectra was negligible. Therefore, the intermediate state of M2 in DPPG liposomes does not originate from scattering artifacts.

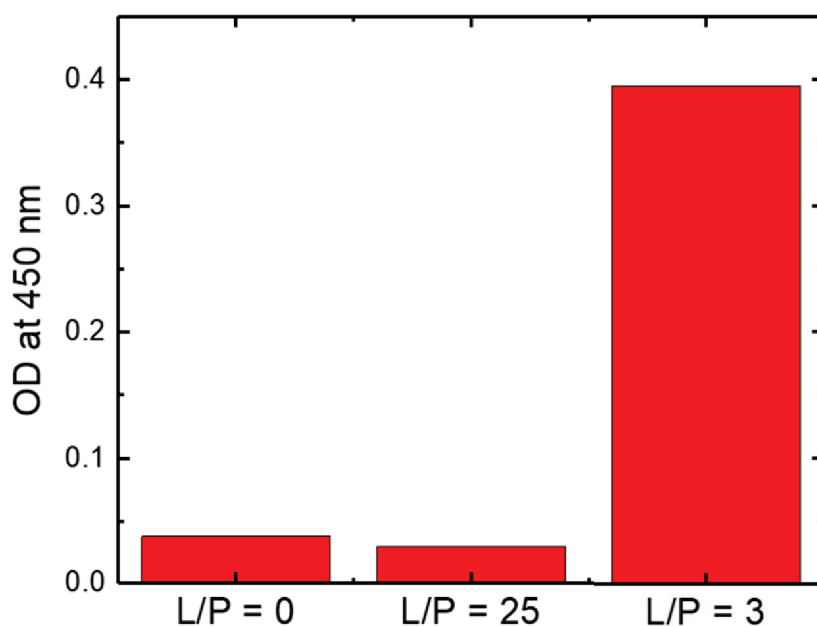


Figure 5.6. Optical density at 450 nm of M2-DPPG liposome system at the L/P of 0, 25, and 3 obtained using a commercial absorption spectrophotometer and a quartz cuvette with an optical path length of 1 cm. The concentration of lipid molecule was 400 μ M.

The spectra of M2 in the three states were analyzed using the SELCON3 program to estimate the secondary structures of M2 in the native, membrane-bound monomeric, and oligomeric states. The analytical results from the CDSSTR and BeStSel programs^{67,170} were almost consistent with those of SELCON3 (Figure 5.7). Figure 5.7 shows the secondary structure contents of M2 in the three states. The SELCON3 analysis revealed that native M2 comprised 7.5% α -helix, 28.4% β -strand, and 64.1% turn and unordered structures (others), showing that M2 forms a random coil in an aqueous solution. In contrast, M2 in the membrane-bound monomeric and oligomeric states included 70.2% and 1.2% α -helix, 10.9% and 46.3% β -strand, and 18.9% and 52.5% others, respectively. These data suggest that the oligomeric state of M2 interacting with DPPG membranes induced a large number of β -strand structures.

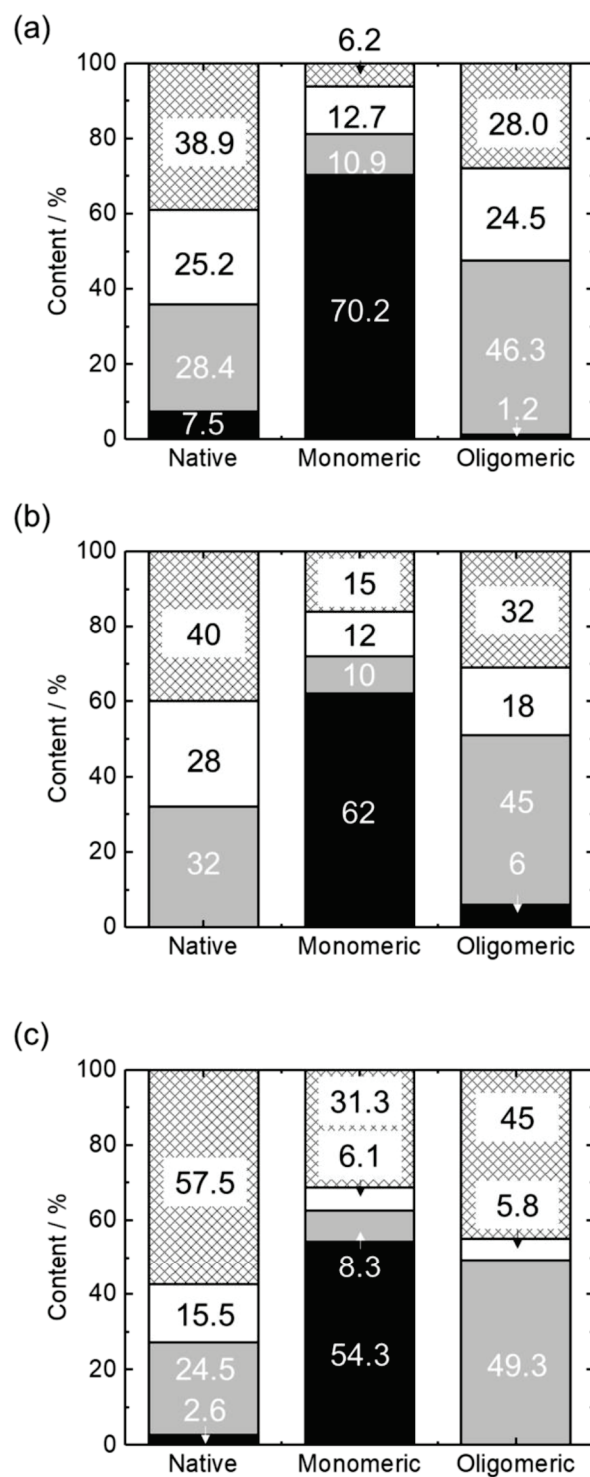


Figure 5.7. Bar graphs of secondary structures of M2 in native, membrane-bound monomeric, and oligomeric states analyzed using the (a) SELCON3, (b) CDSSTR and (c) BeStSel programs (black: α -helix; gray: β -strand; white: turn; meshed: unordered structure).

5.3.2. Linear dichroism

We then conducted LD measurements of M2 in the presence of DPPG liposomes at L/P ratios of 4 and 25, which correspond to the experimental conditions mainly occupied by the oligomeric state and the membrane-bound monomeric state, respectively, to estimate the orientation of the secondary structures (α -helices and β -strands) of M2 on the DPPG membrane surface. To obtain the LD spectra of M2, we used a liquid circulation system in which liposomes can deform from spherical to elliptical shapes in a shear flow environment^{14,35}. In the flow system, the average ratio of major axis/minor axis of dimyristoyl phosphatidylcholine liposome is approximately 1.7 at a flow velocity of 1.0 ml min⁻¹¹⁴. Because the long axis of the elliptical liposome was oriented along the flow direction, the average orientations of secondary structures in the liposomes showed slight biases, providing the LD signals depending on the secondary structure orientations against the membrane surface. M2 in DPPG liposomes at a flow velocity of 1.0 ml min⁻¹ showed a positive peak around 195 nm with a shoulder around 205 nm at L/P = 25 and a positive peak around 200 nm and a small shoulder around 220 nm at L/P = 4, as shown in Figure 5.8. Furthermore, both spectra depended on the flow velocity from 0 to 1.0 ml min⁻¹ (the insets of Figure 5.8). The observations of LD spectra mean that the helical and strand structure directly interact with the DPPG liposomes. Since M2 forms helical and strand structures at L/P = 25 and 4, respectively (Figure 5.1) and free peptides in aqueous solution show no LD signals, these results suggest that the observed LD was mainly affected by the oriented helical structure of M2 for L/P = 25 and the oriented strand structure for L/P = 4 on the elliptical liposomes.

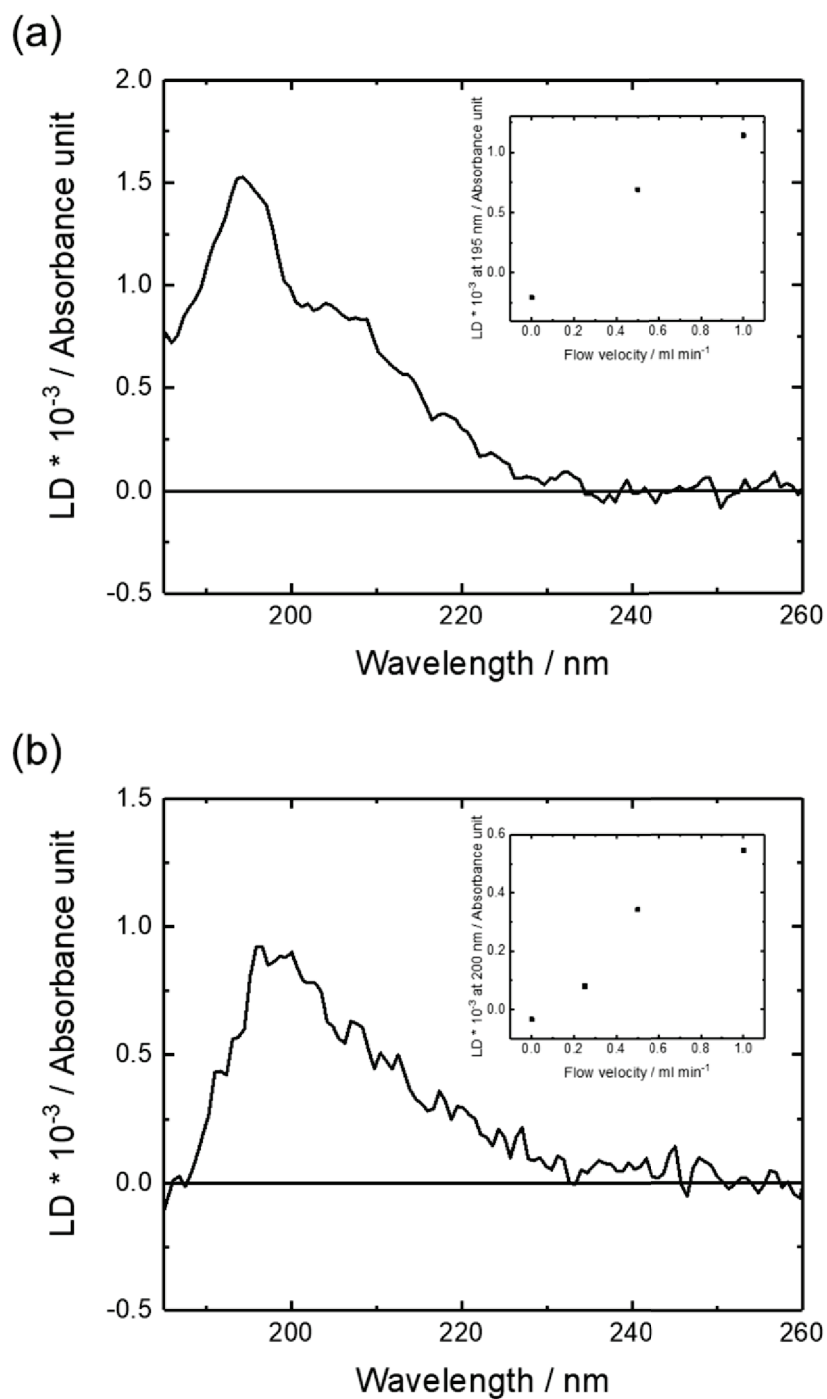


Figure 5.8. LD spectra of M2 in DPPG liposomes at the L/P of (a) 25 and (b) 4. The insets of (a) and (b) show the dependence of flow velocity on the LD at 195 and 200 nm, respectively. All spectra were recorded at 25 °C, pH 7.0, and M2 concentration of 200 μ M.

The electric or magnetic dipole moments of helical structures are approximately vertical to the helix axis at 190 nm, parallel at 208 nm, and vertical at 222 nm³⁵. Furthermore, the absorption spectrum of M2 at an L/P ratio of 25 was successfully reproduced by the three component spectra of Gaussian functions, which have peak positions around 222, 208, and 190 nm, respectively, as shown in Figure 5.9 (a). These results allowed us to analyze the LD spectra under two different assumptions: first, all M2 peptides form the same helical orientation with a single helical angle against the membrane surface; second, M2 peptides form perpendicular (transmembrane) and parallel helical structures against the membrane surface. The results under the first assumption showed that the LD spectrum could be interpreted as the angle between the M2 helix axis and the membrane normal (48°) (Figure 5.9 (b)) while those under the second assumption showed that the ratio of M2 helix axes perpendicular and parallel to the membrane surface was 1:1.2 (Figure 5.9 (c)). Both fitting analyses reproduced the experimental LD well, as shown in Figure 5.9 (d). As for the LD spectrum at an L/P of 4, the electric or magnetic dipole moments of the β -strand structure were approximately vertical to the strand axis at 195 nm, parallel at 219 nm, and vertical at 221 nm^{35,49}; however, the fitting analysis, as described in Figure 5.9, was difficult because the two dipole moments (219 and 221 nm) were very close and had inverse directions, which induced cancelation. However, a positive peak around 200 nm was clearly detected in the LD spectrum and showed that the axis of the β -strands of M2 was perpendicular to the membrane surface on average.

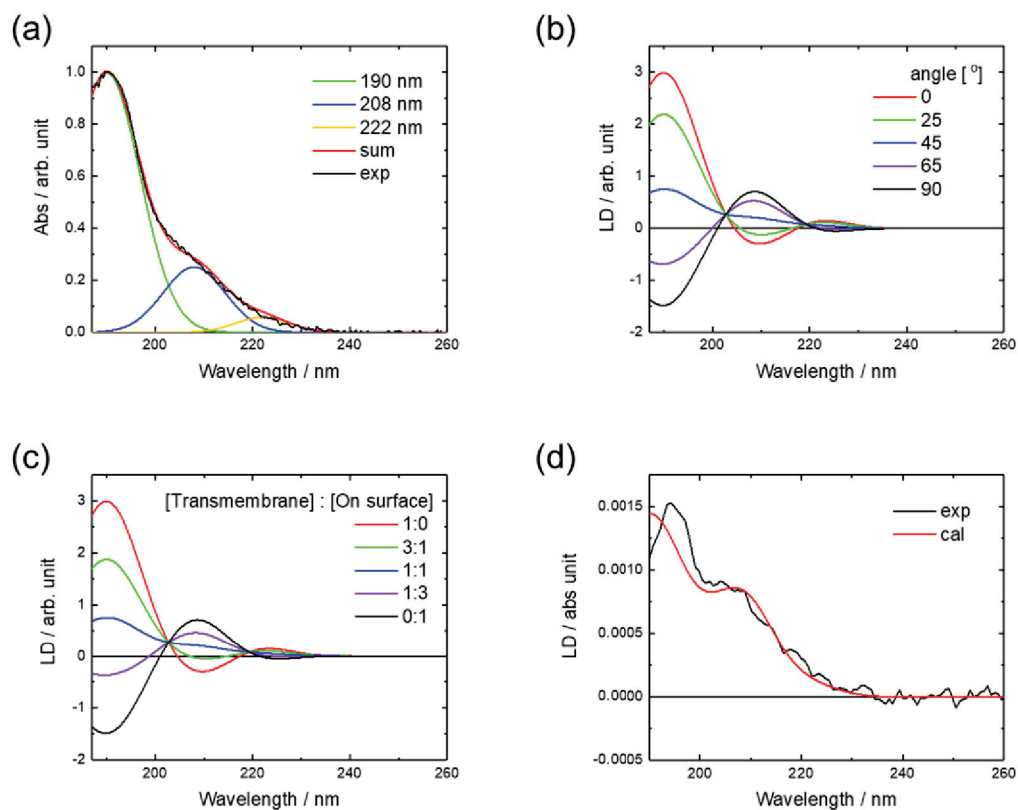


Figure 5.9. (a) absorption spectrum of M2 in the presence of DPPG liposome at $L/P = 25$. The absorption spectrum was deconvoluted into three gaussian-type contributions with peaks at 190 nm, 208 nm, and 222 nm. (b) angle dependence of theoretical LD spectra. (c) [Transmembrane]: [On surface] ratio dependence of the theoretical LD spectra. (d) experimental and calculated LD spectra of M2 in DPPG liposomes at $L/P = 25$. The calculated LD spectrum in (d) was obtained by using the optimized angle ($= 48^\circ$) or [Transmembrane]: [On surface] ratio ([Transmembrane]: [On surface] = 1:1.2).

5.3.3. Fluorescence anisotropy

To investigate the contribution of the α -helix formation in the monomeric state and the β -strand formation in the oligomeric state to the stability of lipid membranes, we measured the fluorescence anisotropy of DPPG liposomes in the presence of M2 at $L/P = 25$ and 3. Fluorescence anisotropy can monitor the degree

of dynamics or rotational mobility of DPH in liposomes as described in section 2.5.2, and the parameters are then used to investigate the lipid packing (ordering) or the membrane fluidity of lipid bilayers^{171,172}. The DPH probe is present in the hydrophobic core of liposomes and the motion of the DPH molecules is normally restricted to the gel-phase liposomes, resulting in high fluorescence anisotropy values. However, when the temperature is increased or the phase of the lipid bilayer shifts to the liquid-crystalline phase, the degree of rotational mobility of the DPH molecules increased, leading to a decrease in the anisotropy values. Figure 5.10 shows the temperature dependence of the fluorescence anisotropy values r of DPPG liposomes in the absence of M2 and at L/P = 25 and 3.

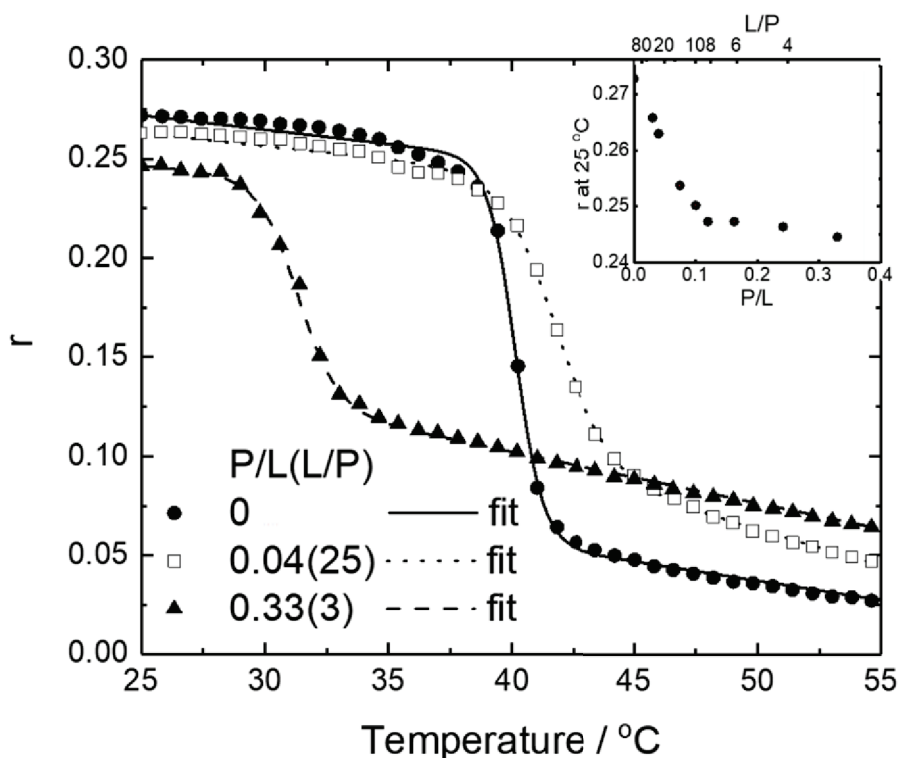


Figure 5.10. Fluorescence anisotropy values r and fitting curves of DPPG liposomes in the absence of M2 and in the presence of M2 at L/P = 25 and 3. The inset shows P/L (L/P) dependence of r at 25 °C. All data were recorded at pH 7.0 and DPPG concentration of 400 μ M.

As shown in the inset of Figure 5.10, the r at 25 °C linearly decreased as L/P decreased, up to 10, whereas r did not change below a L/P of 10, implying that the effect of M2 binding on the DPPG membrane changes around L/P = 10. We analyzed the midpoint temperature T_m and the molar enthalpy change ΔH of the phase transition of DPPG liposomes in the presence of M2 using a sigmoid function ((5.1) Equation (5.1)). The fitting curves were well fitted to the experimental data (Figure 5.10). The T_m and ΔH values are listed in Table 5.2. From this table, pure DPPG liposomes showed a phase transition temperature (T_m) of approximately 40.1 °C, which is consistent with the main phase transition temperature of the DPPG membrane ($T_m = 41$ °C), showing that the DPH fluorescence anisotropy measurement can successfully monitor the change in membrane fluidity of DPPG liposomes. The T_m of DPPG liposomes at a L/P of 25 was 41.7 °C, which was higher than that of pure DPPG liposomes. In contrast, the T_m of DPPG liposomes at L/P of 3 was 31.3 °C, showing a significant decrease. This indicates that M2 in the DPPG membranes at L/P = 3 destabilizes the bilayer structure of the membranes. Since M2 can form a monomeric helical structure and oligomeric strand structure at L/P = 25 and 3, respectively, these findings suggest that the adsorption of monomeric and oligomeric M2 on the DPPG membranes largely contributes to the stabilization and destabilization of the membrane, respectively.

Table 5.2. Midpoint temperature T_m and molar enthalpy change ΔH obtained by fitting the temperature dependence of the fluorescence anisotropy at L/P of 25 and 3 in Figure 5.10.

L/P	T_m [°C]	ΔH [kcal/mol]
Only liposome	40.12 ± 0.02	351 ± 7
25	41.71 ± 0.02	180 ± 4
3	31.31 ± 0.03	231 ± 7

5.4 Discussion

In this study, we used VUVCD spectroscopy to reveal that the conformation of M2 changed from random coil to α -helix structures via an intermediate state as the L/P ratio increased. The global fitting analysis of the VUVCD spectra based on the adsorption model indicated that α -helical M2 monomers assembled and transformed into β -strand M2 oligomers in the intermediate state. LD data also showed that the β -strand M2 oligomers bind to the membrane as the strand axis is perpendicular to the membrane surface. To elucidate the effect of oligomerization on the structure and stability of lipid membranes, further we conducted fluorescence anisotropy measurements of DPPG liposomes in the presence of M2 and revealed that the formation of an oligomeric β -strand structure contributed to the destabilization of the membrane structure. Therefore, our findings demonstrate that the oligomeric β -strand structure of M2 in membranes plays a crucial role in the disruption of the cell membrane.

Our VUVCD data showed that M2 formed a helical conformation on the membrane at L/P = 25 and in the monomeric state. The LD result at L/P = 25 could be interpreted as the two possible orientations of M2 with respect to the membrane surface: the helix axis of M2 for the membrane normal was uniformly distributed at an angle of 48° or the helix axes of M2 perpendicular and parallel to the membrane surface were mixed at a ratio of 1:1.2. In addition, our fluorescence anisotropy data showed an increase in the membrane stability at L/P = 25. According to previous research¹⁶³, pure electrostatic interactions between negatively charged DPPG headgroups and positively charged residues of peptides contributes to the increase in membrane stability, whereas the hydrophobic interaction of peptides with membrane core regions induces perturbation of lipid chain packing, leading to the destabilization of the membrane structure. Furthermore, FTIR and solid-state NMR spectroscopy have indicated that α -helical M2 analogs directly bind to the headgroups of DPPG phospholipids¹⁵⁶. If the helix axis of M2 was uniformly distributed at an angle of 48° against the membrane normal, M2 would be partially inserted into the membrane, resulting in hydrophobic interactions, destabilizing the membrane structure. Wimley¹⁵⁴ suggested four types of models for the molecular mechanism of the antimicrobial activity of M2, one of which is that M2 peptides can form a transmembrane pore. Even in this case, the polar faces of peptides whose helical orientation is

perpendicular to the membrane surface can interact with the polar headgroups of phospholipids¹⁴³, stabilizing the membrane structure. Hence, it is possible that helical M2 perpendicular to the membrane surface interacts with DPPG headgroups, showing a mixture of perpendicular and parallel helices. Further, it is likely that monomeric helical M2 interacts with DPPG headgroups and is a mixture of perpendicular and parallel helices at a ratio of 1:1.2. Because the toroidal pore formation and other models, such as carpet and detergent models do not require specific peptide-peptide interactions¹⁵⁴, it is possible that M2 peptides in the pore formation could be treated as a monomeric state.

To confirm the presence of pore formation at $L/P = 25$, we tested M2-induced leakage of calcein molecules entrapped in DPPG liposomes and found that approximately 30% of the dye molecules were released from the liposomes (Figure 5.11). This result indicates that the pores formed in liposomes at $L/P = 25$, but the M2-induced disruption of DPPG liposomes would not be completed under this condition. In contrast, the extent of liposome-entrapped calcein leakage at $L/P = 4$ was 2-fold greater than that at $L/P = 25$ (~60%). Hence, elucidating what occurred around $L/P = 4$ might be important for understanding the overall molecular mechanism of DPPG liposome disruption by M2.

We found that the α -helix monomers of M2 assembled and transformed into β -strand oligomers as the L/P ratio decreased from 25 to 4. Although our fitting analysis of the VUVCD data did not yield the unique thermodynamic parameters of the M2 adsorption to DPPG membranes due to strong cross-correlation between

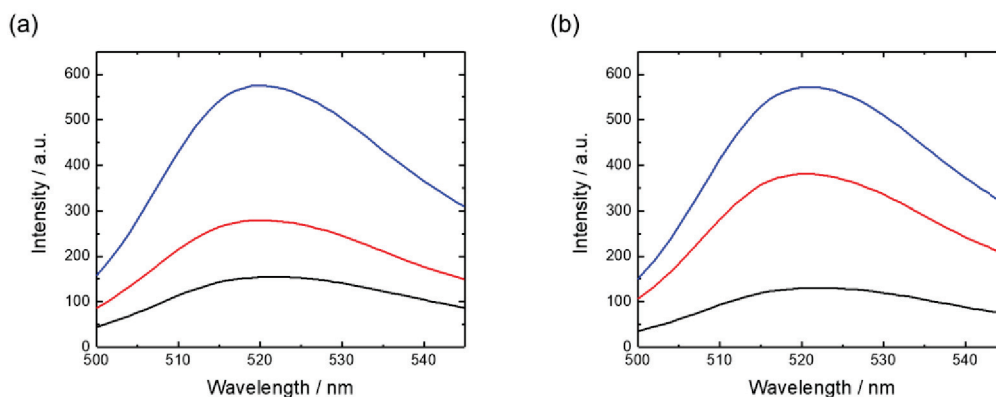


Figure 5.11. Fluorescence spectra of calcein in the calcein leakage assay before (black) and 40 min after adding M2 (red) at $L/P = 25$ (a) and 4(b). The blue lines are corresponding to the fluorescence spectra after adding Triton X-100.

each parameter and the limited number of data points (Figure 5.12), the fitting analysis suggested that M2 in the DPPG membranes formed the β -strand z-mer ($z > 2$). We also estimated that the average axis of β -strands was perpendicular to the membrane surface and confirmed that the formation of β -strand oligomers contributed to the destabilization of the membrane structure. Since the hydrophobic interaction of peptides with membrane core regions induces destabilization of the membrane structure¹⁶³, the β -strand oligomers of M2 may be buried in the DPPG membrane core or the disruption of the chain packing of DPPG membranes. These results suggest that the oligomeric β -strand M2 has unique conformations, such as the toxic β -sheet channels of protegrin-1¹⁷³ and transmembrane amyloid β ($A\beta$) oligomers¹⁷⁴. Ciudad et al. suggested that the β -strand-rich $A\beta$ 42 tetramer formed lipid-stabilized pores in a membrane-mimicking environment, in which water permeation occurred¹⁷⁴. The discussion requires further analyses such as FTIR¹⁵⁶, vibrational sum frequency generation¹⁷⁵, and Raman spectroscopy¹⁵⁷. However, the β -strand oligomers of M2 may contribute

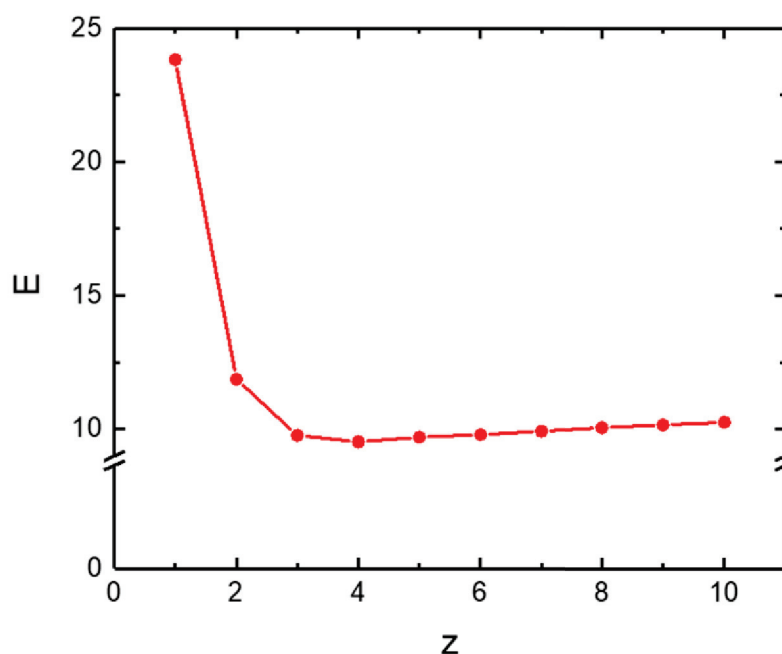


Figure 5.12. Dependence of the fitting error E on the number of subunits z of adsorbed aggregates calculated using fixed $K = 17500$ and $n = 2.2$ and K_{1z} as a variable. The minimum point was plotted as a function of z .

to the formation of stable pores in DPPG membranes, inducing the complete disruption of the membrane structure.

Previous reports¹⁷⁶ suggested that ΔH and T_m of membrane phase transition were basically correlated with each other for several membrane-bound proteins and peptides, meaning that the destabilization of membrane (decrement in T_m) would relate to the decrement in ΔH . In this study, we observed that the both ΔH and T_m of the phase transition of DPPG liposome decreased at $L/P = 3$, compared to those of pure DPPG liposome (Table 5.2), which identifies with the previous results and suggests that the penetration of oligomeric M2 peptides would contribute the destabilization membrane and the decrement in ΔH . However, the ΔH and T_m at $L/P = 25$ decreased and increased, respectively. This conflict might be induced by the unique conformations of M2 on the membrane because M2 would form two types of orientations on the membrane (the helix axes of M2 perpendicular and parallel to the membrane surface were mixed at a ratio of 1:1.2). The ΔH and T_m at $L/P = 25$ might be also interpreted from a balance between the stabilization by the electrostatic interaction and the destabilization by the pore formation.

We investigated the conformation of M2 in dimyristoyl phosphatidylglycerol liposomes and observed that M2 in the liposomes did not show the presence of an oligomeric state with a β -strand structure (data not shown). It is likely that the formation of oligomeric β -strand structures largely depends on the inherent characteristics of lipid constituents, such as the phase transition temperature and tail region length. Given that bacteria change the lipid composition, including the acyl chain, of their cell membranes in response to their environment¹⁷⁷⁻¹⁷⁹, to understand the antimicrobial mechanism of M2, it is important to characterize the detailed dependence of lipid constituents. In addition, it is important to investigate the interactions between M2 and bacterial cells¹⁸⁰ to clarify whether M2 can form β -strands when interacting with bacterial cells under physiological conditions.

In summary, by using VUVCD, LD, and fluorescence anisotropy, we have shown that M2 in DPPG liposomes formed transmembrane β -strand oligomers, which induced the destabilization of the membrane structure. Future studies will aim to characterize the mechanisms underlying the antimicrobial action of M2, which would be helpful for taking new insight into the antimicrobial mechanism of AMPs.

Chapter 6: Conclusions

In this study, we have used VUVCD spectroscopy to characterize the interaction mechanism between the three membrane-bound proteins (or peptides) and lipid membranes. VUVCD spectroscopy has been successfully applied to reveal the dependence of membrane-bound conformation on the lipid composition and the L/P molar ratio. Despite some limitations in the experimental and theoretical analyses of peripheral membrane proteins in liposomes, this study has successfully produced more-comprehensive information about the detailed mechanism between the membrane-bound proteins and lipid membranes.

AGP

We used VUVCD spectroscopy to characterize the secondary structures of AGP in the N and MB states. A comprehensive analysis of the contents, numbers of segments, and sequences of the secondary structures revealed that the membrane-bound conformation of AGP is strongly depending on the types of constituent phospholipid molecules in the liposomes. These results represent important information for understanding the membrane interaction sites and the mechanism of interaction between AGP and lipid membranes, in which at least the amphiphilic N-terminal helix and the positively charged C-terminal helix in the membrane-bound conformation would be candidates for the interaction sites with the membrane surface, with the two helices interacting with the membrane via hydrophobic and electrostatic interactions, respectively.

MBP

We used VUVCD spectroscopy and MD simulation to characterize the conformation of MBP bound to PI liposomes. The VUVCD results showed that the eight helix segments in MBP are assigned as candidate membrane-interaction sites. We performed MD simulations of peptide fragments of the candidate sites to determine whether each fragment can approach and interact with the PI membrane surface. The experimentally observed and theoretically calculated data together suggest that all eight peptide fragments can approach and interact with the

membrane surface, but only five peptide fragments remain as helix structures on the surface. Further, this combination method revealed that three of the five peptide fragments are nonamphiphilic helices that can interact electrostatically with the membrane, while the remaining fragments are amphiphilic helices that can interact hydrophobically and electrostatically with the membrane.

M2

We used VUVCD, LD, and fluorescence spectroscopies to characterize the relationships between the conformations and activities of M2 on the DPPG membrane. VUVCD and LD analyses revealed that M2 formed β -strand oligomers in DPPG liposomes. Fluorescence spectroscopies showed that the formation of β -strand oligomers induced the destabilization of the membrane structure and the leakage of calcein molecules entrapped in the liposomes. It has been commonly recognized that the formation of the helical structure of M2 on the membrane could be the driving force of the destabilization of the membrane or the antimicrobial activity; however, our findings demonstrate that the oligomeric β -strand structure of M2 in membranes also plays a crucial role in the disruption of the cell membrane.

These results demonstrate that VUVCD spectroscopy is a useful tool for characterizing the membrane-bound conformation of proteins and indicate that combining VUVCD and experimental (e.g., LD and fluorescence) or theoretical (e.g., NN and MD) methods represents a unique and improved tool for characterizing the mechanism of interaction between peripheral membrane proteins and lipid membranes. Furthermore, our data suggest that VUVCD spectroscopy highly contributes to the developments in the structural biology of membrane-bound proteins, especially for targets that are not amenable to X-ray and NMR analyses. Considerable efforts are now devoted to developing time-resolved and spatially-resolved VUVCD measurement systems in our research group. By using these novel techniques, future studies will aim to elucidate the molecular mechanisms underlying the interaction between peripheral membrane proteins and lipid membranes in more detail, which would be helpful for gaining new insights into the relationship between the interaction mechanisms and the biological functions or diseases.

Acknowledgements

The author would like to thank Associate Professor Koichi Matsuo of HiSOR, Hiroshima University, for useful comments in conducting this study. The author would also like to thank Dr. Yudai Izumi of National Institutes for Quantum Science and Technology for collaboration. The author is very grateful to Professor Kenya Shimada of HiSOR, Hiroshima University, for financial support. The author is grateful to Professor Hirofumi Namatame of HiSOR, Hiroshima University, for giving him the educationally significant opportunities to communicate how interesting science is to high school students. The author is also grateful to all the professors, associate professors, and assistant professors of HiSOR, Hiroshima University, for their effective advice in the laboratory seminar. The author is indebted to all the staffs and students of HiSOR, Hiroshima University, for their help and encouragement. Finally, the author acknowledges his parents for their very kind supports and encouragements.

Reference

- (1) Nishi, K., Maruyama, T., Halsall, H. B., Handa, T., and Otagiri, M. (2004) Binding of α 1-acid glycoprotein to membrane results in a unique structural change and ligand release. *Biochemistry* 43, 10513–10519.
- (2) Vassall, K. A., Bamm, V. V., and Harauz, G. (2015) MyelStones: the executive roles of myelin basic protein in myelin assembly and destabilization in multiple sclerosis. *Biochem. J.* 472, 17–32.
- (3) Zasloff, M. (2002) Antimicrobial peptides of multicellular organisms. *Nature* 415, 389–395.
- (4) Nguyen, P. H., Ramamoorthy, A., Sahoo, B. R., Zheng, J., Faller, P., Straub, J. E., Dominguez, L., Shea, J. E., Dokholyan, N. V., de Simone, A., Ma, B., Nussinov, R., Najafi, S., Ngo, S. T., Loquet, A., Chiricotto, M., Ganguly, P., McCarty, J., Li, M. S., Hall, C., Wang, Y., Miller, Y., Melchionna, S., Habenstein, B., Timr, S., Chen, J., Hnath, B., Strodel, B., Kayed, R., Lesné, S., Wei, G., Sterpone, F., Doig, A. J., and Derreumaux, P. (2021) Amyloid oligomers: A joint experimental/computational perspective on Alzheimer’s disease, Parkinson’s disease, type II diabetes, and amyotrophic lateral sclerosis. *Chem. Rev.* 121, 2545–2647.
- (5) Moraes, I., Evans, G., Sanchez-Weatherby, J., Newstead, S., and Stewart, P. D. S. (2014) Membrane protein structure determination - The next generation. *Biochim. Biophys. Acta - Biomembr.* 1838, 78–87.
- (6) Hagn, F., Nasr, M. L., and Wagner, G. (2018) Assembly of phospholipid nanodiscs of controlled size for structural studies of membrane proteins by NMR. *Nat. Protoc.* 13, 79–98.
- (7) Murata, K., and Wolf, M. (2018) Cryo-electron microscopy for structural analysis of dynamic biological macromolecules. *Biochim. Biophys. Acta - Gen. Subj.* 1862, 324–334.
- (8) Yao, X., Fan, X., and Yan, N. (2020) Cryo-EM analysis of a membrane protein embedded in the liposome. *Proc. Natl. Acad. Sci. U. S. A.* 117, 18497–18503.
- (9) Allen, K. N., Entova, S., Ray, L. C., and Imperiali, B. (2019) Monotopic Membrane Proteins Join the Fold. *Trends Biochem. Sci.* 44, 7–20.

- (10) Hurley, J. H. (2006) Membrane binding domains. *Biochim. Biophys. Acta - Mol. Cell Biol. Lipids* 1761, 805–811.
- (11) Harauz, G., Ishiyama, N., Hill, C. M. D., Bates, I. R., Libich, D. S., and Farès, C. (2004) Myelin basic protein - Diverse conformational states of an intrinsically unstructured protein and its roles in myelin assembly and multiple sclerosis. *Micron* 35, 503–542.
- (12) Sreerama, N., and Woody, R. W. (2004) On the analysis of membrane protein circular dichroism spectra. *Protein Sci.* 13, 100–112.
- (13) Miles, A. J., and Wallace, B. A. (2016) Circular dichroism spectroscopy of membrane proteins. *Chem. Soc. Rev.* 45, 4859–4872.
- (14) Matsuo, K., Maki, Y., Namatame, H., Taniguchi, M., and Gekko, K. (2016) Conformation of membrane-bound proteins revealed by vacuum-ultraviolet circular-dichroism and linear-dichroism spectroscopy. *Proteins Struct. Funct. Bioinforma.* 84, 349–359.
- (15) Matsuo, K., Yonehara, R., and Gekko, K. (2004) Secondary-structure analysis of proteins by vacuum-ultraviolet circular dichroism spectroscopy. *J. Biochem.* 135, 405–411.
- (16) Matsuo, K., Yonehara, R., and Gekko, K. (2005) Improved estimation of the secondary structures of proteins by vacuum-ultraviolet circular dichroism spectroscopy. *J. Biochem.* 138, 79–88.
- (17) Matsuo, K., Watanabe, H., and Gekko, K. (2008) Improved sequence-based prediction of protein secondary structures by combining vacuum-ultraviolet circular dichroism spectroscopy with neural network. *Proteins Struct. Funct. Genet.* 73, 104–112.
- (18) Matsuo, K., Namatame, H., Taniguchi, M., and Gekko, K. (2009) Membrane-induced conformational change of α 1-acid glycoprotein characterized by vacuum-ultraviolet circular dichroism spectroscopy. *Biochemistry* 48, 9103–9111.
- (19) Yagi-Utsumi, M., Matsuo, K., Yanagisawa, K., Gekko, K., and Kato, K. (2010) Spectroscopic characterization of intermolecular interaction of amyloid β promoted on GM1 micelles. *Int. J. Alzheimers. Dis.* 2011, 925073.
- (20) Ohler, B., Graf, K., Bragg, R., Lemons, T., Coe, R., Genain, C., Israelachvili, J., and Husted, C. (2004) Role of lipid interactions in autoimmune demyelination. *Biochim. Biophys. Acta - Mol. Basis Dis.* 1688, 10–17.

- (21) Riekkinen, P., Rinne, U. K., Pelliniemi, T., and Sonninen, V. (1975) Interaction between dopamine and phospholipids. Studies of the substantia nigra in Parkinson disease patients. *Arch. Neurol.* 32, 25–27.
- (22) Min, Y., Kristiansen, K., Boggs, J. M., Husted, C., Zasadzinski, J. A., and Israelachvili, J. (2009) Interaction forces and adhesion of supported myelin lipid bilayers modulated by myelin basic protein. *Proc. Natl. Acad. Sci. U. S. A.* 106, 3154–3159.
- (23) Sugiura, Y., Ikeda, K., and Nakano, M. (2015) High Membrane Curvature Enhances Binding, Conformational Changes, and Fibrillation of Amyloid- β on Lipid Bilayer Surfaces. *Langmuir* 31, 11549–11557.
- (24) Terakawa, M. S., Lee, Y. H., Kinoshita, M., Lin, Y., Sugiki, T., Fukui, N., Ikenoue, T., Kawata, Y., and Goto, Y. (2018) Membrane-induced initial structure of α -synuclein control its amyloidogenesis on model membranes. *Biochim. Biophys. Acta - Biomembr.* 1860, 757–766.
- (25) Matsumoto, K., Sukimoto, K., Nishi, K., Maruyama, T., Suenaga, A., and Otagiri, M. (2002) Characterization of Ligand Binding Sites on the α 1-Acid Glycoprotein in Humans, Bovines and Dogs. *Drug Metab. Pharmacokinet.* 17, 300–306.
- (26) Ganguly, M., Carnighan, R. H., and Westphal, U. (1967) Steroid-Protein Interactions. XIV. Interaction between Human α 1-Acid Glycoprotein and Progesterone. *Biochemistry* 6, 2803–2814.
- (27) Boggs, J. M. (2006) Myelin basic protein: A multifunctional protein. *Cell. Mol. Life Sci.* 63, 1945–1961.
- (28) Han, H., Myllykoski, M., Ruskamo, S., Wang, C., and Kursula, P. (2013) Myelin-specific proteins: A structurally diverse group of membrane-interacting molecules. *BioFactors* 39, 233–241.
- (29) Harauz, G., Ladizhansky, V., and Boggs, J. M. (2009) Structural polymorphism and multifunctionality of myelin basic protein. *Biochemistry* 48, 8094–8104.
- (30) Harauz, G., and Boggs, J. M. (2013) Myelin management by the 18.5-kDa and 21.5-kDa classic myelin basic protein isoforms. *J. Neurochem.* 125, 334–361.
- (31) Melo, M. N., Ferre, R., and Castanho, M. A. R. B. (2009) Antimicrobial peptides: Linking partition, activity and high membrane-bound concentrations. *Nat. Rev. Microbiol.* 7, 245–250.
- (32) Hope, M. J., Bally, M. B., Webb, G., and Cullis, P. R. (1985) Production of large unilamellar vesicles by a rapid extrusion procedure. Characterization of size distribution,

- trapped volume and ability to maintain a membrane potential. *Biochim. Biophys. Acta - Biomembr.* 812, 55–65.
- (33) Bernadotte, S., Atkins, A. J., and Jacob, C. R. (2012) Origin-independent calculation of quadrupole intensities in X-ray spectroscopy. *J. Chem. Phys.* 137.
- (34) Barron, L. D. (2009) *Molecular Light Scattering and Optical Activity*. Cambridge University Press.
- (35) Rodger, A., Nordén, B., and Dafforn, T. (2010) *Linear Dichroism and Circular Dichroism: A Textbook on Polarized-Light Spectroscopy*. Royal Society of Chemistry.
- (36) Fasman, G. D. (1996) *Circular Dichroism and the Conformational Analysis of Biomolecules*. Springer, Boston, MA.
- (37) Nakanishi, K., Berova, N., and Woody, R. W. (2000) *Circular Dichroism: Principles and Applications*.
- (38) 熊代宗弘. (2019) 真空紫外円二色性によるミエリン塩基性タンパク質の生体膜相互作用研究 広島大学 修士論文.
- (39) Sreerama, N., and Woody, R. W. (2004) Computation and Analysis of Protein Circular Dichroism Spectra. *Methods Enzymol.* 383, 318–351.
- (40) Ramachandran, G. N., Ramakrishnan, C., and Sasisekharan, V. (1963) Stereochemistry of polypeptide chain configurations. *J. Mol. Biol.* 7, 95–99.
- (41) Lovell, S. C., Davis, I. W., Arendall, W. B., De Bakker, P. I. W., Word, J. M., Prisant, M. G., Richardson, J. S., and Richardson, D. C. (2003) Structure validation by C α geometry: ϕ , ψ and C β deviation. *Proteins Struct. Funct. Genet.* 50, 437–450.
- (42) Shashilov, V. A., and Lednev, I. K. (2010) Advanced statistical and numerical methods for spectroscopic characterization of protein structural evolution. *Chem. Rev.* 110, 5692–5713.
- (43) Woody, R. W. (2015) The development and current state of protein circular dichroism. *Biomed. Spectrosc. Imaging* 4, 5–34.
- (44) Shi, Z., Woody, R. W., and Kallenbach, N. (2002) Is polyproline II a major backbone conformation in unfolded proteins? *Adv. Protein Chem.* 62, 163–240.
- (45) Kumar, A., Toal, S. E., Diguseppi, D., Schweitzer-Stenner, R., and Wong, B. M. (2020) Water-Mediated Electronic Structure of Oligopeptides Probed by Their UV Circular Dichroism, Absorption Spectra, and Time-Dependent DFT Calculations. *J. Phys. Chem. B* 124, 2579–2590.

- (46) Shimada, K., and Matsuo, K. (Ed.) (2020) HiSOR Activity Report 2020.
- (47) Sawada, M., Namatame, H., and Taniguchi, M. (2013) Optical design of a compact and practical UV beamline at HiSOR-BL12. *J. Phys. Conf. Ser.* 425, 162010.
- (48) Matsuo, K., and Gekko, K. (2013) Construction of a synchrotron-radiation vacuum-ultraviolet circular-dichroism spectrophotometer and its application to the structural analysis of biomolecules. *Bull. Chem. Soc. Jpn.* 86, 675–689.
- (49) Rodger, A., Rajendra, J., Marrington, R., Ardhammar, M., Nordén, B., Hirst, J. D., Gilbert, A. T. B., Dafforn, T. R., Halsall, D. J., Woolhead, C. A., Robinson, C., Pinheiro, T. J. T., Kazlauskaitė, J., Seymour, M., Perez, N., and Hannon, M. J. (2002) Flow oriented linear dichroism to probe protein orientation in membrane environments. *Phys. Chem. Chem. Phys.* 4, 4051–4057.
- (50) Lakowicz, J. R. (2006) Principles of Fluorescence Spectroscopy 3rd ed. Springer.
- (51) Matsuzaki, K., Sugishita, K. I., Ishibe, N., Ueha, M., Nakata, S., Miyajima, K., and Epanand, R. M. (1998) Relationship of membrane curvature to the formation of pores by magainin 2. *Biochemistry* 37, 11856–11863.
- (52) Allen, T. M., and Cleland, L. G. (1980) Serum-induced leakage of liposome contents. *BBA - Biomembr.* 597, 418–426.
- (53) Jones, D. T. (1999) Protein secondary structure prediction based on position-specific scoring matrices. *J. Mol. Biol.* 292, 195–202.
- (54) Schönfeld, D. L., Ravelli, R. B. G., Mueller, U., and Skerra, A. (2008) The 1.8-Å Crystal Structure of α 1-Acid Glycoprotein (Orosomuroid) Solved by UV RIP Reveals the Broad Drug-Binding Activity of This Human Plasma Lipocalin. *J. Mol. Biol.* 384, 393–405.
- (55) Nishi, K., Sakai, N., Komine, Y., Maruyama, T., Halsall, H. B., and Otagiri, M. (2002) Structural and drug-binding properties of α 1-acid glycoprotein in reverse micelles. *Biochim. Biophys. Acta - Proteins Proteomics* 1601, 185–191.
- (56) Kopecký, V., Etrich, R., Hofbauerová, K., and Baumruk, V. (2003) Structure of human α 1-acid glycoprotein and its high-affinity binding site. *Biochem. Biophys. Res. Commun.* 300, 41–46.
- (57) Scirè, A., Baldassarre, M., Lupidi, G., and Tanfani, F. (2011) Importance of pH and disulfide bridges on the structural and binding properties of human α 1-acid glycoprotein. *Biochimie* 93, 1529–1536.

- (58) Lupidi, G., Camaioni, E., Khalifé, H., Avenali, L., Damiani, E., Tanfani, F., and Scirè, A. (2012) Characterization of thymoquinone binding to human α_1 -acid glycoprotein. *J. Pharm. Sci.* *101*, 2564–2573.
- (59) Johannessen, C., Pendrill, R., Widmalm, G., Hecht, L., and Barron, L. D. (2011) Glycan structure of a high-mannose glycoprotein from raman optical activity. *Angew. Chemie - Int. Ed.* *50*, 5349–5351.
- (60) Kopecký, V., Ettrich, R., Pazderka, T., Hofbauerová, K., Řeha, D., and Baumruk, V. (2016) Influence of ligand binding on structure and thermostability of human α_1 -acid glycoprotein. *J. Mol. Recognit.* *29*, 70–79.
- (61) Nishi, K., Komine, Y., Fukunaga, N., Maruyama, T., Suenaga, A., and Otagiri, M. (2006) Involvement of disulfide bonds and histidine 172 in a unique β -sheet to α -helix transition of α_1 -acid glycoprotein at the biomembrane interface. *Proteins : Structure, Function, and Bioinforma.* *63*, 611–620.
- (62) Zhang, X., Ge, N., and Keiderling, T. A. (2007) Electrostatic and hydrophobic interactions governing the interaction and binding of β -lactoglobulin to membranes. *Biochemistry* *46*, 5252–5260.
- (63) Muruganandam, G., Bürck, J., Ulrich, A. S., Kursula, I., and Kursula, P. (2013) Lipid membrane association of myelin proteins and peptide segments studied by oriented and synchrotron radiation circular dichroism spectroscopy. *J. Phys. Chem. B* *117*, 14983–14993.
- (64) Marcus, A. J., Ullman, H. L., and Safier, L. B. (1969) Lipid composition of subcellular particles of human blood platelets. *J. Lipid Res.* *10*, 108–114.
- (65) Pace, C. N., Vajdos, F., Fee, L., Grimsley, G., and Gray, T. (1995) How to measure and predict the molar absorption coefficient of a protein. *Protein Sci.* *4*, 2411–2423.
- (66) Wallace, B. A., Lees, J. G., Orry, A. J. W., Lobley, A., and Janes, R. W. (2003) Analyses of circular dichroism spectra of membrane proteins. *Protein Sci.* *12*, 875–884.
- (67) Sreerama, N., and Woody, R. W. (2000) Estimation of protein secondary structure from circular dichroism spectra: Comparison of CONTIN, SELCON, and CDSSTR methods with an expanded reference set. *Anal. Biochem.* *287*, 252–260.
- (68) Sreerama, N., Venyaminov, S. Y. U., and Woody, R. W. (1999) Estimation of the number of α -helical and β -strand segments in proteins using circular dichroism spectroscopy. *Protein Sci.* *8*, 370–380.

- (69) Park, K., Perczel, A., and Fasman, G. D. (1992) Differentiation between transmembrane helices and peripheral helices by the deconvolution of circular dichroism spectra of membrane proteins. *Protein Sci.* 1, 1032–1049.
- (70) Bayard, B., and Fournet, B. (1976) Hydrazinolysis and nitrous acid deamination of the carbohydrate moiety of alpha1-acid glycoprotein. *Carbohydr. Res.* 46, 75–86.
- (71) Patil, Y. P., and Jadhav, S. (2014) Novel methods for liposome preparation. *Chem. Phys. Lipids* 177, 8–18.
- (72) Bürck, J., Wadhvani, P., Fanghänel, S., and Ulrich, A. S. (2016) Oriented Circular Dichroism: A Method to Characterize Membrane-Active Peptides in Oriented Lipid Bilayers. *Acc. Chem. Res.* 49, 184–192.
- (73) Kabsch, W., and Sander, C. (1983) Dictionary of protein secondary structure: Pattern recognition of hydrogen-bonded and geometrical features. *Biopolymers* 22, 2577–2637.
- (74) Kabsch, W., and Sander, C. (1983) How good are predictions of protein secondary structure? *FEBS Lett.* 155, 179–182.
- (75) Gautier, R., Douguet, D., Antonny, B., and Drin, G. (2008) HELIQUEST: A web server to screen sequences with specific α -helical properties. *Bioinformatics* 24, 2101–2102.
- (76) Zhai, J., Wooster, T. J., Hoffmann, S. V., Lee, T. H., Augustin, M. A., and Aguilar, M. I. (2011) Structural rearrangement of β -lactoglobulin at different oil-water interfaces and its effect on emulsion stability. *Langmuir* 27, 9227–9236.
- (77) Mo, H., Tay, K. G., and Ng, H. Y. (2008) Fouling of reverse osmosis membrane by protein (BSA): Effects of pH, calcium, magnesium, ionic strength and temperature. *J. Memb. Sci.* 315, 28–35.
- (78) Zhao, Y., Li, F., Carvajal, M. T., and Harris, M. T. (2009) Interactions between bovine serum albumin and alginate: An evaluation of alginate as protein carrier. *J. Colloid Interface Sci.* 332, 345–353.
- (79) Gorbenko, G. P., Ioffe, V. M., and Kinnunen, P. K. J. (2007) Binding of lysozyme to phospholipid bilayers: Evidence for protein aggregation upon membrane association. *Biophys. J.* 93, 140–153.
- (80) Cornell, D. G., and Patterson, D. L. (1989) Interaction of phospholipids in monolayers with β -lactoglobulin adsorbed from solution. *J. Agric. Food Chem.* 37, 1455–1459.

- (81) Litzinger, D. C., and Huang, L. (1992) Phosphatidylethanolamine liposomes: drug delivery, gene transfer and immunodiagnostic applications. *BBA - Rev. Biomembr.* 1113, 201–227.
- (82) Van Den Brink-Van Der Laan, E., Antoinette Killian, J., and De Kruijff, B. (2004) Nonbilayer lipids affect peripheral and integral membrane proteins via changes in the lateral pressure profile. *Biochim. Biophys. Acta - Biomembr.* 1666, 275–288.
- (83) Echteld, C. J. A. Van, Stigt, R. Van, Kruijff, B. De, J. Leunissen-Bijvelt, A.J. Verkleij, and Gier, J. De. (1981) Gramicidin promotes formation of the hexagonal HII phase in aqueous dispersions of phosphatidylethanolamine and phosphatidylcholine. *Biochim. Biophys. Acta - Biomembr.* 648, 287–291.
- (84) Nishi, K., Komine, Y., Sakai, N., Maruyama, T., and Otagiri, M. (2005) Cooperative effect of hydrophobic and electrostatic forces on alcohol-induced α -helix formation of α 1-acid glycoprotein. *FEBS Lett.* 579, 3596–3600.
- (85) Moncelli, M. R., Becucci, L., and Guidelli, R. (1994) The intrinsic pKa values for phosphatidylcholine, phosphatidylethanolamine, and phosphatidylserine in monolayers deposited on mercury electrodes. *Biophys. J.* 66, 1969–1980.
- (86) Zsila, F., and Iwao, Y. (2007) The drug binding site of human α 1-acid glycoprotein: Insight from induced circular dichroism and electronic absorption spectra. *Biochim. Biophys. Acta - Gen. Subj.* 1770, 797–809.
- (87) Yamamoto, T., Izumi, S., and Gekko, K. (2004) Mass spectrometry on hydrogen/deuterium exchange of dihydrofolate reductase: Effects of ligand binding. *J. Biochem.* 135, 663–671.
- (88) Homchaudhuri, L., Polverini, E., Gao, W., Harauz, G., and Boggs, J. M. (2009) Influence of membrane surface charge and post-translational modifications to myelin basic protein on its ability to tether the Fyn-SH3 domain to a membrane in vitro. *Biochemistry* 48, 2385–2393.
- (89) Aggarwal, S., Yurlova, L., and Simons, M. (2011) Central nervous system myelin: Structure, synthesis and assembly. *Trends Cell Biol.* 21, 585–593.
- (90) Stassart, R. M., Möbius, W., Nave, K. A., and Edgar, J. M. (2018) The axon-myelin unit in development and degenerative disease. *Front. Neurosci.* 12.
- (91) Stadelmann, C., Timmler, S., Barrantes-Freer, A., and Simons, M. (2019) Myelin in the central nervous system: structure, function, and pathology. *Physiol. Rev.* 99, 1381–1431.

- (92) Yang, L., Tan, D., and Piao, H. (2016) Myelin basic protein citrullination in multiple sclerosis: a potential therapeutic target for the pathology. *Neurochem. Res.* *41*, 1845–1856.
- (93) Compston, A., and Coles, A. (2008) Multiple sclerosis. *Lancet* *372*, 1502–1517.
- (94) Gow, A., and Smith, R. (1989) The thermodynamically stable state of myelin basic protein in aqueous solution is a flexible coil. *Biochem. J.* *257*, 535–540.
- (95) Stadler, A. M., Stingaciu, L., Radulescu, A., Holderer, O., Monkenbusch, M., Biehl, R., and Richter, D. (2014) Internal nanosecond dynamics in the intrinsically disordered myelin basic protein. *J. Am. Chem. Soc.* *136*, 6987–6994.
- (96) Vassall, K. A., Jenkins, A. D., Bamm, V. V., and Harauz, G. (2015) Thermodynamic analysis of the disorder-to- α -helical transition of 18.5-kDa myelin basic protein reveals an equilibrium intermediate representing the most compact conformation. *J. Mol. Biol.* *427*, 1977–1992.
- (97) Bamm, V. V., De Avila, M., Smith, G. S. T., Ahmed, M. A. M., and Harauz, G. (2011) Structured functional domains of myelin basic protein: Cross talk between actin polymerization and Ca²⁺-dependent calmodulin interaction. *Biophys. J.* *101*, 1248–1256.
- (98) Libich, D. S., and Harauz, G. (2008) Backbone dynamics of the 18.5 kDa isoform of myelin basic protein reveals transient α -helices and a calmodulin-binding site. *Biophys. J.* *94*, 4847–4866.
- (99) Raasakka, A., Ruskamo, S., Kowal, J., Barker, R., Baumann, A., Martel, A., Tuusa, J., Myllykoski, M., Bürck, J., Ulrich, A. S., Stahlberg, H., and Kursula, P. (2017) Membrane association landscape of myelin basic protein portrays formation of the myelin major dense line. *Sci. Rep.* *7*, 4974.
- (100) Widder, K., Träger, J., Kerth, A., Harauz, G., and Hinderberger, D. (2018) Interaction of myelin basic protein with myelin-like lipid monolayers at air-water interface. *Langmuir* *34*, 6095–6108.
- (101) ter Beest, M. B. A., and Hoekstra, D. (1993) Interaction of myelin basic protein with artificial membranes: parameters governing binding, aggregation and dissociation. *Eur. J. Biochem.* *211*, 689–696.
- (102) Boggs, J. M., Stamp, D., and Moscarello, M. A. (1982) Effect of pH and fatty acid chain length on the interaction of myelin basic protein with phosphatidylglycerol. *Biochemistry* *21*, 1208–1214.

- (103) Nawaz, S., Kippert, A., Saab, A. S., Werner, H. B., Lang, T., Nave, K. A., and Simons, M. (2009) Phosphatidylinositol 4,5-bisphosphate-dependent interaction of myelin basic protein with the plasma membrane in oligodendroglial cells and its rapid perturbation by elevated calcium. *J. Neurosci.* 29, 4794–4807.
- (104) Inouye, H., and Kirschner, D. A. (1988) Membrane interactions in nerve myelin: II. determination of surface charge from biochemical data. *Biophys. J.* 53, 247–260.
- (105) Musse, A. A., Gao, W., Homchaudhuri, L., Boggs, J. M., and Harauz, G. (2008) Myelin basic protein as a “PI(4,5)P2-modulin”: A new biological function for a major central nervous system protein. *Biochemistry* 47, 10372–10382.
- (106) Steck, A. J., Siegrist, H. P., Zahler, P., and Herschkowitz, N. N. (1976) Lipid-protein interactions with native and modified myelin basic protein. *Biochim. Biophys. Acta - Biomembr.* 455, 343–352.
- (107) Ishiyama, N., Bates, I. R., Hill, C. M., Wood, D. D., Matharu, P., Viner, N. J., Moscarello, M. A., and Harauz, G. (2001) The effects of deimination of myelin basic protein on structures formed by its interaction with phosphoinositide-containing lipid monolayers. *J. Struct. Biol.* 136, 30–45.
- (108) Matsuo, K., Kumashiro, M., and Gekko, K. (2020) Characterization of the mechanism of interaction between α 1-acid glycoprotein and lipid membranes by vacuum-ultraviolet circular-dichroism spectroscopy. *Chirality* 32, 594–604.
- (109) Sunhwan, J., Taehoon, K., Vidyashankara, I. G., and Wonpil, I. (2008) CHARMM-GUI: a web-based graphical user interface for CHARMM. *J. Comput. Chem.* 29, 1859–1865.
- (110) Qi, Y., Cheng, X., Lee, J., Vermaas, J. V., Pogorelov, T. V., Tajkhorshid, E., Park, S., Klauda, J. B., and Im, W. (2015) CHARMM-GUI HMMM builder for membrane simulations with the highly mobile membrane-mimetic model. *Biophys. J.* 109, 2012–2022.
- (111) Monje-Galvan, V., Warburton, L., and Klauda, J. B. (2019) Setting up all-atom molecular dynamics simulations to study the interactions of peripheral membrane proteins with model lipid bilayers. *Methods Mol. Biol.* 1949, 325–339.
- (112) Wildermuth, K. D., Monje-Galvan, V., Warburton, L. M., and Klauda, J. B. (2019) Effect of membrane lipid packing on stable binding of the ALPS peptide. *J. Chem. Theory Comput.* 15, 1418–1429.

- (113) Humphrey, W., Dalke, A., and Schulten, K. (1996) VMD: visual molecular dynamics. *J. Mol. Graph.* 14, 33–38.
- (114) Lomize, M. A., Pogozheva, I. D., Joo, H., Mosberg, H. I., and Lomize, A. L. (2012) OPM database and PPM web server: resources for positioning of proteins in membranes. *Nucleic Acids Res.* 40, D370–D376.
- (115) Abraham, M. J., Murtola, T., Schulz, R., Páll, S., Smith, J. C., Hess, B., and Lindah, E. (2015) Gromacs: high performance molecular simulations through multi-level parallelism from laptops to supercomputers. *SoftwareX* 1–2, 19–25.
- (116) Huang, J., Rauscher, S., Nawrocki, G., Ran, T., Feig, M., De Groot, B. L., Grubmüller, H., and MacKerell, A. D. (2017) CHARMM36m: an improved force field for folded and intrinsically disordered proteins. *Nat. Methods* 14, 71–73.
- (117) Nosé, S. (1984) A unified formulation of the constant temperature molecular dynamics methods. *J. Chem. Phys.* 81, 511–519.
- (118) Hoover, W. G. (1985) Canonical dynamics: equilibrium phase-space distributions. *Phys. Rev. A* 31, 1695–1697.
- (119) Darden, T., York, D., and Pedersen, L. (1993) Particle mesh Ewald: an N·log(N) method for Ewald sums in large systems. *J. Chem. Phys.* 98, 10089–10092.
- (120) Hess, B. (2008) P-LINCS: a parallel linear constraint solver for molecular simulation. *J. Chem. Theory Comput.* 4, 116–122.
- (121) Greenfield, N., and Fasman, G. D. (1969) Computed circular dichroism spectra for the evaluation of protein conformation. *Biochemistry* 8, 4108–4116.
- (122) Robert W. Woody. (2010) Circular dichroism of intrinsically disordered proteins. *Instrum. Anal. Intrinsically Disord. Proteins Assess. Struct. Conform.* 303–322.
- (123) Polverini, E., Fasano, A., Zito, F., Riccio, P., and Cavatorta, P. (1999) Conformation of bovine myelin basic protein purified with bound lipids. *Eur. Biophys. J.* 28, 351–355.
- (124) Haas, H., Oliveira, C. L. P., Torriani, I. L., Polverini, E., Fasano, A., Carlone, G., Cavatorta, P., and Riccio, P. (2004) Small angle X-ray scattering from lipid-bound myelin basic protein in solution. *Biophys. J.* 86, 455–460.
- (125) Bates, I. R., Feix, J. B., Boggs, J. M., and Harauz, G. (2004) An Immunodominant epitope of myelin basic protein is an amphipathic α -helix. *J. Biol. Chem.* 279, 5757–5764.

- (126) Bates, I. R., Libich, D. S., Wood, D. D., Moscarello, M. A., and Harauz, G. (2002) An Arg/Lys → Gln mutant of recombinant murine myelin basic protein as a mimic of the deiminated form implicated in multiple sclerosis. *Protein Expr. Purif.* 25, 330–341.
- (127) Randall, C. S., and Zand, R. (1985) Spectroscopic assessment of secondary and tertiary structure in myelin basic protein. *Biochemistry* 24, 1998–2004.
- (128) Matsuo, K., Sakurada, Y., Yonehara, R., Kataoka, M., and Gekko, K. (2007) Secondary-structure analysis of denatured proteins by vacuum-ultraviolet circular dichroism spectroscopy. *Biophys. J.* 92, 4088–4096.
- (129) Wang, C., Neugebauer, U., Bürck, J., Myllykoski, M., Baumgärtel, P., Popp, J., and Kursula, P. (2011) Charge isomers of myelin basic protein: Structure and interactions with membranes, nucleotide analogues, and calmodulin. *PLoS One* 6, e19915.
- (130) Buchan, D. W. A., and Jones, D. T. (2019) The PSIPRED Protein Analysis Workbench: 20 years on. *Nucleic Acids Res.* 47, W402–W407.
- (131) Drozdetskiy, A., Cole, C., Procter, J., and Barton, G. J. (2015) JPred4: A protein secondary structure prediction server. *Nucleic Acids Res.* 43, W389–W394.
- (132) Geourjon, C., and Deléage, G. (1995) SOPMA: significant improvements in protein secondary structure prediction by consensus prediction from multiple alignments. *Bioinformatics* 11, 681–684.
- (133) Monje-Galvan, V., and Klauda, J. B. (2016) Peripheral membrane proteins: tying the knot between experiment and computation. *Biochim. Biophys. Acta - Biomembr.* 1858, 1584–1593.
- (134) Ohkubo, Y. Z., Pogorelov, T. V., Arcario, M. J., Christensen, G. A., and Tajkhorshid, E. (2012) Accelerating membrane insertion of peripheral proteins with a novel membrane mimetic model. *Biophys. J.* 102, 2130–2139.
- (135) Baylon, J. L., and Tajkhorshid, E. (2015) Capturing spontaneous membrane insertion of the influenza virus hemagglutinin fusion peptide. *J. Phys. Chem. B* 119, 7882–7893.
- (136) Elmore, D. E. (2006) Molecular dynamics simulation of a phosphatidylglycerol membrane. *FEBS Lett.* 580, 144–148.
- (137) Polverini, E., Coll, E. P., Tieleman, D. P., and Harauz, G. (2011) Conformational choreography of a molecular switch region in myelin basic protein-Molecular dynamics shows induced folding and secondary structure type conversion upon threonyl phosphorylation in both

aqueous and membrane-associated environments. *Biochim. Biophys. Acta - Biomembr.* 1808, 674–683.

(138) Homchaudhuri, L., De Avila, M., Nilsson, S. B., Bessonov, K., Smith, G. S. T., Bamm, V. V., Musse, A. A., Harauz, G., and Boggs, J. M. (2010) Secondary structure and solvent accessibility of a calmodulin-binding C-terminal segment of membrane-associated myelin basic protein. *Biochemistry* 49, 8955–8966.

(139) Hughes, J. M. (2011) Preserving the Lifesaving Power of Antimicrobial Agents. *JAMA* 305, 1027.

(140) Hancock, R. E. W., and Sahl, H. G. (2006) Antimicrobial and host-defense peptides as new anti-infective therapeutic strategies. *Nat. Biotechnol.* 24, 1551–1557.

(141) Matsuzaki, K. (2009) Control of cell selectivity of antimicrobial peptides. *Biochim. Biophys. Acta - Biomembr.* 1788, 1687–1692.

(142) Lei, J., Sun, L. C., Huang, S., Zhu, C., Li, P., He, J., Mackey, V., Coy, D. H., and He, Q. Y. (2019) The antimicrobial peptides and their potential clinical applications. *Am. J. Transl. Res.* 11, 3919–3931.

(143) Matsuzaki, K. (Ed.) (2019) Antimicrobial Peptides Basics for Clinical Application. Springer, Singapore, Singapore.

(144) Benfield, A. H., and Henriques, S. T. (2020) Mode-of-Action of Antimicrobial Peptides: Membrane Disruption vs. Intracellular Mechanisms. *Front. Med. Technol.* 2, 610997.

(145) Zasloff, M. (1987) Magainins, a class of antimicrobial peptides from *Xenopus* skin: Isolation, characterization of two active forms, and partial cDNA sequence of a precursor. *Proc. Natl. Acad. Sci. U. S. A.* 84, 5449–5453.

(146) Bechinger, B., Zasloff, M., and Opella, S. J. (1993) Structure and orientation of the antibiotic peptide magainin in membranes by solid-state nuclear magnetic resonance spectroscopy. *Protein Sci.* 2, 2077–2084.

(147) Tamba, Y., and Yamazaki, M. (2005) Single giant unilamellar vesicle method reveals effect of antimicrobial peptide magainin 2 on membrane permeability. *Biochemistry* 44, 15823–15833.

(148) Wenk, M. R., and Seelig, J. (1998) Magainin 2 amide interaction with lipid membranes: Calorimetric detection of peptide binding and pore formation. *Biochemistry* 37, 3909–3916.

- (149) Matsuzaki, K., Murase, O., Tokuda, H., Funakoshi, S., and Miyajima, K. (1994) Orientational and Aggregational States of Magainin 2 in Phospholipid Bilayers. *Biochemistry* 33, 3342–3349.
- (150) Matsuzaki, K., Murase, O., and Miyajima, K. (1995) Kinetics of Pore Formation by an Antimicrobial Peptide, Magainin 2, in Phospholipid Bilayers. *Biochemistry* 34, 12553–12559.
- (151) Schümann, M., Dathe, M., Wieprecht, T., Beyermann, M., and Bienert, M. (1997) The tendency of magainin to associate upon binding to phospholipid bilayers. *Biochemistry* 36, 4345–4351.
- (152) Gregory, S. M., Pokorny, A., and Almeida, P. F. F. (2009) Magainin 2 revisited: a test of the quantitative model for the all-or-none permeabilization of phospholipid vesicles. *Biophys. J.* 96, 116–131.
- (153) Travkova, O. G., Moehwald, H., and Brezesinski, G. (2017) The interaction of antimicrobial peptides with membranes. *Adv. Colloid Interface Sci.* 247, 521–532.
- (154) Wimley, W. C. (2010) Describing the Mechanism of Antimicrobial Peptide Action with the Interfacial Activity Model 5, 905–917.
- (155) Jackson, M., Mantsch, H. H., and Spencer, J. H. (1992) Conformation of Magainin-2 and Related Peptides in Aqueous Solution and Membrane Environments Probed by Fourier Transform Infrared Spectroscopy. *Biochemistry* 31, 7289–7293.
- (156) Hirsh, D. J., Hammer, J., Maloy, W. L., Blazyk, J., and Schaefer, J. (1996) Secondary structure and location of a magainin analogue in synthetic phospholipid bilayers. *Biochemistry* 35, 12733–12741.
- (157) Williams, R. W., Starman, R., Taylor, K. M. P., Gable, K., Beeler, T., Zasloff, M., and Covell, D. (1990) Raman Spectroscopy of Synthetic Antimicrobial Frog Peptides Magainin 2a and PGLa. *Biochemistry* 29, 4490–4496.
- (158) Nguyen, L. T., Haney, E. F., and Vogel, H. J. (2011) The expanding scope of antimicrobial peptide structures and their modes of action. *Trends Biotechnol.* 29, 464–472.
- (159) Kumashiro, M., Izumi, Y., and Matsuo, K. (2021) Conformation of myelin basic protein bound to phosphatidylinositol membrane characterized by vacuum-ultraviolet circular-dichroism spectroscopy and molecular-dynamics simulations. *Proteins Struct. Funct. Bioinforma.* 89, 1251–1261.

- (160) Rodger, A., Marrington, R., Geeves, M. A., Hicks, M., De Alwis, L., Halsall, D. J., and Dafforn, T. R. (2006) Looking at long molecules in solution: What happens when they are subjected to Couette flow? *Phys. Chem. Chem. Phys.* 8, 3161–3171.
- (161) Bartlett, G. R. (1959) Phosphorus assay in column chromatography. *J. Biol. Chem.* 234, 466–468.
- (162) Chatelier, R. C., and Minton, A. P. (1996) Adsorption of globular proteins on locally planar surfaces: Models for the effect of excluded surface area and aggregation of adsorbed protein on adsorption equilibria. *Biophys. J.* 71, 2367–2374.
- (163) Arouri, A., Dathe, M., and Blume, A. (2009) Peptide induced demixing in PG/PE lipid mixtures: A mechanism for the specificity of antimicrobial peptides towards bacterial membranes? *Biochim. Biophys. Acta - Biomembr.* 1788, 650–659.
- (164) Edwards-Gayle, C. J. C., Barrett, G., Roy, S., Castelletto, V., Seitsonen, J., Ruokolainen, J., and Hamley, I. W. (2020) Selective Antibacterial Activity and Lipid Membrane Interactions of Arginine-Rich Amphiphilic Peptides. *ACS Appl. Bio Mater.* 3, 1165–1175.
- (165) Persson, D., Thorén, P. E. G., Herner, M., Lincoln, P., and Nordén, B. (2003) Application of a novel analysis to measure the binding of the membrane-translocating peptide penetratin to negatively charged liposomes. *Biochemistry* 42, 421–429.
- (166) Manavalan, P., and Johnson, W. C. (1985) Protein secondary structure from circular dichroism spectra. *J. Biosci.* 8, 141–149.
- (167) Zuckermann, M. J., and Heimburg, T. (2001) Insertion and pore formation driven by adsorption of proteins onto lipid bilayer membrane-water interfaces. *Biophys. J.* 81, 2458–2472.
- (168) Gesell, J., Zasloff, M., and Opella, S. J. (1997) Two-dimensional ¹H NMR experiments show that the 23-residue magainin antibiotic peptide is an α -helix in dodecylphosphocholine micelles, sodium dodecylsulfate micelles, and trifluoroethanol/water solution. *J. Biomol. NMR* 9, 127–135.
- (169) Vermeer, L. S., Marquette, A., Schoup, M., Fenard, D., Galy, A., and Bechinger, B. (2016) Simultaneous Analysis of Secondary Structure and Light Scattering from Circular Dichroism Titrations: Application to Vectofusin-1. *Sci. Rep.* 6, 39450.
- (170) Micsonai, A., Wien, F., Kernya, L., Lee, Y. H., Goto, Y., Réfrégiers, M., and Kardos, J. (2015) Accurate secondary structure prediction and fold recognition for circular dichroism spectroscopy. *Proc. Natl. Acad. Sci. U. S. A.* 112, E3095–E3103.

- (171) Lentz, B. R. (1993) Use of fluorescent probes to monitor molecular order and motions within liposome bilayers. *Chem. Phys. Lipids* 64, 99–116.
- (172) Lentz, B. R. (1989) Membrane “fluidity” as detected by diphenylhexatriene probes. *Chem. Phys. Lipids* 50, 171–190.
- (173) Jang, H., Ma, B., Lal, R., and Nussinov, R. (2008) Models of toxic β -sheet channels of protegrin-1 suggest a common subunit organization motif shared with toxic Alzheimer β -amyloid ion channels. *Biophys. J.* 95, 4631–4642.
- (174) Ciudad, S., Puig, E., Botzanowski, T., Meigooni, M., Arango, A. S., Do, J., Mayzel, M., Bayoumi, M., Chaignepain, S., Maglia, G., Cianferani, S., Orekhov, V., Tajkhorshid, E., Bardiaux, B., and Carulla, N. (2020) A β (1-42) tetramer and octamer structures reveal edge conductivity pores as a mechanism for membrane damage. *Nat. Commun.* 11, 3014.
- (175) Rzeźnicka, I. I., Pandey, R., Schleege, M., Bonn, M., and Weidner, T. (2014) Formation of lysozyme oligomers at model cell membranes monitored with sum frequency generation spectroscopy. *Langmuir* 30, 7736–7744.
- (176) Papahadjopoulos, D., Moscarello, M., Eylar, E. H., and Isac, T. (1975) Effects of proteins on the thermotropic phase transitions of phospholipid membranes. *BBA - Biomembr.* 401, 317–335.
- (177) Quinn, P. J. (1981) The fluidity of cell membranes and its regulation. *Prog. Biophys. Mol. Biol.* 38, 1–104.
- (178) Veld, G. I., Driessen, A. J. M., and Konings, W. N. (1993) Bacterial solute transport proteins in their lipid environment. *FEMS Microbiol. Rev.* 12, 293–314.
- (179) Jeffrey R. Hazel, and Williams, E. E. (1990) The role of alterations in membrane lipid composition in enabling physiological adaptation of organisms to their physical environment. *Prog. Lipid Res.* 29, 167–227.
- (180) Avitabile, C., D’Andrea, L. D., and Romanelli, A. (2014) Circular Dichroism studies on the interactions of antimicrobial peptides with bacterial cells. *Sci. Rep.* 4, 4293.